



Population Properties of Compact Objects from the Second LIGO–Virgo Gravitational-Wave Transient Catalog

R. Abbott¹, T. D. Abbott², S. Abraham³, F. Acernese^{4,5}, K. Ackley⁶ , A. Adams⁷, C. Adams⁸, R. X. Adhikari¹, V. B. Adya⁹, C. Affeldt^{10,11}, M. Agathos^{12,13}, K. Agatsuma¹⁴ , N. Aggarwal¹⁵, O. D. Aguiar¹⁶, L. Aiello^{17,18}, A. Ain^{19,20}, P. Ajith²¹, G. Allen²², A. Allocca¹⁹, P. A. Altin²³, A. Amato²³, S. Anand¹ , A. Ananyeva¹, S. B. Anderson¹, W. G. Anderson²⁴, S. V. Angelova²⁵, S. Ansoldi^{26,27}, J. M. Antelis²⁸, S. Antier²⁹, S. Appert¹, K. Arai¹, M. C. Araya¹, J. S. Areeda³⁰, M. Arène²⁹, N. Arnaud^{31,32}, S. M. Aronson³³, K. G. Arun³⁴, Y. Asali³⁵, S. Ascenzi^{17,36}, G. Ashton⁶ , S. M. Aston⁸, P. Astone³⁷, F. Aubin³⁸ , P. Aufmuth^{10,11}, K. AultONeal²⁸, C. Austin², V. Avendano³⁹, S. Babak²⁹, F. Badaracco^{17,18} , M. K. M. Bader⁴⁰, S. Bae⁴¹, A. M. Baer⁷, S. Bagnasco⁴², J. Baird²⁹, M. Ball⁴³, G. Ballardarin³², S. W. Ballmer⁴⁴, A. Bals²⁸, A. Balsamo⁷, G. Baltus⁴⁵, S. Banagiri⁴⁶ , D. Bankar³, R. S. Bankar³, J. C. Barayoga¹, C. Barbieri^{47,48,49}, B. C. Barish¹, D. Barker⁵⁰, P. Barneo⁵¹, S. Barnum⁵², F. Barone^{5,53}, B. Barr⁵⁴, L. Barsotti⁵², M. Barsuglia²⁹, D. Barta⁵⁵, J. Bartlett⁵⁰, I. Bartos³³ , R. Bassiri⁵⁶, A. Basti^{19,20}, M. Bawaj^{57,58}, J. C. Bayley⁵⁴, M. Bazzan^{59,60}, B. R. Becher⁶¹, B. Bécsy⁶² , V. M. Bedakihale⁶³, M. Bejger⁶⁴ , I. Belahcene³¹, D. Beniwal⁶⁵, M. G. Benjamin²⁸, T. F. Bennett⁶⁶, J. D. Bentley¹⁴, F. Bergamin^{10,11}, B. K. Berger⁵⁶, G. Bergmann^{10,11}, S. Bernuzzi¹³ , C. P. L. Berry¹⁵, D. Bersanetti⁶⁷, A. Bertolini⁴⁰, J. Betzwieser⁸, R. Bhandare⁶⁸, A. V. Bhandari³, D. Bhattacharjee⁶⁹ , J. Bidler³⁰, I. A. Bilenko⁷⁰ , G. Billingsley¹, R. Birney⁷¹, O. Birnholtz⁷², S. Biscans^{1,52}, M. Bischl^{73,74}, S. Biscoveanu⁵², A. Bisht^{10,11}, M. Bitossi^{19,32}, M.-A. Bizouard⁷⁵, J. K. Blackburn¹, J. Blackman⁷⁶, C. D. Blair⁷⁷, D. G. Blair⁷⁷, R. M. Blair⁵⁰, O. Blanch⁷⁸, F. Bobba^{79,80}, N. Bode^{10,11}, M. Boer⁷⁵ , Y. Boetzel⁸¹, G. Bogaert⁷⁵, M. Boldrini^{37,82}, F. Bondu⁸³, E. Bonilla⁵⁶, R. Bonnand³⁸, P. Booker^{10,11}, B. A. Boom⁴⁰, R. Bork¹, V. Boschi¹⁹, S. Bose³, V. Bossilkov⁷⁷, V. Boudart⁴⁵, Y. Bouffanaïs^{59,60} , A. Bozzi³², C. Bradaschia¹⁹, P. R. Brady²⁴, A. Bramley⁸, M. Branchesi^{17,18}, J. E. Brau⁴³, M. Breschi¹³, T. Briant⁸⁴, J. H. Briggs⁵⁴, F. Brighenti^{73,74} , A. Brillet⁷⁵, M. Brinkmann^{10,11}, P. Brockill²⁴, A. F. Brooks¹, J. Brooks³², D. D. Brown⁶⁵, S. Brunetti¹, G. Bruno⁸⁵, R. Bruntz⁷, A. Buikema⁵², T. Bulik⁸⁶, H. J. Bulten^{40,87}, A. Buonanno^{88,89}, R. Busicchio¹⁴ , D. Buskulic³⁸, R. L. Byer⁵⁶, M. Cabero^{10,11} , L. Cadonati⁹⁰, M. Caesar⁹¹, G. Cagnoli²³, C. Cahillane¹, J. Calderón Bustillo⁶, J. D. Callaghan⁵⁴, T. A. Callister⁹², E. Calloni^{5,93}, J. B. Camp⁹⁴, M. Canepa^{67,95}, K. C. Cannon⁹⁶, H. Cao⁶⁵, J. Cao⁹⁷, G. Carapella^{79,80}, F. Carbognani³², M. F. Carney¹⁵, M. Carpinelli^{98,99}, G. Carullo^{19,20}, T. L. Carver¹⁰⁰, J. Casanueva Diaz³², C. Casentini^{36,101}, S. Caudill⁴⁰, M. Cavaglia⁶⁹, F. Cavalieri³¹, R. Cavalieri³², G. Cella¹⁹, P. Cerdá-Durán¹⁰², E. Cesarini³⁶, W. Chaibi⁷⁵, K. Chakravarti³, C.-L. Chan¹⁰³, C. Chan⁹⁶, K. Chandra¹⁰⁴, P. Chaniãl³², S. Chao¹⁰⁵, P. Charlton¹⁰⁶, E. A. Chase¹⁵, E. Chassande-Mottin²⁹, D. Chatterjee²⁴, D. Chattopadhyay¹⁰⁷, M. Chaturvedi⁶⁸, K. Chatziioannou⁹², A. Chen¹⁰³, H. Y. Chen¹⁰⁸, X. Chen⁷⁷, Y. Chen⁷⁶, H.-P. Cheng³³, C. K. Cheong¹⁰³, H. Y. Chia³³, F. Chiadini^{80,109}, R. Chierici¹¹⁰, A. Chincarini⁶⁷, A. Chiummo³², G. Cho¹¹¹, H. S. Cho¹¹², M. Cho⁸⁹, S. Choate⁹¹, N. Christensen⁷⁵, Q. Chu⁷⁷, S. Chua⁸⁴, K. W. Chung¹¹³, S. Chung⁷⁷, G. Ciani^{59,60}, P. Cieciela⁶⁴, M. Cieřlar⁶⁴, M. Cifaldi^{36,101}, A. A. Ciobanu⁶⁵, R. Ciolfi^{60,114}, F. Cipriano⁷⁵, A. Cirone^{67,95}, F. Clara⁵⁰, E. N. Clark¹¹⁵, J. A. Clark⁹⁰, L. Clarke¹¹⁶, P. Clearwater¹¹⁷, S. Clesse⁸⁵, F. Cleva⁷⁵, E. Coccia^{17,18}, P.-F. Cohadon⁸⁴, D. E. Cohen³¹, M. Colleoni¹¹⁸, C. G. Collette¹¹⁹, C. Collins¹⁴, M. Colpi^{47,48}, M. Constancio, Jr.¹⁶, L. Conti⁶⁰, S. J. Cooper¹⁴, P. Corban⁸, T. R. Corbitt², I. Cordero-Carrión¹²⁰, S. Corezzi^{57,58}, K. R. Corley³⁵, N. Cornish⁶², D. Corre³¹, A. Corsi¹²¹, S. Cortese³², C. A. Costa¹⁶, R. Cotesta⁸⁸, M. W. Coughlin^{1,46} , S. B. Coughlin^{15,100}, J.-P. Coulon⁷⁵, S. T. Countryman³⁵, P. Couvares¹, P. B. Covas¹¹⁸, D. M. Coward⁷⁷, M. J. Cowart⁸, D. C. Coyne¹, R. Coyne¹²², J. D. E. Creighton²⁴, T. D. Creighton¹²³, M. Croquette⁸⁴, S. G. Crowder¹²⁴, J. R. Cudell⁴⁵, T. J. Cullen², A. Cumming⁵⁴, R. Cummings⁵⁴, L. Cunningham⁵⁴, E. Cuoco^{32,125}, M. Curylo⁸⁶, T. Dal Canton^{31,88}, G. Dálya¹²⁶, A. Dana⁵⁶, L. M. DaneshgaranBajastani⁶⁶, B. D'Angelo^{67,95}, S. L. Danilishin¹²⁷, S. D'Antonio³⁶, K. Danzmann^{10,11}, C. Darsow-Fromm¹²⁸, A. Dasgupta⁶³, L. E. H. Datrier⁵⁴, V. Dattilo³², I. Dave⁶⁸, M. Davier³¹, G. S. Davies¹²⁹, D. Davis¹, E. J. Daw¹³⁰, R. Dean⁹¹, D. DeBra⁵⁶, M. Deenadayalan³, J. Degallaix¹³¹, M. De Laurentis^{5,93}, S. Deléglise⁸⁴, V. Del Favero¹³², F. De Lillo⁸⁵, N. De Lillo⁵⁴, W. Del Pozzo^{19,20}, L. M. DeMarchi¹⁵, F. De Matteis^{36,101}, V. D'Emilio¹⁰⁰, N. Demos⁵², T. Denker^{10,11}, T. Dent¹²⁹, A. Depasse⁸⁵, R. De Pietri^{133,134}, R. De Rosa^{5,93}, C. De Rossi³², R. DeSalvo^{80,135}, O. de Varona^{10,11}, S. Dhurandhar³, M. C. Díaz¹²³, M. Diaz-Ortiz, Jr.³³, N. A. Didio⁴⁴, T. Dietrich⁴⁰, L. Di Fiore⁵, C. DiFronzo¹⁴, C. Di Giorgio^{79,80}, F. Di Giovanni¹⁰², M. Di Giovanni^{136,137}, T. Di Girolamo^{5,93}, A. Di Lieto^{19,20}, B. Ding¹¹⁹, S. Di Pace^{37,82}, I. Di Palma^{37,82}, F. Di Renzo^{19,20}, A. K. Divakarla³³, A. Dmitriev¹⁴, Z. Doctor⁴³, L. D'Onofrio^{5,93}, F. Donovan⁵², K. L. Dooley¹⁰⁰, S. Doravari³, I. Dorrington¹⁰⁰, T. P. Downes²⁴, M. Drago^{17,18}, J. C. Driggers⁵⁰, Z. Du⁹⁷, J.-G. Ducoin³¹, P. Dupej⁵⁴, O. Durante^{79,80}, D. D'Urso^{98,99}, P.-A. Duverne³¹, S. E. Dwyer⁵⁰, P. J. Easter⁶, G. Eddolls⁵⁴, B. Edelman⁴³, T. B. Edo¹³⁰, O. Edy¹³⁸, A. Effler⁸, J. Eichholz⁹, S. S. Eikenberry³³, M. Eisenmann³⁸, R. A. Eisenstein⁵², A. Ejlli¹⁰⁰, L. Errico^{5,93}, R. C. Essick¹⁰⁸, H. Estellés¹¹⁸, D. Estevez³⁸, Z. B. Etienne¹³⁹, T. Etzel¹, M. Evans⁵², T. M. Evans⁸, B. E. Ewing¹⁴⁰, V. Fafone^{17,36,101}, H. Fair⁴⁴, S. Fairhurst¹⁰⁰, X. Fan⁹⁷, A. M. Farah¹⁰⁸, S. Farinon⁶⁷, B. Farr⁴³, W. M. Farr^{92,141}, E. J. Fauchon-Jones¹⁰⁰, M. Favata³⁹, M. Fays^{45,130}, M. Fazio¹⁴², J. Feicht¹, M. M. Fejer⁵⁶, F. Feng²⁹, E. Fenyvesi^{55,143}, D. L. Ferguson⁹⁰, A. Fernandez-Galiana⁵², I. Ferrante^{19,20}, T. A. Ferreira¹⁶, F. Fiducaro^{19,20}, P. Figura⁸⁶, I. Fiori³², D. Fiorucci^{17,18}, M. Fishbach¹⁰⁸ , R. P. Fisher⁷, J. M. Fishner⁵², R. Fittipaldi^{80,144}, M. Fitz-Axen⁴⁶, V. Fiumara^{80,145}, R. Flamini^{38,146}, E. Floden⁴⁶, E. Flynn³⁰, H. Fong⁹⁶, J. A. Font^{102,147}, P. W. F. Forsyth⁹, J.-D. Fournier⁷⁵, S. Frasca^{37,82}, F. Frasconi¹⁹, Z. Frei¹²⁶, A. Freise¹⁴, R. Frey⁴³, V. Frey³¹, P. Fritschel⁵², V. V. Frolov⁸,

G. G. Fronzé⁴², P. Fulda³³, M. Fyffe⁸, H. A. Gabbard⁵⁴, B. U. Gadre⁸⁸, S. M. Gaebel¹⁴, J. R. Gair⁸⁸, J. Gais¹⁰³, S. Galaudage⁶, R. Gamba¹³, D. Ganapathy⁵², A. Ganguly²¹, S. G. Gaonkar³, B. Garaventa^{67,95}, C. García-Quirós¹¹⁸, F. Garufi^{5,93}, B. Gateley⁵⁰, S. Gaudio²⁸, V. Gayathri³³, G. Gemme⁶⁷, A. Gennai¹⁹, D. George²², J. George⁶⁸, L. Gergely¹⁴⁸, S. Ghonge⁹⁰, Abhirup Ghosh⁸⁸, Archisman Ghosh^{40,149,150,151}, S. Ghosh^{24,39}, B. Giacomazzo^{47,48,49}, L. Giacoppo^{37,82}, J. A. Giaime^{2,8}, K. D. Giardino⁸, D. R. Gibson⁷¹, C. Gier²⁵, K. Gill³⁵, P. Giri^{19,20}, J. Glanzer², A. E. Gleckl³⁰, P. Godwin¹⁴⁰, E. Goetz¹⁵², R. Goetz³³, N. Gohlke^{10,11}, B. Goncharov⁶, G. González², A. Gopakumar¹⁵³, S. E. Gossan¹, M. Gosselin^{19,20}, R. Gouaty³⁸, B. Grace⁹, A. Grado^{5,154}, M. Granata¹³¹, V. Granata⁷⁹, A. Grant⁵⁴, S. Gras⁵², P. Grassia¹, C. Gray⁵⁰, R. Gray⁵⁴, G. Greco^{73,74}, A. C. Green³³, R. Green¹⁰⁰, E. M. Gretarsson²⁸, H. L. Griggs⁹⁰, G. Grignani^{57,58}, A. Grimaldi^{136,137}, E. Grimes²⁸, S. J. Grimm^{17,18}, H. Grote¹⁰⁰, S. Grunewald⁸⁸, P. Gruning³¹, J. G. Guerrero³⁰, G. M. Guidi^{73,74}, A. R. Guimaraes², G. Guixé⁵¹, H. K. Gulati⁶³, Y. Guo⁴⁰, Anchal Gupta¹, Anuradha Gupta¹⁴⁰, P. Gupta^{40,155}, E. K. Gustafson¹, R. Gustafson¹⁵⁶, F. Guzman¹¹⁵, L. Haegel²⁹, O. Halim^{17,18}, E. D. Hall⁵², E. Z. Hamilton¹⁰⁰, G. Hammond⁵⁴, M. Haney⁸¹, M. M. Hanke^{10,11}, J. Hanks⁵⁰, C. Hanna¹⁴⁰, O. A. Hannuksela¹⁰³, O. Hannuksela^{40,155}, H. Hansen⁵⁰, T. J. Hansen²⁸, J. Hanson⁸, T. Harder⁷⁵, T. Hardwick², K. Haris^{21,40,155}, J. Harms^{17,18}, G. M. Harry¹⁵⁷, I. W. Harry¹³⁸, D. Hartwig¹²⁸, R. K. Hasskew⁸, C.-J. Haster⁵², K. Haughian⁵⁴, F. J. Hayes⁵⁴, J. Healy¹³², A. Heidmann⁸⁴, M. C. Heintze⁸, J. Heinze^{10,11}, J. Heinzl¹⁵⁸, H. Heitmann⁷⁵, F. Hellman¹⁵⁹, P. Hello³¹, A. F. Helmling-Cornell⁴³, G. Hemming³², M. Hendry⁵⁴, I. S. Heng⁵⁴, E. Hennes⁴⁰, J. Hennig^{10,11}, M. H. Hennig^{10,11}, F. Hernandez Vivanco⁶, M. Heurs^{10,11}, S. Hild¹²⁷, P. Hill²⁵, A. S. Hines¹¹⁵, S. Hochheim^{10,11}, E. Hofgard⁵⁶, D. Hofman¹³¹, J. N. Hohmann¹²⁸, A. M. Holgado²², N. A. Holland⁹, I. J. Hollows¹³⁰, Z. J. Holmes⁶⁵, K. Holt⁸, D. E. Holz¹⁰⁸, P. Hopkins¹⁰⁰, C. Horst²⁴, J. Hough⁵⁴, E. J. Howell⁷⁷, C. G. Hoy¹⁰⁰, D. Hoyland¹⁴, Y. Huang⁵², M. T. Hübner⁶, A. D. Huddart¹¹⁶, E. A. Huerta²², B. Hughey²⁸, V. Hui³⁸, S. Husa¹¹⁸, S. H. Huttner⁵⁴, B. M. Hutzler², R. Huxford¹⁴⁰, T. Huynh-Dinh⁸, B. Idzkowski⁸⁶, A. Iess^{36,101}, S. Imperato¹⁵, H. Inchauspe³³, C. Ingram⁶⁵, G. Intini^{37,82}, M. Isi⁵², B. R. Iyer²¹, V. JaberianHamedan⁷⁷, T. Jacqmin⁸⁴, S. J. Jadhav¹⁶⁰, S. P. Jadhav³, A. L. James¹⁰⁰, K. Jani⁹⁰, K. Janssens¹⁶¹, N. N. Janthalur¹⁶⁰, P. Jaranowski¹⁶², D. Jariwala³³, R. Jaume¹¹⁸, A. C. Jenkins¹¹³, M. Jeunon⁴⁶, J. Jiang³³, G. R. Johns⁷, A. W. Jones¹⁴, D. I. Jones¹⁶³, J. D. Jones⁵⁰, P. Jones¹⁴, R. Jones⁵⁴, R. J. G. Jonker⁴⁰, L. Ju⁷⁷, J. Junker^{10,11}, C. V. Kalaghatgi¹⁰⁰, V. Kalogera¹⁵, B. Kamai¹, S. Kandhasamy³, G. Kang⁴¹, J. B. Kanner¹, S. J. Kapadia²¹, D. P. Kapasi⁹, C. Karathanasis⁷⁸, S. Karki⁶⁹, R. Kashyap¹⁴⁰, M. Kasprzak¹, W. Kastaun^{10,11}, S. Katsanevas³², E. Katsavounidis⁵², W. Katzman⁸, K. Kawabe⁵⁰, F. Kéfélian⁷⁵, D. Keitel¹¹⁸, J. S. Key¹⁶⁴, S. Khadka⁵⁶, F. Y. Khalili⁷⁰, I. Khan^{17,36}, S. Khan¹⁰⁰, E. A. Khazanov¹⁶⁵, N. Khetan^{17,18}, M. Khurshed⁶⁸, N. Kijbunchoo⁹, C. Kim¹⁶⁶, G. J. Kim⁹⁰, J. C. Kim¹⁶⁷, K. Kim¹⁶⁸, W. S. Kim¹⁶⁹, Y.-M. Kim¹⁷⁰, C. Kimball¹⁵, P. J. King⁵⁰, M. Kinley-Hanlon⁵⁴, R. Kirchhoff^{10,11}, J. S. Kissel⁵⁰, L. Kleybolte¹²⁸, S. Klimenko³³, T. D. Knowles¹³⁹, E. Knyazev⁵², P. Koch^{10,11}, S. M. Koehlenbeck^{10,11}, G. Koekoek^{40,171}, S. Koley⁴⁰, M. Kolstein⁷⁸, K. Komori⁵², V. Kondrashov¹, A. Kontos⁶¹, N. Koper^{10,11}, M. Korobko¹²⁸, W. Z. Korth¹, M. Kovalam⁷⁷, D. B. Kozak¹, C. Krämer^{10,11}, V. Kringel^{10,11}, N. V. Krishnendu^{10,11}, A. Królak^{172,173}, G. Kuehn^{10,11}, A. Kumar¹⁶⁰, P. Kumar¹⁷⁴, Rahul Kumar⁵⁰, Rakesh Kumar⁶³, K. Kuns⁵², S. Kwang²⁴, B. D. Lackey⁸⁸, D. Laghi^{19,20}, E. Lalande¹⁷⁵, T. L. Lam¹⁰³, A. Lamberts^{75,176}, M. Landry⁵⁰, B. B. Lane⁵², R. N. Lang⁵², J. Lange¹³², B. Lantz⁵⁶, R. K. Lanza⁵², I. La Rosa³⁸, A. Lartaux-Vollard³¹, P. D. Lasky⁶, M. Laxen⁸, A. Lazzarini¹, C. Lazzaro^{59,60}, P. Leaci^{37,82}, S. Leavey^{10,11}, Y. K. Lecoche⁵⁰, H. M. Lee¹⁶⁸, H. W. Lee¹⁶⁷, J. Lee¹¹¹, K. Lee⁵⁶, J. Lehmann^{10,11}, E. Leon³⁰, N. Leroy³¹, N. Letendre³⁸, Y. Levin⁶, A. Li¹, J. Li⁹⁷, K. J. L. Li¹⁰³, T. G. F. Li¹⁰³, X. Li⁷⁶, F. Linde^{40,177}, S. D. Linker⁶⁶, J. N. Linley⁵⁴, T. B. Littenberg¹⁷⁸, J. Liu^{10,11}, X. Liu²⁴, M. Llorens-Monteaudo¹⁰², R. K. L. Lo¹, A. Lockwood¹⁷⁹, L. T. London⁵², A. Longo^{180,181}, M. Lorenzini^{36,101}, V. Lorette¹⁸², M. Lormand⁸, G. Losurdo¹⁹, J. D. Lough^{10,11}, C. O. Lousto¹³², G. Lovelace³⁰, H. Lück^{10,11}, D. Lumaca^{36,101}, A. P. Lundgren¹³⁸, Y. Ma⁷⁶, R. Macas¹⁰⁰, M. MacInnis⁵², D. M. Macleod¹⁰⁰, I. A. O. MacMillan¹, A. Macquet⁷⁵, I. Magaña Hernandez²⁴, F. Magaña-Sandoval³³, C. Magazzù¹⁹, R. M. Magee¹⁴⁰, E. Majorana³⁷, I. Maksimovic¹⁸², S. Maliakal¹, A. Malik⁶⁸, N. Man⁷⁵, V. Mandic⁴⁶, V. Mangano^{37,82}, G. L. Mansell^{50,52}, M. Manske²⁴, M. Mantovani³², M. Mapelli^{59,60}, F. Marchesoni^{57,183}, F. Marion³⁸, S. Márka³⁵, Z. Márka³⁵, C. Markakis¹², A. S. Markosyan⁵⁶, A. Markowitz¹, E. Maros¹, A. Marquina¹²⁰, S. Marsat²⁹, F. Martelli^{73,74}, I. W. Martin⁵⁴, R. M. Martin³⁹, M. Martinez⁷⁸, V. Martinez²³, D. V. Martynov¹⁴, H. Masalehdan¹²⁸, K. Mason⁵², E. Massera¹³⁰, A. Masserot³⁸, T. J. Massinger⁵², M. Masso-Reid⁵⁴, S. Mastrogiovanni²⁹, A. Matas⁸⁸, M. Mateu-Lucena¹¹⁸, F. Matichard^{1,52}, M. Matushechkina^{10,11}, N. Mavalvala⁵², E. Maynard², J. J. McCann⁷⁷, R. McCarthy⁵⁰, D. E. McClelland⁹, S. McCormick⁸, L. McCuller⁵², S. C. McGuire¹⁸⁴, C. McIsaac¹³⁸, J. McIver¹⁵², D. J. McManus⁹, T. McRae⁹, S. T. McWilliams¹³⁹, D. Meacher²⁴, G. D. Meadors⁶, M. Mehmet^{10,11}, A. K. Mehta⁸⁸, A. Melatos¹¹⁷, D. A. Melchor³⁰, G. Mendell⁵⁰, A. Menendez-Vazquez⁷⁸, R. A. Mercer²⁴, L. Mereni¹³¹, K. Merfeld⁴³, E. L. Merilh⁵⁰, J. D. Merritt⁴³, M. Merzougui⁷⁵, S. Meshkov¹, C. Messenger⁵⁴, C. Messick¹⁸⁵, R. Metzdrorf⁸⁴, P. M. Meyers¹¹⁷, F. Meylahn^{10,11}, A. Mhaske³, A. Miani^{136,137}, H. Miao¹⁴, I. Michaloliakos³³, C. Michel¹³¹, H. Middleton¹¹⁷, L. Milano^{5,93}, A. L. Miller^{33,85}, S. Miller^{92,186}, M. Millhouse¹¹⁷, J. C. Mills¹⁰⁰, E. Milotti^{27,187}, M. C. Milovich-Goff⁶⁶, O. Minazzoli^{75,188}, Y. Minkov³⁶, L. M. Mir⁷⁸, A. Mishkin³³, C. Mishra¹⁸⁹, T. Mistry¹³⁰, S. Mitra³, V. P. Mitrofanov⁷⁰, G. Mitselmakher³³, R. Mittleman⁵², G. Mo⁵², K. Mogushi⁶⁹, S. R. P. Mohapatra⁵², S. R. Mohite²⁴, I. Molina³⁰, M. Molina-Ruiz¹⁵⁹, M. Mondin⁶⁶, M. Montani^{73,74}, C. J. Moore¹⁴, D. Moraru⁵⁰, F. Morawski⁶⁴, G. Moreno⁵⁰, S. Morisaki⁹⁶, B. Mours¹⁹⁰, C. M. Mow-Lowry¹⁴, S. Mozzon¹³⁸, F. Muciaccia^{37,82}, Arunava Mukherjee⁵⁴, D. Mukherjee¹⁴⁰, Soma Mukherjee¹²³, Subroto Mukherjee⁶³, N. Mukund^{10,11}, A. Mullavey⁸, J. Munch⁶⁵, E. A. Muñoz⁴⁴, P. G. Murray⁵⁴, S. L. Nadji^{10,11}, A. Nagar^{42,191,192}, I. Nardecchia^{36,101}, L. Naticchioni³⁷, R. K. Nayak¹⁹³, B. F. Neil⁷⁷, J. Neilson^{80,135}, G. Nelemans¹⁹⁴, T. J. N. Nelson⁸, M. Nery^{10,11}, A. Neunzert¹⁶⁴, K. Y. Ng⁵², S. Ng⁶⁵, C. Nguyen²⁹, P. Nguyen⁴³, T. Nguyen⁵², S. A. Nichols², S. Nissanke^{40,149}, F. Nocera³², M. Noh¹⁵², C. North¹⁰⁰, D. Nothard¹⁹⁵, L. K. Nuttall¹³⁸, J. Oberling⁵⁰,

B. D. O'Brien³³, J. O'Dell¹¹⁶, G. Oganessian^{17,18}, G. H. Oggin¹⁹⁶, J. J. Oh¹⁶⁹, S. H. Oh¹⁶⁹, F. Ohme^{10,11}, H. Ohta⁹⁶, M. A. Okada¹⁶, C. Olivetto³², P. Oppermann^{10,11}, R. J. Oram⁸, B. O'Reilly⁸, R. G. Ormiston⁴⁶, N. Ormsby⁷, L. F. Ortega³³, R. O'Shaughnessy¹³², S. Ossokine⁸⁸, C. Osthelder¹, D. J. Ottaway⁶⁵, H. Overmier⁸, B. J. Owen¹²¹, A. E. Pace¹⁴⁰, G. Pagano^{19,20}, M. A. Page⁷⁷, G. Pagliaroli^{17,18}, A. Pai¹⁰⁴, S. A. Pai⁶⁸, J. R. Palamos⁴³, O. Palashov¹⁶⁵, C. Palomba³⁷, H. Pan¹⁰⁵, P. K. Panda¹⁶⁰, T. H. Pang^{40,155}, C. Pankow¹⁵, F. Pannarale^{37,82}, B. C. Pant⁶⁸, F. Paoletti¹⁹, A. Paoli³², A. Paolone^{37,197}, W. Parker^{8,184}, D. Pascucci⁴⁰, A. Pasqualetti³², R. Passaquietti^{19,20}, D. Passuello¹⁹, M. Patel⁷, B. Patricelli^{19,20}, E. Payne⁶, T. C. Pechsiri³³, M. Pedraza¹, M. Pegoraro⁶⁰, A. Pele⁸, S. Penn¹⁹⁸, A. Perego^{136,137}, C. J. Perez⁵⁰, C. P erigois³⁸, A. Perreca^{136,137}, S. Perri es¹¹⁰, J. Petermann¹²⁸, D. Petterson¹, H. P. Pfeiffer⁸⁸, K. A. Pham⁴⁶, K. S. Phukon^{3,40,177}, O. J. Piccinni^{37,82}, M. Pichot⁷⁵, M. Piendibene^{19,20}, F. Piergiovanni^{73,74}, L. Pierini^{37,82}, V. Pierro^{80,135}, G. Pillant³², F. Pilo¹⁹, L. Pinard¹³¹, I. M. Pinto^{80,135,191}, K. Piotrkowski⁸⁵, M. Pirello⁵⁰, M. Pitkin¹⁹⁹, E. Placidi⁸², W. Plastino^{180,181}, C. Pluchar¹¹⁵, R. Poggiani^{19,20}, E. Polini³⁸, D. Y. T. Pong¹⁰³, S. Ponrathnam³, P. Popolizio³², E. K. Porter²⁹, A. Poverman⁶¹, J. Powell¹⁰⁷, M. Pracchia³⁸, A. K. Prajapati⁶³, K. Prasai⁵⁶, R. Prasanna¹⁶⁰, G. Pratten¹⁴, T. Prestegard²⁴, M. Principe^{80,135,191}, G. A. Prodi^{137,200}, L. Prokhorov¹⁴, P. Proposito^{36,101}, A. Puecher^{40,155}, M. Punturo⁵⁷, F. Puosi^{19,20}, P. Puppo³⁷, M. P urrer⁸⁸, H. Qi¹⁰⁰, V. Quetschke¹²³, P. J. Quinonez²⁸, R. Quitzow-James⁶⁹, F. J. Raab⁵⁰, G. Raaijmakers^{40,149}, H. Radkins⁵⁰, N. Radulesco⁷⁵, P. Raffai¹²⁶, H. Rafferty²⁰¹, S. X. Rail¹⁷⁵, S. Raja⁶⁸, C. Rajan⁶⁸, B. Rajbhandari¹²¹, M. Rakhmanov¹²³, K. E. Ramirez¹²³, T. D. Ramirez³⁰, A. Ramos-Buades¹¹⁸, J. Rana¹⁴⁰, K. Rao¹⁵, P. Rapagnani^{37,82}, U. D. Rapol²⁰², B. Ratto²⁸, V. Raymond¹⁰⁰, M. Razzano^{19,20}, J. Read³⁰, T. Regimbau³⁸, L. Rei⁶⁷, S. Reid²⁵, D. H. Reitze^{1,33}, P. Rettegno^{42,203}, F. Ricci^{37,82}, C. J. Richardson²⁸, J. W. Richardson¹, L. Richardson¹¹⁵, P. M. Ricker²², G. Riemenschneider^{42,203}, K. Riles¹⁵⁶, M. Rizzo¹⁵, N. A. Robertson^{1,54}, F. Robinet³¹, A. Rocchi³⁶, J. A. Rocha³⁰, S. Rodriguez³⁰, R. D. Rodriguez-Soto²⁸, L. Rolland³⁸, J. G. Rollins¹, V. J. Roma⁴³, M. Romanelli⁸³, R. Romano^{4,5}, C. L. Romel⁵⁰, A. Romero⁷⁸, I. M. Romero-Shaw⁶, J. H. Romie⁸, S. Ronchini^{17,18}, C. A. Rose²⁴, D. Rose³⁰, K. Rose¹⁹⁵, M. J. B. Rosell¹⁸⁵, D. Rosińska⁸⁶, S. G. Rosofsky²², M. P. Ross¹⁷⁹, S. Rowan⁵⁴, S. J. Rowlinson¹⁴, Santosh Roy³, Soumen Roy²⁰⁴, P. Ruggi³², K. Ryan⁵⁰, S. Sachdev¹⁴⁰, T. Sadecki⁵⁰, M. Sakellariadou¹¹³, O. S. Salafia^{47,48,49}, L. Salconi³², M. Saleem³⁴, A. Samajdar^{40,155}, E. J. Sanchez¹, J. H. Sanchez³⁰, L. E. Sanchez¹, N. Sanchis-Gual²⁰⁵, J. R. Sanders²⁰⁶, K. A. Santiago³⁹, E. Santos⁷⁵, T. R. Saravanan³, N. Sarin⁶, B. Sassolas¹³¹, B. S. Sathyaprakash^{100,140}, O. Sauter³⁸, R. L. Savage⁵⁰, V. Savant³, D. Sawant¹⁰⁴, S. Sayah¹³¹, D. Schaetzl¹, P. Schale⁴³, M. Scheel⁷⁶, J. Scheuer¹⁵, A. Schindler-Tyka³³, P. Schmidt¹⁴, R. Schnabel¹²⁸, R. M. S. Schofield⁴³, A. Sch onbeck¹²⁸, E. Schreiber^{10,11}, B. W. Schulte^{10,11}, B. F. Schutz^{10,100}, O. Schwarm¹⁹⁶, E. Schwartz¹⁰⁰, J. Scott⁵⁴, S. M. Scott⁹, M. Seglar-Arroyo³⁸, E. Seidel²², D. Sellers⁸, A. S. Sengupta²⁰⁴, N. Sennett⁸⁸, D. Sentenac³², V. Sequino^{5,93}, A. Sergeev¹⁶⁵, Y. Setyawati^{10,11}, T. Shaffer⁵⁰, M. S. Shahriar¹⁵, S. Sharifi², A. Sharma^{17,18}, P. Sharma⁶⁸, P. Shawhan⁸⁹, H. Shen²², M. Shikauchi⁹⁶, R. Shink¹⁷⁵, D. H. Shoemaker⁵², D. M. Shoemaker⁹⁰, K. Shukla¹⁵⁹, S. ShyamSundar⁶⁸, M. Sieniawska⁶⁴, D. Sigg⁵⁰, L. P. Singer⁹⁴, D. Singh¹⁴⁰, N. Singh⁸⁶, A. Singha¹²⁷, A. Singhal^{17,37}, A. M. Sintes¹¹⁸, V. Sipala^{98,99}, V. Skliris¹⁰⁰, B. J. J. Slagmolen⁹, T. J. Slaven-Blair⁷⁷, J. Smetana¹⁴, J. R. Smith³⁰, R. J. E. Smith⁶, S. N. Somala²⁰⁷, E. J. Son¹⁶⁹, S. Soni², B. Sorazu⁵⁴, V. Sordini¹¹⁰, F. Sorrentino⁶⁷, N. Sorrentino^{19,20}, R. Soulard⁷⁵, T. Souradeep^{3,202}, E. Sowell¹²¹, A. P. Spencer⁵⁴, M. Spera^{15,59,60}, A. K. Srivastava⁶³, V. Srivastava⁴⁴, K. Staats¹⁵, C. Stachie⁷⁵, D. A. Steer²⁹, M. Steinke^{10,11}, J. Steinlechner^{54,127}, S. Steinlechner¹²⁷, D. Steinmeyer^{10,11}, S. P. Stevenson¹⁰⁷, G. Stolle-McAllister¹⁹⁵, D. J. Stops¹⁴, M. Stover¹⁹⁵, K. A. Strain⁵⁴, G. Stratta^{74,208}, A. Strunk⁵⁰, R. Sturani²⁰⁹, A. L. Stuver⁹¹, J. S udbeck¹²⁸, S. Sudhagar³, V. Sudhir⁵², H. G. Suh²⁴, T. Z. Summerscales²¹⁰, H. Sun⁷⁷, L. Sun¹, S. Sunil⁶³, A. Sur⁶⁴, J. Suresh⁹⁶, P. J. Sutton¹⁰⁰, B. L. Swinkels⁴⁰, M. J. Szczepańczyk³³, M. Tacca⁴⁰, S. C. Tait⁵⁴, C. Talbot⁶, A. J. Tanasijczuk⁸⁵, D. B. Tanner³³, D. Tao¹, A. Tapia³⁰, E. N. Tapia San Martin⁴⁰, J. D. Tasson¹⁵⁸, R. Taylor¹, R. Tenorio¹¹⁸, L. Terkowski¹²⁸, M. P. Thirugnanasambandam³, L. Thomas¹⁴, M. Thomas⁸, P. Thomas⁵⁰, J. E. Thompson¹⁰⁰, S. R. Thondapu⁶⁸, K. A. Thorne⁸, E. Thrane⁶, Shubhanshu Tiwari⁸¹, Srishti Tiwari¹⁵³, V. Tiwari¹⁰⁰, K. Toland⁵⁴, A. E. Tolley¹³⁸, M. Tonelli^{19,20}, Z. Tornasi⁵⁴, A. Torres-Forn e⁸⁸, C. I. Torrie¹, I. Tosta e Melo^{98,99}, D. T oyr a⁹, A. T. Tran¹²⁴, A. Trapananti^{57,183}, F. Travasso^{57,183}, G. Traylor⁸, M. C. Tringali⁸⁶, A. Tripathee¹⁵⁶, A. Trovato²⁹, R. J. Trudeau¹, D. S. Tsai¹⁰⁵, K. W. Tsang^{40,155,211}, M. Tse⁵², R. Tso⁷⁶, L. Tsukada⁹⁶, D. Tsuna⁹⁶, T. Tsutsui⁹⁶, M. Turconi⁷⁵, A. S. Ubhi¹⁴, R. P. Udall⁹⁰, K. Ueno⁹⁶, D. Ugolini²⁰¹, C. S. Unnikrishnan¹⁵³, A. L. Urban², S. A. Usman¹⁰⁸, A. C. Utina¹²⁷, H. Vahlbruch^{10,11}, G. Vajente¹, A. Vajpeyi⁶, G. Valdes², M. Valentini^{136,137}, V. Valsan²⁴, N. van Bakel⁴⁰, M. van Beuzekom⁴⁰, J. F. J. van den Brand^{40,87,171}, C. Van Den Broeck^{40,155}, D. C. Vander-Hyde⁴⁴, L. van der Schaaf⁴⁰, J. V. van Heijningen⁷⁷, M. Vardaro^{40,177}, A. F. Vargas¹¹⁷, V. Varma⁷⁶, S. Vass¹, M. Vas uth⁵⁵, A. Vecchio¹⁴, G. Vedovato⁶⁰, J. Veitch⁵⁴, P. J. Veitch⁶⁵, K. Venkateswara¹⁷⁹, J. Venneberg^{10,11}, G. Venugopalan¹, D. Verkindt³⁸, Y. Verma⁶⁸, D. Veske³⁵, F. Vetrano⁷³, A. Vicer e^{73,74}, A. D. Viets²¹², V. Villa-Ortega¹²⁹, J.-Y. Vinet⁷⁵, S. Vitale⁵², T. Vo⁴⁴, H. Vocca^{57,58}, C. Vorvick⁵⁰, S. P. Vyatchanin⁷⁰, A. R. Wade⁹, L. E. Wade¹⁹⁵, M. Wade¹⁹⁵, R. C. Walet⁴⁰, M. Walker⁷, G. S. Wallace²⁵, L. Wallace¹, S. Walsh²⁴, J. Z. Wang¹⁵⁶, S. Wang²², W. H. Wang¹²³, Y. F. Wang¹⁰³, R. L. Ward⁹, J. Warner⁵⁰, M. Was³⁸, N. Y. Washington¹, J. Watchi¹¹⁹, B. Weaver⁵⁰, L. Wei^{10,11}, M. Weinert^{10,11}, A. J. Weinstein¹, R. Weiss⁵², F. Wellmann^{10,11}, L. Wen⁷⁷, P. Weels^{10,11}, J. W. Westhouse²⁸, K. Wette⁹, J. T. Whelan¹³², D. D. White³⁰, L. V. White⁴⁴, B. F. Whiting³³, C. Whittle⁵², D. M. Wilken^{10,11}, D. Williams⁵⁴, M. J. Williams⁵⁴, A. R. Williamson¹³⁸, J. L. Willis¹, B. Willke^{10,11}, D. J. Wilson¹¹⁵, M. H. Wimmer^{10,11}, W. Winkler^{10,11}, C. C. Wipf¹, G. Woan⁵⁴, J. Woehler^{10,11}, J. K. Wofford¹³², I. C. F. Wong¹⁰³, J. Wrangel^{10,11}, J. L. Wright⁵⁴, D. S. Wu^{10,11}, D. M. Wysocki¹³², L. Xiao¹, H. Yamamoto¹, L. Yang¹⁴², Y. Yang³³, Z. Yang⁴⁶, M. J. Yap⁹, D. W. Yeeles¹⁰⁰, A. Yoon⁷, Hang Yu⁷⁶, Haocun Yu⁵², S. H. R. Yuen¹⁰³, A. Zadrożny¹⁷³, M. Zanolin²⁸, T. Zelenova³², J.-P. Zendi⁶⁰, M. Zevin¹⁵, J. Zhang⁷⁷, L. Zhang¹, R. Zhang³³, T. Zhang¹⁴, C. Zhao⁷⁷, G. Zhao¹¹⁹, M. Zhou¹⁵, Z. Zhou¹⁵, X. J. Zhu⁶

A. B. Zimmerman¹⁸⁵, M. E. Zucker^{1,52}, and J. Zweizig¹

The LIGO Scientific Collaboration and the Virgo Collaboration

- ¹ LIGO, California Institute of Technology, Pasadena, CA 91125, USA
² Louisiana State University, Baton Rouge, LA 70803, USA
³ Inter-University Centre for Astronomy and Astrophysics, Pune 411007, India
⁴ Dipartimento di Farmacia, Università di Salerno, I-84084 Fisciano, Salerno, Italy
⁵ INFN, Sezione di Napoli, Complesso Universitario di Monte S. Angelo, I-80126 Napoli, Italy
⁶ OzGrav, School of Physics & Astronomy, Monash University, Clayton 3800, VIC, Australia
⁷ Christopher Newport University, Newport News, VA 23606, USA
⁸ LIGO Livingston Observatory, Livingston, LA 70754, USA
⁹ OzGrav, Australian National University, Canberra, ACT 0200, Australia
¹⁰ Max Planck Institute for Gravitational Physics (Albert Einstein Institute), D-30167 Hannover, Germany
¹¹ Leibniz Universität Hannover, D-30167 Hannover, Germany
¹² University of Cambridge, Cambridge CB2 1TN, UK
¹³ Theoretisch-Physikalisches Institut, Friedrich-Schiller-Universität Jena, D-07743 Jena, Germany
¹⁴ University of Birmingham, Birmingham B15 2TT, UK
¹⁵ Center for Interdisciplinary Exploration & Research in Astrophysics (CIERA), Northwestern University, Evanston, IL 60208, USA
¹⁶ Instituto Nacional de Pesquisas Espaciais, 12227-010 São José dos Campos, São Paulo, Brazil
¹⁷ Gran Sasso Science Institute (GSSI), I-67100 L'Aquila, Italy
¹⁸ INFN, Laboratori Nazionali del Gran Sasso, I-67100 Assergi, Italy
¹⁹ INFN, Sezione di Pisa, I-56127 Pisa, Italy
²⁰ Università di Pisa, I-56127 Pisa, Italy
²¹ International Centre for Theoretical Sciences, Tata Institute of Fundamental Research, Bengaluru 560089, India
²² NCSA, University of Illinois at Urbana-Champaign, Urbana, IL 61801, USA
²³ Université de Lyon, Université Claude Bernard Lyon 1, CNRS, Institut Lumière Matière, F-69622 Villeurbanne, France
²⁴ University of Wisconsin–Milwaukee, Milwaukee, WI 53201, USA
²⁵ SUPA, University of Strathclyde, Glasgow G1 1XQ, UK
²⁶ Dipartimento di Matematica e Informatica, Università di Udine, I-33100 Udine, Italy
²⁷ INFN, Sezione di Trieste, I-34127 Trieste, Italy
²⁸ Embry-Riddle Aeronautical University, Prescott, AZ 86301, USA
²⁹ Université de Paris, CNRS, Astroparticule et Cosmologie, F-75013 Paris, France
³⁰ California State University Fullerton, Fullerton, CA 92831, USA
³¹ Université Paris-Saclay, CNRS/IN2P3, IJCLab, F-91405 Orsay, France
³² European Gravitational Observatory (EGO), I-56021 Cascina, Pisa, Italy
³³ University of Florida, Gainesville, FL 32611, USA
³⁴ Chennai Mathematical Institute, Chennai 603103, India
³⁵ Columbia University, New York, NY 10027, USA
³⁶ INFN, Sezione di Roma Tor Vergata, I-00133 Roma, Italy
³⁷ INFN, Sezione di Roma, I-00185 Roma, Italy
³⁸ Laboratoire d'Annecy de Physique des Particules (LAPP), Univ. Grenoble Alpes, Université Savoie Mont Blanc, CNRS/IN2P3, F-74941 Annecy, France
³⁹ Montclair State University, Montclair, NJ 07043, USA
⁴⁰ Nikhef, Science Park 105, 1098 XG Amsterdam, The Netherlands
⁴¹ Korea Institute of Science and Technology Information, Daejeon 34141, Republic of Korea
⁴² INFN Sezione di Torino, I-10125 Torino, Italy
⁴³ University of Oregon, Eugene, OR 97403, USA
⁴⁴ Syracuse University, Syracuse, NY 13244, USA
⁴⁵ Université de Liège, B-4000 Liège, Belgium
⁴⁶ University of Minnesota, Minneapolis, MN 55455, USA
⁴⁷ Università degli Studi di Milano-Bicocca, I-20126 Milano, Italy
⁴⁸ INFN, Sezione di Milano-Bicocca, I-20126 Milano, Italy
⁴⁹ INAF, Osservatorio Astronomico di Brera sede di Merate, I-23807 Merate, Lecco, Italy
⁵⁰ LIGO Hanford Observatory, Richland, WA 99352, USA
⁵¹ Institut de Ciències del Cosmos, Universitat de Barcelona, C/ Martí i Franquès 1, Barcelona, E-08028, Spain
⁵² LIGO, Massachusetts Institute of Technology, Cambridge, MA 02139, USA
⁵³ Dipartimento di Medicina, Chirurgia e Odontoiatria "Scuola Medica Salernitana," Università di Salerno, I-84081 Baronissi, Salerno, Italy
⁵⁴ SUPA, University of Glasgow, Glasgow G12 8QQ, UK
⁵⁵ Wigner RCP, RMKI, H-1121 Budapest, Konkoly Thege Miklós út 29-33, Hungary
⁵⁶ Stanford University, Stanford, CA 94305, USA
⁵⁷ INFN, Sezione di Perugia, I-06123 Perugia, Italy
⁵⁸ Università di Perugia, I-06123 Perugia, Italy
⁵⁹ Università di Padova, Dipartimento di Fisica e Astronomia, I-35131 Padova, Italy
⁶⁰ INFN, Sezione di Padova, I-35131 Padova, Italy
⁶¹ Bard College, 30 Campus Road, Annandale-On-Hudson, NY 12504, USA
⁶² Montana State University, Bozeman, MT 59717, USA
⁶³ Institute for Plasma Research, Bhat, Gandhinagar 382428, India
⁶⁴ Nicolaus Copernicus Astronomical Center, Polish Academy of Sciences, 00-716, Warsaw, Poland
⁶⁵ OzGrav, University of Adelaide, Adelaide, SA 5005, Australia
⁶⁶ California State University, Los Angeles, 5151 State University Drive, Los Angeles, CA 90032, USA
⁶⁷ INFN, Sezione di Genova, I-16146 Genova, Italy
⁶⁸ RRCAT, Indore, Madhya Pradesh 452013, India
⁶⁹ Missouri University of Science and Technology, Rolla, MO 65409, USA
⁷⁰ Faculty of Physics, Lomonosov Moscow State University, Moscow 119991, Russia
⁷¹ SUPA, University of the West of Scotland, Paisley PA1 2BE, UK
⁷² Bar-Ilan University, Ramat Gan, 5290002, Israel
⁷³ Università degli Studi di Urbino "Carlo Bo," I-61029 Urbino, Italy

- ⁷⁴ INFN, Sezione di Firenze, I-50019 Sesto Fiorentino, Firenze, Italy
- ⁷⁵ Artemis, Université Côte d’Azur, Observatoire Côte d’Azur, CNRS, F-06304 Nice, France
- ⁷⁶ Caltech CaRT, Pasadena, CA 91125, USA
- ⁷⁷ OzGrav, University of Western Australia, Crawley, WA 6009, Australia
- ⁷⁸ Institut de Física d’Altes Energies (IFAE), Barcelona Institute of Science and Technology, and ICREA, E-08193 Barcelona, Spain
- ⁷⁹ Dipartimento di Fisica “E.R. Caianiello,” Università di Salerno, I-84084 Fisciano, Salerno, Italy
- ⁸⁰ INFN, Sezione di Napoli, Gruppo Collegato di Salerno, Complesso Universitario di Monte S. Angelo, I-80126 Napoli, Italy
- ⁸¹ Physik-Institut, University of Zurich, Winterthurerstrasse 190, 8057 Zurich, Switzerland
- ⁸² Università di Roma “La Sapienza,” I-00185 Roma, Italy
- ⁸³ Univ Rennes, CNRS, Institut FOTON—UMR6082, F-3500 Rennes, France
- ⁸⁴ Laboratoire Kastler Brossel, Sorbonne Université, CNRS, ENS-Université PSL, Collège de France, F-75005 Paris, France
- ⁸⁵ Université catholique de Louvain, B-1348 Louvain-la-Neuve, Belgium
- ⁸⁶ Astronomical Observatory, Warsaw University, 00-478 Warsaw, Poland
- ⁸⁷ VU University Amsterdam, 1081 HV Amsterdam, The Netherlands
- ⁸⁸ Max Planck Institute for Gravitational Physics (Albert Einstein Institute), D-14476 Potsdam-Golm, Germany
- ⁸⁹ University of Maryland, College Park, MD 20742, USA
- ⁹⁰ School of Physics, Georgia Institute of Technology, Atlanta, GA 30332, USA
- ⁹¹ Villanova University, 800 Lancaster Avenue, Villanova, PA 19085, USA
- ⁹² Center for Computational Astrophysics, Flatiron Institute, New York, NY 10010, USA
- ⁹³ Università di Napoli “Federico II,” Complesso Universitario di Monte S. Angelo, I-80126 Napoli, Italy
- ⁹⁴ NASA Goddard Space Flight Center, Greenbelt, MD 20771, USA
- ⁹⁵ Dipartimento di Fisica, Università degli Studi di Genova, I-16146 Genova, Italy
- ⁹⁶ RESCEU, University of Tokyo, Tokyo, 113-0033, Japan
- ⁹⁷ Tsinghua University, Beijing 100084, People’s Republic of China
- ⁹⁸ Università degli Studi di Sassari, I-07100 Sassari, Italy
- ⁹⁹ INFN, Laboratori Nazionali del Sud, I-95125 Catania, Italy
- ¹⁰⁰ Gravity Exploration Institute, Cardiff University, Cardiff CF24 3AA, UK
- ¹⁰¹ Università di Roma Tor Vergata, I-00133 Roma, Italy
- ¹⁰² Departamento de Astronomía y Astrofísica, Universitat de València, E-46100 Burjassot, València, Spain
- ¹⁰³ The Chinese University of Hong Kong, Shatin, NT, Hong Kong
- ¹⁰⁴ Indian Institute of Technology Bombay, Powai, Mumbai 400 076, India
- ¹⁰⁵ National Tsing Hua University, Hsinchu City, 30013 Taiwan, Republic of China
- ¹⁰⁶ Charles Sturt University, Wagga Wagga, NSW 2678, Australia
- ¹⁰⁷ OzGrav, Swinburne University of Technology, Hawthorn, VIC 3122, Australia
- ¹⁰⁸ University of Chicago, Chicago, IL 60637, USA
- ¹⁰⁹ Dipartimento di Ingegneria Industriale (DIIN), Università di Salerno, I-84084 Fisciano, Salerno, Italy
- ¹¹⁰ Institut de Physique des 2 Infinis de Lyon, CNRS/IN2P3, Université de Lyon, Université Claude Bernard Lyon 1, F-69622 Villeurbanne, France
- ¹¹¹ Seoul National University, Seoul 08826, Republic of Korea
- ¹¹² Pusan National University, Busan 46241, Republic of Korea
- ¹¹³ King’s College London, University of London, London WC2R 2LS, UK
- ¹¹⁴ INAF, Osservatorio Astronomico di Padova, I-35122 Padova, Italy
- ¹¹⁵ University of Arizona, Tucson, AZ 85721, USA
- ¹¹⁶ Rutherford Appleton Laboratory, Didcot OX11 0DE, UK
- ¹¹⁷ OzGrav, University of Melbourne, Parkville, VIC 3010, Australia
- ¹¹⁸ Universitat de les Illes Balears, IAC3—IEEC, E-07122 Palma de Mallorca, Spain
- ¹¹⁹ Université Libre de Bruxelles, Brussels B-1050, Belgium
- ¹²⁰ Departamento de Matemáticas, Universitat de València, E-46100 Burjassot, València, Spain
- ¹²¹ Texas Tech University, Lubbock, TX 79409, USA
- ¹²² University of Rhode Island, Kingston, RI 02881, USA
- ¹²³ The University of Texas Rio Grande Valley, Brownsville, TX 78520, USA
- ¹²⁴ Bellevue College, Bellevue, WA 98007, USA
- ¹²⁵ Scuola Normale Superiore, Piazza dei Cavalieri, 7, I-56126 Pisa, Italy
- ¹²⁶ MTA-ELTE Astrophysics Research Group, Institute of Physics, Eötvös University, Budapest 1117, Hungary
- ¹²⁷ Maastricht University, 6200 MD, Maastricht, The Netherlands
- ¹²⁸ Universität Hamburg, D-22761 Hamburg, Germany
- ¹²⁹ IGFAE, Campus Sur, Universidad de Santiago de Compostela, E-15782, Spain
- ¹³⁰ The University of Sheffield, Sheffield S10 2TN, UK
- ¹³¹ Laboratoire des Matériaux Avancés (LMA), Institut de Physique des 2 Infinis de Lyon, CNRS/IN2P3, Université de Lyon, F-69622 Villeurbanne, France
- ¹³² Rochester Institute of Technology, Rochester, NY 14623, USA
- ¹³³ Dipartimento di Scienze Matematiche, Fisiche e Informatiche, Università di Parma, I-43124 Parma, Italy
- ¹³⁴ INFN, Sezione di Milano Bicocca, Gruppo Collegato di Parma, I-43124 Parma, Italy
- ¹³⁵ Dipartimento di Ingegneria, Università del Sannio, I-82100 Benevento, Italy
- ¹³⁶ Università di Trento, Dipartimento di Fisica, I-38123 Povo, Trento, Italy
- ¹³⁷ INFN, Trento Institute for Fundamental Physics and Applications, I-38123 Povo, Trento, Italy
- ¹³⁸ University of Portsmouth, Portsmouth, PO1 3FX, UK
- ¹³⁹ West Virginia University, Morgantown, WV 26506, USA
- ¹⁴⁰ The Pennsylvania State University, University Park, PA 16802, USA
- ¹⁴¹ Stony Brook University, Stony Brook, NY 11794, USA
- ¹⁴² Colorado State University, Fort Collins, CO 80523, USA
- ¹⁴³ Institute for Nuclear Research, Hungarian Academy of Sciences, Bem tér 18/c, H-4026 Debrecen, Hungary
- ¹⁴⁴ CNR-SPIN, c/o Università di Salerno, I-84084 Fisciano, Salerno, Italy
- ¹⁴⁵ Scuola di Ingegneria, Università della Basilicata, I-85100 Potenza, Italy
- ¹⁴⁶ National Astronomical Observatory of Japan, 2-21-1 Osawa, Mitaka, Tokyo 181-8588, Japan
- ¹⁴⁷ Observatori Astronòmic, Universitat de València, E-46980 Paterna, València, Spain
- ¹⁴⁸ University of Szeged, Dóm tér 9, Szeged 6720, Hungary

- ¹⁴⁹ GRAPPA, Anton Pannekoek Institute for Astronomy and Institute for High-Energy Physics, University of Amsterdam, Science Park 904, 1098 XH Amsterdam, The Netherlands
- ¹⁵⁰ Delta Institute for Theoretical Physics, Science Park 904, 1090 GL Amsterdam, The Netherlands
- ¹⁵¹ Lorentz Institute, Leiden University, Niels Bohrweg 2, 2333 CA Leiden, The Netherlands
- ¹⁵² University of British Columbia, Vancouver, BC V6T 1Z4, Canada
- ¹⁵³ Tata Institute of Fundamental Research, Mumbai 400005, India
- ¹⁵⁴ INAF, Osservatorio Astronomico di Capodimonte, I-80131 Napoli, Italy
- ¹⁵⁵ Department of Physics, Utrecht University, Princetonplein 1, 3584 CC Utrecht, The Netherlands
- ¹⁵⁶ University of Michigan, Ann Arbor, MI 48109, USA
- ¹⁵⁷ American University, Washington, DC 20016, USA
- ¹⁵⁸ Carleton College, Northfield, MN 55057, USA
- ¹⁵⁹ University of California, Berkeley, CA 94720, USA
- ¹⁶⁰ Directorate of Construction, Services & Estate Management, Mumbai 400094, India
- ¹⁶¹ Universiteit Antwerpen, Prinsstraat 13, B-2000 Antwerpen, Belgium
- ¹⁶² University of Białystok, 15-424 Białystok, Poland
- ¹⁶³ University of Southampton, Southampton SO17 1BJ, UK
- ¹⁶⁴ University of Washington Bothell, Bothell, WA 98011, USA
- ¹⁶⁵ Institute of Applied Physics, Nizhny Novgorod, 603950, Russia
- ¹⁶⁶ Ewha Womans University, Seoul 03760, Republic of Korea
- ¹⁶⁷ Inje University Gimhae, South Gyeongsang 50834, Republic of Korea
- ¹⁶⁸ Korea Astronomy and Space Science Institute, Daejeon 34055, Republic of Korea
- ¹⁶⁹ National Institute for Mathematical Sciences, Daejeon 34047, Republic of Korea
- ¹⁷⁰ Ulsan National Institute of Science and Technology, Ulsan 44919, Republic of Korea
- ¹⁷¹ Maastricht University, P.O. Box 616, 6200 MD Maastricht, The Netherlands
- ¹⁷² Institute of Mathematics, Polish Academy of Sciences, 00656 Warsaw, Poland
- ¹⁷³ National Center for Nuclear Research, 05-400 Świerk-Otwock, Poland
- ¹⁷⁴ Cornell University, Ithaca, NY 14850, USA
- ¹⁷⁵ Université de Montréal/Polytechnique, Montreal, Quebec H3T 1J4, Canada
- ¹⁷⁶ Laboratoire Lagrange, Université Côte d’Azur, Observatoire Côte d’Azur, CNRS, F-06304 Nice, France
- ¹⁷⁷ Institute for High-Energy Physics, University of Amsterdam, Science Park 904, 1098 XH Amsterdam, The Netherlands
- ¹⁷⁸ NASA Marshall Space Flight Center, Huntsville, AL 35811, USA
- ¹⁷⁹ University of Washington, Seattle, WA 98195, USA
- ¹⁸⁰ Dipartimento di Matematica e Fisica, Università degli Studi Roma Tre, I-00146 Roma, Italy
- ¹⁸¹ INFN, Sezione di Roma Tre, I-00146 Roma, Italy
- ¹⁸² ESPCI, CNRS, F-75005 Paris, France
- ¹⁸³ Università di Camerino, Dipartimento di Fisica, I-62032 Camerino, Italy
- ¹⁸⁴ Southern University and A&M College, Baton Rouge, LA 70813, USA
- ¹⁸⁵ Department of Physics, University of Texas, Austin, TX 78712, USA
- ¹⁸⁶ Department of Physics, Smith College, Northampton, MA 01063, USA
- ¹⁸⁷ Dipartimento di Fisica, Università di Trieste, I-34127 Trieste, Italy
- ¹⁸⁸ Centre Scientifique de Monaco, 8 quai Antoine 1er, MC-98000, Monaco
- ¹⁸⁹ Indian Institute of Technology Madras, Chennai 600036, India
- ¹⁹⁰ Institut Pluridisciplinaire Hubert CURIE, 23 rue du loess—BP28 67037 Strasbourg cedex 2, France
- ¹⁹¹ Museo Storico della Fisica e Centro Studi e Ricerche “Enrico Fermi,” I-00184 Roma, Italy
- ¹⁹² Institut des Hautes Etudes Scientifiques, F-91440 Bures-sur-Yvette, France
- ¹⁹³ Indian Institute of Science Education and Research, Kolkata, Mohanpur, West Bengal 741252, India
- ¹⁹⁴ Department of Astrophysics/IMAPP, Radboud University Nijmegen, P.O. Box 9010, 6500 GL Nijmegen, The Netherlands
- ¹⁹⁵ Kenyon College, Gambier, OH 43022, USA
- ¹⁹⁶ Whitman College, 345 Boyer Avenue, Walla Walla, WA 99362, USA
- ¹⁹⁷ Consiglio Nazionale delle Ricerche - Istituto dei Sistemi Complessi, Piazzale Aldo Moro 5, I-00185 Roma, Italy
- ¹⁹⁸ Hobart and William Smith Colleges, Geneva, NY 14456, USA
- ¹⁹⁹ Lancaster University, Lancaster LA1 4YW, UK
- ²⁰⁰ Università di Trento, Dipartimento di Matematica, I-38123 Povo, Trento, Italy
- ²⁰¹ Trinity University, San Antonio, TX 78212, USA
- ²⁰² Indian Institute of Science Education and Research, Pune, Maharashtra 411008, India
- ²⁰³ Dipartimento di Fisica, Università degli Studi di Torino, I-10125 Torino, Italy
- ²⁰⁴ Indian Institute of Technology, Palaj, Gandhinagar, Gujarat 382355, India
- ²⁰⁵ Centro de Astrofísica e Gravitação (CENTRA), Departamento de Física, Instituto Superior Técnico, Universidade de Lisboa, 1049-001 Lisboa, Portugal
- ²⁰⁶ Marquette University, 11420 West Clybourn Street, Milwaukee, WI 53233, USA
- ²⁰⁷ Indian Institute of Technology Hyderabad, Sangareddy, Khandi, Telangana 502285, India
- ²⁰⁸ INAF, Osservatorio di Astrofisica e Scienza dello Spazio, I-40129 Bologna, Italy
- ²⁰⁹ International Institute of Physics, Universidade Federal do Rio Grande do Norte, Natal RN 59078-970, Brazil
- ²¹⁰ Andrews University, Berrien Springs, MI 49104, USA
- ²¹¹ Van Swinderen Institute for Particle Physics and Gravity, University of Groningen, Nijenborgh 4, 9747 AG Groningen, The Netherlands
- ²¹² Concordia University Wisconsin, Mequon, WI 53097, USA

Received 2020 October 25; revised 2021 February 22; accepted 2021 February 24; published 2021 May 19

Abstract

We report on the population of 47 compact binary mergers detected with a false-alarm rate of $<1 \text{ yr}^{-1}$ in the second LIGO–Virgo Gravitational-Wave Transient Catalog. We observe several characteristics of the merging binary black hole (BBH) population not discernible until now. First, the primary mass spectrum contains structure beyond a power law with a sharp high-mass cutoff; it is more consistent with a broken power law with a break at $39.7_{-9.1}^{+20.3} M_{\odot}$ or a power law with a Gaussian feature peaking at $33.1_{-5.6}^{+4.0} M_{\odot}$ (90% credible interval). While the primary mass distribution must extend to $\sim 65 M_{\odot}$ or beyond, only $2.9_{-1.7}^{+3.5}\%$ of systems have primary

masses greater than $45 M_{\odot}$. Second, we find that a fraction of BBH systems have component spins misaligned with the orbital angular momentum, giving rise to precession of the orbital plane. Moreover, 12%–44% of BBH systems have spins tilted by more than 90° , giving rise to a negative effective inspiral spin parameter, χ_{eff} . Under the assumption that such systems can only be formed by dynamical interactions, we infer that between 25% and 93% of BBHs with nonvanishing $|\chi_{\text{eff}}| > 0.01$ are dynamically assembled. Third, we estimate merger rates, finding $\mathcal{R}_{\text{BBH}} = 23.9_{-8.6}^{+14.3} \text{ Gpc}^{-3} \text{ yr}^{-1}$ for BBHs and $\mathcal{R}_{\text{BNS}} = 320_{-240}^{+490} \text{ Gpc}^{-3} \text{ yr}^{-1}$ for binary neutron stars. We find that the BBH rate likely increases with redshift (85% credibility) but not faster than the star formation rate (86% credibility). Additionally, we examine recent exceptional events in the context of our population models, finding that the asymmetric masses of GW190412 and the high component masses of GW190521 are consistent with our models, but the low secondary mass of GW190814 makes it an outlier.

Unified Astronomy Thesaurus concepts: [Gravitational waves \(678\)](#); [Astrophysical black holes \(98\)](#); [Stellar mass black holes \(1611\)](#); [Massive stars \(732\)](#); [Compact objects \(288\)](#); [Bayesian statistics \(1900\)](#)

1. Introduction

We analyze the population properties of black holes (BHs) and neutron stars (NSs) in compact binary systems using data from the LIGO–Virgo Gravitational-Wave Transient Catalog 2 (GWTC-2; Abbott et al. 2020c). The GWTC-2 catalog combines observations from the first two observing runs (O1 and O2; Abbott et al. 2019b) and the first half of the third observing run (O3a; Abbott et al. 2020c) of the Advanced LIGO (Aasi et al. 2015) and Advanced Virgo (Acernese et al. 2015) gravitational-wave observatories. With the 39 additional candidates from O3a, we have more than quadrupled the number of events from O1 and O2, published in the first LIGO–Virgo Transient Catalog (GWTC-1; Abbott et al. 2019b). Counting only events with a false-alarm rate (FAR) of $< 1 \text{ yr}^{-1}$ (as opposed to the less conservative FAR threshold of $< 2 \text{ yr}^{-1}$ in GWTC-2), the new combined catalog includes two binary NS (BNS) events, 44 confident binary BH (BBH) events, and one NS–BH (NSBH) candidate that may be a BBH, a topic we discuss below. We define BBH events as systems where both masses are above $3 M_{\odot}$ at 90% credibility. These 47 events are listed in Table 1. Our chosen FAR threshold ensures a relatively pure sample with only \sim one noise event (see Section 2) and excludes three marginal triggers presented in GWTC-2. Two of these excluded events are BBH candidates (GW190719_215514 and GW190909_114149), and one is an NSBH candidate (GW190426_152155).

The latest observations include a number of individually remarkable events that invite theoretical speculation while providing challenges to existing models. The observation of high-mass binaries such as GW190521 (Abbott et al. 2020e), which has a primary mass $m_1 \sim 85 M_{\odot}$, is in tension with the sharp mass cutoff $m_{\text{max}} = 40.8_{-4.4}^{+11.8} M_{\odot}$ inferred from the GWTC-1 detections, forcing us to reconsider models for the distribution of BH masses in binary systems (Abbott et al. 2020e, 2020f). Here and in the following, the primary mass m_1 refers to the bigger of the two component masses in the binary, while the secondary mass m_2 refers to the smaller of the two. Along with GW190521, GW190602_175927 and GW190519_153544 also have primary masses above $45 M_{\odot}$ at $>99\%$ credibility. These high-mass binaries are interesting from a theoretical perspective, since they occur in the predicted pair-instability gap (Fowler & Hoyle 1964; Barkat et al. 1967; Heger & Woosley 2002; Heger et al. 2003; Woosley & Heger 2015; Belczynski et al. 2016). Additionally, GWTC-2 includes the first systems with confidently asymmetric component masses, including GW190412 with mass ratio $m_2/m_1 \equiv q = 0.28_{0.06}^{+0.12}$ (Abbott et al. 2020a) and GW190814

(Abbott et al. 2020b) with $q = 0.112_{-0.009}^{+0.008}$. Furthermore, the secondary mass of GW190814, $m_2 = 2.59_{0.09}^{+0.08} M_{\odot}$, is near the purported NSBH gap (Bailyn et al. 1998; Farr et al. 2011; Özel et al. 2011), posing a challenge to our understanding of binary formation (Abbott et al. 2020b; Zevin et al. 2020; Mandel et al. 2021). We can gain insight into these exceptional events by studying them in the context of the larger population of compact binaries (Fishbach et al. 2020b).

In particular, studying the enlarged population of BBH events enables us to investigate how compact binaries form.²¹³ Several evolutionary channels have been proposed to explain the origin of the compact binary mergers observed with Advanced LIGO and Advanced Virgo. The isolated binary channel may occur via common-envelope evolution (e.g., Bethe & Brown 1998; Portegies Zwart & Yungelson 1998; Belczynski et al. 2002; Dominik et al. 2015), the remnants of Population III stars (e.g., Madau & Rees 2001; Inayoshi et al. 2017), or chemically homogeneous stellar evolution (e.g., de Mink & Mandel 2016; Mandel & de Mink 2016; Marchant et al. 2016). Evolution via common envelope predicts BBH systems with component masses up to $\sim 50 M_{\odot}$, mass ratios in the range $0.3 \lesssim q < 1$, and nearly aligned spins (Kalogera 2000; Mandel & O’Shaughnessy 2010; Dominik et al. 2013; Eldridge et al. 2017; Giacobbo et al. 2017; Olejak et al. 2020).

In the chemically homogeneous scenario, BBH systems are expected to form with nearly equal-mass components, in addition to aligned spins and component masses in the range ~ 20 – $50 M_{\odot}$. In isolated formation scenarios, component BHs form via stellar collapse and are thus not expected to occur within the pair-instability mass gap, ~ 50 – $120 M_{\odot}$, but may populate either side of the gap.

Alternatively, BBH mergers could form via dynamical interactions in young stellar clusters, globular clusters, or nuclear star clusters (e.g., Kulkarni et al. 1993; Sigurdsson & Hernquist 1993; Portegies Zwart & McMillan 2000); triple systems (e.g., Antonini et al. 2014; Kimpson et al. 2016; Antonini et al. 2017; Vigna-Gómez et al. 2021); or the disks of active galactic nuclei (e.g., McKernan et al. 2012; Bartos et al. 2017; Stone et al. 2017; Fragione et al. 2019). Dynamical formation in dense stellar clusters typically produces an isotropic distribution of spin directions (e.g., Rodriguez et al. 2016; Vitale et al. 2017b) and may enable hierarchical mergers characterized by relatively high-mass binaries (e.g., Antonini & Rasio 2016; Mapelli 2016; McKernan et al. 2018; Rodriguez et al. 2018; Arca Sedda et al. 2020) and large BH spins

²¹³ For the sake of brevity, we refer throughout to “BBHs” when we really mean “merging BBHs.” It is possible that nonmerging BBHs have different properties from those that merge.

Table 1
A Summary of the Events Included in This Analysis

Event	$m_1 (M_\odot)$	$m_2 (M_\odot)$	FAR (yr^{-1})
GW150914	$35.7^{+4.7}_{-3.1}$	$30.6^{+3.0}_{-4.4}$	$<1.0 \times 10^{-7}$
GW151012	$23.4^{+15.1}_{-5.6}$	$13.6^{+4.1}_{-4.9}$	7.9×10^{-3}
GW151226	$13.7^{+8.7}_{-3.2}$	$7.7^{+2.2}_{-2.6}$	$<1.0 \times 10^{-7}$
GW170104	$31.2^{+7.3}_{-3.8}$	$20.0^{+4.9}_{-4.7}$	$<1.0 \times 10^{-7}$
GW170608	$10.9^{+5.5}_{-1.7}$	$7.6^{+2.4}_{-2.2}$	$<1.0 \times 10^{-7}$
GW170729	$51.9^{+16.5}_{-10.8}$	$33.9^{+10.2}_{-10.4}$	2.0×10^{-2}
GW170809	$35.2^{+8.5}_{-6.0}$	$23.8^{+5.3}_{-5.2}$	$<1.0 \times 10^{-7}$
GW170814	$30.6^{+5.6}_{-3.0}$	$25.3^{+2.8}_{-4.1}$	$<1.0 \times 10^{-7}$
*GW170817	$1.6^{+0.3}_{-0.2}$	$1.2^{+0.2}_{-0.2}$	$<1.0 \times 10^{-7}$
GW170818	$35.4^{+7.5}_{-4.7}$	$26.7^{+3.3}_{-3.2}$	4.2×10^{-5}
GW170823	$40.0^{+11.5}_{-7.1}$	$29.1^{+7.2}_{-8.4}$	$<1.0 \times 10^{-7}$
GW190408_181802	$24.6^{+3.2}_{-3.4}$	$18.4^{+3.3}_{-3.6}$	$<1.0 \times 10^{-5}$
GW190412	$30.1^{+4.7}_{-5.1}$	$8.3^{+1.6}_{-0.9}$	$<1.0 \times 10^{-5}$
GW190413_052954	$34.7^{+12.6}_{-8.1}$	$23.7^{+7.3}_{-6.7}$	7.2×10^{-2}
GW190413_134308	$47.5^{+13.5}_{-10.7}$	$31.8^{+11.7}_{-10.8}$	4.4×10^{-2}
GW190421_213856	$41.3^{+10.4}_{-6.9}$	$31.9^{+8.0}_{-8.8}$	7.7×10^{-4}
GW190424_180648	$40.5^{+11.1}_{-7.3}$	$31.8^{+7.6}_{-7.7}$	7.8×10^{-1}
*GW190425	$2.0^{+0.6}_{-0.3}$	$1.4^{+0.3}_{-0.3}$	7.5×10^{-4}
GW190503_185404	$43.3^{+9.2}_{-8.1}$	$28.4^{+7.7}_{-8.0}$	$<1.0 \times 10^{-5}$
GW190512_180714	$23.3^{+5.3}_{-3.8}$	$12.6^{+3.6}_{-3.5}$	$<1.0 \times 10^{-5}$
GW190513_205428	$35.7^{+9.5}_{-9.2}$	$18.0^{+7.7}_{-4.1}$	$<1.0 \times 10^{-5}$
GW190514_065416	$39.0^{+14.7}_{-8.2}$	$28.4^{+9.3}_{-8.8}$	5.3×10^{-1}
GW190517_055101	$37.4^{+11.7}_{-7.6}$	$25.3^{+7.7}_{-7.3}$	5.7×10^{-5}
GW190519_153544	$66.0^{+10.7}_{-12.0}$	$40.5^{+11.0}_{-11.1}$	$<1.0 \times 10^{-5}$
GW190521	$95.3^{+18.7}_{-18.0}$	$69.0^{+22.7}_{-23.1}$	2.0×10^{-4}
GW190521_074359	$42.2^{+5.9}_{-4.8}$	$32.8^{+5.4}_{-6.4}$	$<1.0 \times 10^{-5}$
GW190527_092055	$36.5^{+16.4}_{-9.0}$	$22.6^{+10.5}_{-8.1}$	6.2×10^{-2}
GW190602_175927	$69.1^{+15.7}_{-13.0}$	$47.8^{+14.3}_{-17.4}$	1.1×10^{-5}
GW190620_030421	$57.1^{+16.0}_{-12.7}$	$35.5^{+12.2}_{-12.3}$	2.9×10^{-3}
GW190630_185205	$35.1^{+5.9}_{-5.6}$	$23.7^{+5.2}_{-5.1}$	$<1.0 \times 10^{-5}$
GW190701_203306	$53.9^{+11.8}_{-8.0}$	$40.8^{+8.7}_{-12.0}$	1.1×10^{-2}
GW190706_222641	$67.0^{+14.6}_{-16.2}$	$38.2^{+14.6}_{-13.3}$	$<1.0 \times 10^{-5}$
GW190707_093326	$11.6^{+3.3}_{-1.7}$	$8.4^{+1.4}_{-1.7}$	$<1.0 \times 10^{-5}$
GW190708_232457	$17.6^{+4.7}_{-2.3}$	$13.2^{+2.0}_{-2.7}$	2.8×10^{-5}
GW190720_000836	$13.4^{+6.7}_{-3.0}$	$7.8^{+2.3}_{-2.3}$	$<1.0 \times 10^{-5}$
GW190727_060333	$38.0^{+9.5}_{-6.2}$	$29.4^{+7.1}_{-8.4}$	$<1.0 \times 10^{-5}$
GW190728_064510	$12.3^{+7.2}_{-2.2}$	$8.1^{+1.7}_{-2.6}$	$<1.0 \times 10^{-5}$
GW190731_140936	$41.5^{+12.2}_{-9.0}$	$28.8^{+9.7}_{-9.5}$	2.1×10^{-1}
GW190803_022701	$37.3^{+10.6}_{-7.0}$	$27.3^{+7.8}_{-8.2}$	2.7×10^{-2}
†GW190814	$23.2^{+1.1}_{-1.0}$	$2.59^{+0.08}_{-0.09}$	$<1.0 \times 10^{-5}$
GW190828_063405	$32.1^{+5.8}_{-4.0}$	$26.2^{+4.6}_{-4.8}$	$<1.0 \times 10^{-5}$
GW190828_065509	$24.1^{+7.0}_{-7.2}$	$10.2^{+3.6}_{-2.1}$	$<1.0 \times 10^{-5}$
GW190910_112807	$43.9^{+7.6}_{-6.1}$	$35.6^{+6.3}_{-7.2}$	1.9×10^{-5}
GW190915_235702	$35.3^{+9.5}_{-6.4}$	$24.4^{+5.6}_{-6.1}$	$<1.0 \times 10^{-5}$
GW190924_021846	$8.9^{+7.0}_{-2.0}$	$5.0^{+1.4}_{-1.9}$	$<1.0 \times 10^{-5}$
GW190929_012149	$80.8^{+33.0}_{-33.2}$	$24.1^{+19.3}_{-10.6}$	2.0×10^{-2}
GW190930_133541	$12.3^{+12.4}_{-2.3}$	$7.8^{+1.7}_{-3.3}$	3.3×10^{-2}

Note. Asterisks denote binaries in which both components lie in the NS mass range, while a dagger (†) indicates a system in which the nature of the secondary component is unknown. Both of these classes are excluded from our analyses unless explicitly stated. From left to right, the columns show the event name, the 90% credible interval for primary source mass (units of M_\odot), the 90% credible interval for secondary mass (units of M_\odot), and the minimum available FAR. For events detected in more than one compact binary coalescence (CBC) detection pipeline, we report the lowest of the available FAR estimates. These credible intervals are obtained using a prior that is uniform in redshifted component mass and comoving volume, as in Table 6 of Abbott et al. (2020c).

(Fishbach et al. 2017; Gerosa & Berti 2017). Finally, BBH systems might originate as part of a primordial BH population in the early universe (Carr & Hawking 1974; Carr et al. 2016). Most primordial BH models predict low spins and isotropic spin orientation (Fernandez & Profumo 2019).

Before we continue, we summarize the key questions addressed in the previous analysis of GWTC-1 data (Abbott et al. 2019a) and how the inclusion of O3a events affects our findings.

1. *Are there BBH systems with component masses $\gtrsim 45 M_\odot$?* Following O1 and O2, we inferred that 99% of BBH systems have a primary mass below $m_{99\%} \approx 45 M_\odot$. Moreover, this limit was consistent with a sharp cutoff at $m_{\max} = 40.8^{+11.8}_{-4.4} M_\odot$, hypothesized to correspond to the lower edge of the pair-instability mass gap expected from supernova theory (Woosley & Heger 2015; Heger & Woosley 2002; Heger et al. 2003; Fishbach & Holz 2017; Talbot & Thrane 2018). While the GWTC-2 events remain consistent with $97.1^{+1.7}_{-3.5}\%$ of BBH systems having primary masses below $45 M_\odot$ (inferred using the the POWER LAW + PEAK mass model described in Section 3, or “Model C” from Abbott et al. 2019a), high-mass detections such as GW190521, GW190602_175927, and GW190519_153544 imply a nonzero rate of BBH mergers beyond the $\sim 45 M_\odot$ mass limit. We infer that the merger rate for systems with primary masses in the range $45 M_\odot < m_1 < 100 M_\odot$ is $0.70^{+0.65}_{-0.35} \text{Gpc}^{-3} \text{yr}^{-1}$, consistent with estimates inferred from GWTC-1 (Fishbach et al. 2020b).
2. *Is there a preference for nearly equal component masses?* All of the GWTC-1 observations are consistent with equal-mass binaries, with mass ratios $q \equiv m_2/m_1 = 1$. In O3a, however, we detected two events with mass ratios bounded confidently away from unity, GW190814 and GW190412, though most binaries are consistent with equal mass. The NSBH candidate GW190426_152155, if real, also has unequal component masses, $q = 0.25^{+0.41}_{-0.15}$, but is above the FAR threshold for this work.
3. *Does the merger rate evolve with redshift?* From GWTC-1, we inferred that the BBH merger rate is $53.2^{+55.8}_{-28.2} \text{Gpc}^{-3} \text{yr}^{-1}$, assuming a rate density that is uniform in comoving volume. Allowing for a rate that evolves with redshift (Fishbach et al. 2018), we found that the local merger rate is $\mathcal{R}_{\text{BBH}}(z=0) = 19.7^{+57.3}_{-15.9} \text{Gpc}^{-3} \text{yr}^{-1}$, and that, while still consistent with a uniform-in-comoving-volume model, the rate density is likely increasing with redshift with 93% credibility (Abbott et al. 2019a). With GWTC-2, we are able to more tightly bound the BBH merger rate at $\mathcal{R}_{\text{BBH}} = 23.9^{+14.3}_{-8.6} \text{Gpc}^{-3} \text{yr}^{-1}$ (assuming the POWER LAW + PEAK mass model and a constant-in-comoving-volume merger rate), as well as its evolution with redshift. The data remain consistent with a merger rate that does not evolve with redshift but prefer a rate that increases with redshift (85% credibility). Using the power-law redshift evolution model of Section 3, we find that the merger rate evolves slower than the naive expectation of $(1+z)^{2.7}$ from the local ($z \lesssim 1$) star formation rate (SFR; Madau & Dickinson 2014) at 86% credibility.
4. *How fast do BHs spin?* From GWTC-1, we inferred that the BH spin component aligned with the orbital angular momentum is typically small (Abbott et al. 2016a; Farr et al. 2017, 2018; Tiwari et al. 2018; Abbott et al. 2019a; Wysocki et al. 2019a; Fernandez & Profumo 2019; Roulet & Zaldarriaga 2019; Miller et al. 2020; Roulet et al. 2020). Among the GWTC-1 events, GW151226 is the only event to exhibit unambiguous signs of spin (Abbott et al. 2016b; Vitale et al. 2017a; Kimball et al. 2020a), while a few other events, including GW170729,

show a mild preference for spin (Chatziioannou et al. 2019). We were unable to determine if this typical smallness was because the spin vectors are misaligned, the spin magnitudes are small, or both, although the GWTC-1 data weakly disfavor the scenario in which all spins are perfectly aligned (Farr et al. 2017; Tiwari et al. 2018; Abbott et al. 2019a; Biscoveanu et al. 2020). With additional data, we can now say confidently that some BBH systems have spins misaligned with the orbital angular momentum. A nonzero fraction of systems have measurable in-plane spin components, leading them to undergo precession of the orbital plane. Additionally, 12%–44% of BBH systems merge with a negative effective inspiral spin parameter χ_{eff} (see Equation (5) below), implying that some component spins are tilted by more than 90° relative to the orbital angular momentum axis. We refer to spins tilted more than 90° as *antialigned spins*.²¹⁴ While some events identified in O3a have individually measurable nonzero spin, they occur infrequently, consistent with our previous estimates. We identify nine out of 44 BBH events in GWTC-2 with a positive effective inspiral spin parameter that excludes zero at greater than 95% credibility.²¹⁵ These nine events include both massive BBH systems like GW190519_153544, with a source primary mass $m_1 = 66.0^{+10.7}_{-12.0} M_\odot$ (90% credibility, uniform in redshifted mass prior), and less massive BBH systems like GW190728_064510, with $m_1 = 12.3^{+7.2}_{-2.2} M_\odot$. No individual BBH events are observed with confidently negative effective inspiral spin parameters.

5. *What is the minimum BH mass?* Using GWTC-1, we previously inferred that, if there is a low-mass cutoff in the BBH mass spectrum, it is somewhere below $9 M_\odot$ (Abbott et al. 2019a). With GWTC-2, we tighten the constraints on the minimum BH mass in a BBH system, finding $m_{\text{min}} < 6.6 M_\odot$ (90% credibility). Furthermore, we find that if the BH mass spectrum extends down to $3 M_\odot$, it likely turns over at $\sim 7.8^{+1.8}_{-2.0} M_\odot$. This suggests that there may be a dearth of systems between the NS and BH masses (Fishbach et al. 2020a). However, the O3a observation of GW190814 (Abbott et al. 2020b), with a secondary mass $m_2 = 2.59^{+0.08}_{-0.09} M_\odot$, complicates this picture. If the secondary mass is a BH, it indicates that the BH mass spectrum extends below $3 M_\odot$, to much lower masses than exhibited by the Galactic X-ray binary population (Bailyn et al. 1998; Özel et al. 2011; Farr et al. 2011, but see also Kreidberg et al. 2012; Thompson et al. 2019; Mandel et al. 2021). Alternatively, the secondary object in GW190814 could be an NS, but it would likely have to be significantly spinning to satisfy constraints on the maximum NS mass (Abbott et al. 2020b; Most et al. 2020; Essick & Landry 2020; Tan et al. 2020; Tews et al. 2021; Zhang & Li 2020). Either way, we find that GW190814 is an outlier with respect to the BBH population and the models we consider in this work. Unless stated otherwise, when presenting results on the BBH population, we exclude GW190814.

The remainder of this paper is organized as follows. In Section 2, we describe the data used in this study and detail how we select events for analysis. In Section 3, we provide a high-level overview of our models for the distributions of binary mass, spins, and redshift. In Section 4, we describe the hierarchical method used to fit population models to data. In Section 5, we present key results and discuss the astrophysical implications. Concluding remarks are provided in Section 6. The appendices provide additional details regarding the statistical method (Appendix A) and descriptions of models (Appendix B, D and E), outlier analyses and model checking (Appendix C), and other supplementary material, including a discussion of gravitational lensing (Appendix F). The data release for this paper is available online in Abbott et al. (2020d).

2. Data and Event Selection

Searches for gravitational-wave transients in the O3a data identified 39 candidate events with FARs below 2 yr^{-1} (Abbott et al. 2020c). This FAR cut excludes two BBH candidates and one low-significance NSBH candidate. It is unlikely that the results of our BBH analyses would differ qualitatively with the inclusion of these two additional BBH events because they are typical of other, more confident GWTC-2 detections, and including them would lead to a modest 5% increase in the catalog size. The event list was collated by combining results from several pipelines searching for compact binary mergers using archival data. The search pipelines include `GstLAL` (Messick et al. 2017; Sachdev et al. 2019; Hanna et al. 2020) and `PyCBC` (Allen 2005; Allen et al. 2012; Canton et al. 2014; Usman et al. 2016; Nitz et al. 2017, 2020b), which use template-based matched filtering techniques, and `cWB` (Klimenko & Mitselmakher 2004; Klimenko et al. 2016), which uses a wavelet-based search that does not assume a physically parameterized signal model. These pipelines, along with two additional pipelines, `MBTA` (Adams et al. 2016) and `SPIIR` (Chu 2017), recovered most of the event candidates in low latency.

For the population studies presented here, the event list is further restricted to the 36 events with $\text{FAR} < 1 \text{ yr}^{-1}$ as a means to increase the purity of the sample. This FAR threshold excludes the lower-significance triggers GW190426_152155 (a potential NSBH or BBH candidate), GW190719_215514, and GW190909_114149 that appear in Abbott et al. (2020c). At this FAR threshold, we expect \sim one noise event and therefore a contamination fraction of $\lesssim 3\%$.²¹⁶ In this work, we assume that all of the event candidates that meet this FAR threshold are of astrophysical origin. For the population analysis of the GWTC-1 BBH events, the selection criteria used for inclusion in the study are the FAR and the probability p_{astro} that the source is of astrophysical origin. This value was only computed for BBHs with $\text{FAR} < 2 \text{ yr}^{-1}$ in Abbott et al. (2020c), so we simplify our criterion to only select on FAR. The set of GWTC-1 events that pass this FAR threshold is identical to the previous set chosen by the FAR and p_{astro} . Therefore, while the selection criteria here are different from our GWTC-1 analysis, the analyzed events are consistent.

In addition to the 36 events from O3a that passed the FAR threshold, the 11 detections presented in GWTC-1 (Abbott et al. 2019b) are also included in the event list used here to infer

²¹⁴ Our definition of antialigned does not imply perfect antialignment (tilt angles of exactly 180°), as the phrase is sometimes used in the context of waveform modeling or numerical relativity.

²¹⁵ This result is obtained using a prior informed by the full population of GWTC-2 events. In particular, we employ the GAUSSIAN model described in Section 3.

²¹⁶ In this estimate, we do not include a trial factor penalty for the fact that we look for candidates with multiple pipelines.

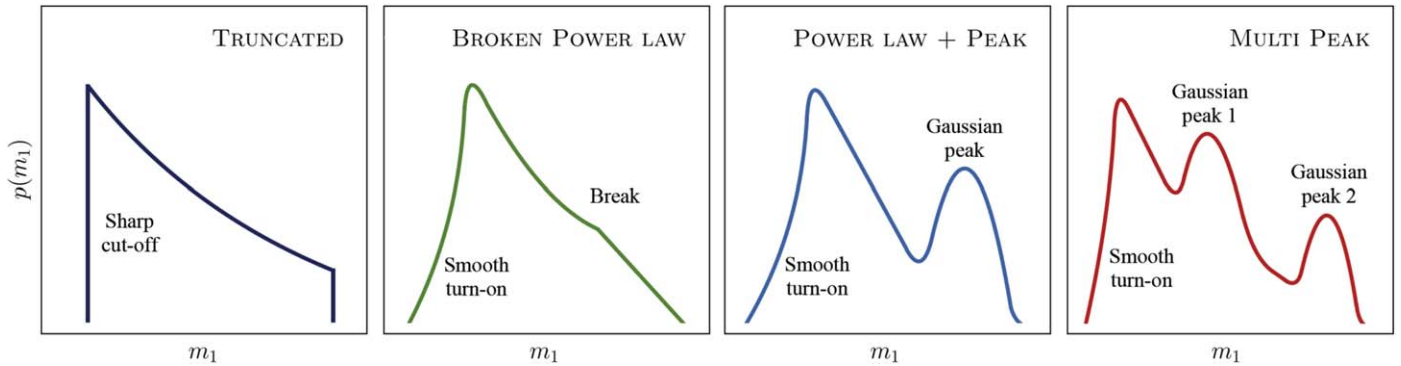


Figure 1. Graphical representations of the various mass distributions described in Section 3.1. MULTISPIN, a model of both mass and spin, is similar to the mass distribution of POWER LAW + PEAK, with a sharp lower-mass cutoff rather than the smooth low-mass turn-on.

the properties of the underlying population. All 47 events used in this analysis are tabulated in Table 1. Of these systems, 44 have both masses confidently in the BH mass range, with $m_1 \geq m_2 > 3 M_\odot$. Unless stated otherwise, we restrict the BBH population results to these 44 (see also Appendix C.3). Since our statistical framework relies on accurately quantifying the selection effects of our search, we only include events identified in GWTC-2, for which we have measured the search sensitivity; see Appendix A. In particular, the event list does not include candidates identified by independent analyses (Nitz et al. 2019, 2020a; Magee et al. 2019; Venumadhav et al. 2019, 2020; Zackay et al. 2019, 2020) of the publicly released LIGO and Virgo data (Abbott et al. 2021). Galaudage et al. (2021) and Roulet et al. (2020) suggested that our results are unlikely to change significantly with the inclusion of these events, and in the future, it may be possible to include events from independent groups using a unified framework for the calculation of significance (Ashton & Thrane 2020; Pratten & Vecchio 2020; Roulet et al. 2020).

Parameter estimation results for each candidate event (Abbott et al. 2020c) were obtained using the LALInference (Veitch et al. 2015; LIGO Scientific Collaboration 2018), RIFT (Lange et al. 2018; Wysocki et al. 2019b), and Bilby (Ashton et al. 2019; Romero-Shaw et al. 2020b) pipelines, the latter employing the `dynesty` nested sampling tool (Speagle 2020). The parameter estimation pipelines use Bayesian sampling methods to produce fair draws from the posterior distribution function of the source parameters, conditioned on the data and given models for the signal and noise (Abbott et al. 2016c).

For the BBH events previously published in GWTC-1, we use the published posterior samples inferred using the IMRPHENOMPV2 (Hannam et al. 2014; Khan et al. 2016; Husa et al. 2016; Bohé et al. 2016) and SEOBNRV3 (Pan et al. 2014; Taracchini et al. 2014; Babak et al. 2017) waveform models. For the new BBH events of GWTC-2, we use waveform approximants that include higher-order multipole content, including IMRPHENOMPV3HM (Khan et al. 2020), NRSUR7DQ4 (Varma et al. 2019), and SEOBNRV4PHM (Bohé et al. 2017; Ossokine et al. 2020). For all events, we average over these waveform families, in contrast to our previously published parameter estimation results for GW190521, which highlighted results from one waveform, NRSUR7DQ4 (Abbott et al. 2020e). A more complete description of the parameter estimation methods and waveform models used can be found in Section V of Abbott et al. (2020c).

3. Population Models

In this section, we provide a high-level overview of the different population models used in this paper. Each model is given a nickname, indicated in bold. There are three categories of models: models for the shape of the mass distribution (Section 3.1), models for the spin distribution (Section 3.2), and models for the redshift distribution (Section 3.3). Readers interested in the astrophysical results may wish to skip ahead to Section 5. In Figure 1, we provide graphical representations of each mass model described below. Additional details about each model are provided in Appendix B, including their mathematical definitions, lists of hyperparameters, and associated prior distributions.

3.1. BH Mass Distribution

1. **TRUNCATED** (four parameters; Appendix B.1). Our simplest mass model, the distribution of primary masses is a power law with hard cutoffs at both low (m_{\min}) and high (m_{\max}) masses. The high-mass cutoff corresponds to the lower edge of the theorized pair-instability gap in the BH mass spectrum (Heger & Woosley 2002; Heger et al. 2003; Woosley & Heger 2015). The mass ratio distribution is also assumed to be a power law (Kovetz et al. 2017; Fishbach & Holz 2017). In Abbott et al. (2019a), it is referred to as “Model B.” This model struggles to accommodate high-mass events like GW190521, necessitating more complicated models.
2. **POWER LAW + PEAK** (eight parameters; Appendix B.2). Similar to the **TRUNCATED MODEL** but with two modifications. At low masses, we implement a smoothing function to avoid a hard cutoff. At high masses, we include a Gaussian peak, initially introduced to model a pileup from pulsational pair-instability supernovae (PPSN; Talbot & Thrane 2018). This model is better able to accommodate the high-mass events that pose a challenge for the **TRUNCATED MODEL**. In Abbott et al. (2019a), it is referred to as “Model C.”
3. **BROKEN POWER LAW** (seven parameters; Appendix B.3). The same as **TRUNCATED** except, instead of a single power law between m_{\min} and m_{\max} , the model allows for a break in the power law at some mass m_{break} . This model includes the low-mass smoothing function used in the **POWER LAW + PEAK** model. The high-mass feature m_{break} may correspond to the onset of pair-instability, and the second power law can be thought of as either a

gradual tapering off or a subpopulation of BHs within the pair-instability mass gap. This model accommodates the high-mass events that pose a challenge for the TRUNCATED MODEL while providing an alternative to the POWER LAW + PEAK model.

4. MULTYPEAK (11 parameters; Appendix B.4). This phenomenological model is similar to POWER LAW + PEAK, except we allow for two peaks. The resulting mass distribution can accommodate hierarchical BBH mergers (Miller & Hamilton 2002b; Gültekin et al. 2004; Antonini & Rasio 2016; Rodriguez et al. 2019), in which second-generation mergers create a second high-mass peak in the BH mass spectrum. We use this model to test if GWTC-2 exhibits evidence for hierarchical mergers.

3.2. Spin Distribution

1. DEFAULT (four parameters; Appendix D.1). This parameterization for the component BH spin magnitudes and tilts was previously used to explore the spin distribution of compact binaries in GWTC-1 (Abbott et al. 2019a). The spin of each component BH in a binary is assumed to be independently drawn from the same underlying distribution. The dimensionless spin magnitude is described using a beta distribution as in Wysocki et al. (2019a). The spin-tilt distribution from Talbot & Thrane (2017) is a mixture model comprising two components: an isotropic component designed to model dynamically assembled binaries and a component in which the spins are preferentially aligned with the orbital angular momentum, as expected for isolated field binaries. The fraction of binaries in the purely aligned subpopulation is denoted as ζ .²¹⁷ For this latter component, the spin-tilt angles are distributed as a TRUNCATED Gaussian with width σ_t that peaks when the BH spin is aligned to the orbital angular momentum. We use this model in concert with the mass models described above.
2. GAUSSIAN (five parameters; Appendix D.2). While the DEFAULT spin model is physically inspired, this model, based on that of Miller et al. (2020), allows us to fit the distribution of phenomenological spin parameters χ_{eff} (the effective inspiral spin parameter; Equation (5)) and χ_p (the effective precession spin parameter; Equation (6)), assuming that their distribution is jointly described as a bivariate Gaussian. The ensemble properties of χ_{eff} and χ_p allow us to conclude that the BBHs in GWTC-2 exhibit general relativistic spin-induced precession of the orbital plane ($\chi_p > 0$), and that some systems have component spins misaligned by more than 90° ($\chi_{\text{eff}} < 0$) relative to the orbital angular momentum.
3. MULTISPIN (12 spin parameters, 10 mass parameters; Appendix D.3). This model allows for multiple subpopulations of BBH systems with distinct mass and spin distributions. Specifically, this model assumes a TRUNCATED power-law mass distribution with the additional presence of a 2D Gaussian subpopulation in m_1 and m_2 , TRUNCATED such that $m_1 \geq m_2$. While similar to the

POWER LAW + PEAK mass model, there is no smooth turn-on, and the mass ratio distribution is allowed to differ between each subpopulation. Most importantly, the two subpopulations have independently parameterized DEFAULT spin distributions. We use this model to test whether the BBH spin distribution varies as a function of mass, as expected if higher-mass systems are the products of hierarchical mergers.

3.3. Redshift Evolution

1. NONEVOLVING (zero parameters). Our default model posits that the merger rate is uniform in comoving volume.
2. POWER-LAW EVOLUTION (one parameter; Appendix E). Following Fishbach et al. (2018), the merger rate density is described by a power law in $(1+z)$, where z is redshift. Given the finite range of Advanced LIGO and Advanced Virgo to BBH mergers, we only expect to constrain the redshift evolution at redshifts $z \lesssim 1$ (Abbott et al. 2013). The farthest event in our analysis is likely GW190706_222641, at redshift $z = 0.71_{-0.27}^{+0.32}$.

4. Method

We adopt a hierarchical Bayesian approach, marginalizing over the properties of individual events to measure the parameters of the population models described above (see, e.g., Mandel et al. 2019; Thrane & Talbot 2019; Vitale 2020). Given the data $\{d_i\}$ from N_{det} gravitational-wave detections, the likelihood of the data given population parameters Λ is (Loredo 2004; Mandel et al. 2019; Thrane & Talbot 2019)

$$\mathcal{L}(\{d\}|\Lambda, N) \propto N^{N_{\text{det}}} e^{-N\xi(\Lambda)} \prod_{i=1}^{N_{\text{det}}} \int \mathcal{L}(d_i|\theta) \pi(\theta|\Lambda) d\theta. \quad (1)$$

Here N is the total number of events expected during the observation period (including both resolvable and unresolvable signals). Each event is described by a set of parameters θ , the likelihood of which is $\mathcal{L}(d|\theta)$. The conditional prior $\pi(\theta|\Lambda)$, meanwhile, is defined by the mass, spin, and redshift models described above in Section 3. It serves to quantify the predicted distribution of event parameters θ given the hyperparameters Λ of the population model. An example of a hyperparameter is the power-law index α governing primary mass distribution $\pi(m_1|\alpha) \propto m_1^{-\alpha}$ for the TRUNCATED mass model. Finally, $\xi(\Lambda)$ is the fraction of binaries that we expect to successfully detect for a population described by the hyperparameters Λ . The procedure for calculating $\xi(\Lambda)$ is described in Appendix A. One of our primary goals in this paper is to constrain the population hyperparameters describing the distribution of gravitational-wave signals. Given a log-uniform prior on N , one can marginalize Equation (1) over N to obtain (Fishbach et al. 2018; Mandel et al. 2019; Vitale 2020)

$$\mathcal{L}(\{d\}|\Lambda) \propto \prod_{i=1}^{N_{\text{det}}} \frac{\int \mathcal{L}(d_i|\theta) \pi(\theta|\Lambda) d\theta}{\xi(\Lambda)}. \quad (2)$$

To evaluate the single-event likelihood $\mathcal{L}(d_i|\theta)$, we use posterior samples that are obtained using some default prior $\pi_{\mathcal{O}}(\theta)$. In this case, integrals over the likelihood can be replaced

²¹⁷ Throughout the paper, the spin tilt is measured at a reference frequency of 20 Hz for all events except GW190521, for which the spin tilt is measured at 11 Hz (see discussion in Abbott et al. 2020c). We verified that for GW190521, the difference between the spin measurements at 20 and 11 Hz are smaller than the systematic uncertainty between the waveform models.

with weighted averages “ $\langle \dots \rangle$ ” over discrete samples. Equation (2), for example, becomes

$$\mathcal{L}(\{d\}|\Lambda) \propto \prod_{i=1}^{N_{\text{det}}} \frac{1}{\xi(\Lambda)} \left\langle \frac{\pi(\theta|\Lambda)}{\pi_{\mathcal{O}}(\theta)} \right\rangle_{\text{samples}}, \quad (3)$$

where the factor of $\pi_{\mathcal{O}}(\theta)$ serves to divide out the prior used for initial parameter estimation. We evaluate the likelihoods for population models using the `emcee`, `dynesty`, and `stan` packages (Foreman-Mackey et al. 2013; Speagle 2020; Carpenter et al. 2017; Riddell et al. 2018). The likelihoods are implemented in a variety of software, including `GWPopulation` (Talbot et al. 2019) and `PopModels` (Wysocki & O’Shaughnessy 2017). The priors adopted for each of our hyperparameters are described in Appendix B.

Throughout this paper, we find it useful to distinguish between the *astrophysical* distribution of a parameter—the distribution as it is in nature—and the *observed* distribution of a parameter—the distribution as it appears among detected events due to selection effects. The posterior population distribution for a given model represents our best guess for the astrophysical distribution of some source parameter θ , averaged over the posterior for population parameters Λ :

$$p_{\Lambda}(\theta) = \int d\Lambda \pi(\theta|\Lambda) p(\Lambda|\{d\}). \quad (4)$$

The subscript Λ indicates that we have marginalized over the population parameters. Meanwhile, the posterior predictive distribution refers to the population-averaged distribution of source parameters θ conditioned on detection.

In Appendices C–E, we provide posterior predictive checks for our population models. These checks consist of comparing simulated sets of N_{obs} “predicted” and “observed” events. For every sample in the model hyperposterior, we generate a set of predicted events by reweighting our found injections to the population model and drawing N_{obs} synthetic events. For each hyperposterior sample, we then generate a set of observed events by reweighting the single-event posteriors of the N_{obs} events to this population prior and drawing one sample per event. Therefore, the inferred distribution of observed events depends on the population model considered. The first example of such a posterior predictive check is shown in Figure 19. We calculate the cumulative distribution function for each set of predicted and observed events in the model hyperposterior and summarize these curves with 90% credibility bands. The uncertainty in the predicted bands comes from uncertainty in the population hyperposterior, as well as Poisson fluctuations, because each cumulative distribution curve consists of N_{obs} simulated events.

Phenomenological models such as we employ here can fail if their assumed form does not adequately represent reality or priors are inappropriately chosen. Inferences from such models are inevitably prone to systematic error, given that the model is unlikely to be a perfect description of reality; for instance, the inferred local rate of BBH mergers is subject to a systematic error associated with our choice of model(s) for the BBH mass distribution. While such errors cannot be eliminated, we take steps to control and minimize their magnitude. First, we carry out posterior predictive checks to make sure our models are consistent with the data. Next, where possible, we check for consistency between models with different assumptions, for

example, looking for common features in the POWER LAW + PEAK and BROKEN POWER-LAW models. Finally, we carry out tests to make sure that our inferences are not artifacts of our model design, for example, by applying the models to simulated uninformative data. Additional information about these tests is provided in Appendix C.

5. Results and Discussion

5.1. Mass Distribution

In this subsection, we report results obtained using the mass models described in Section 3.1 (see Figure 1).²¹⁸ We employ the DEFAULT spin model and the NONEVOLVING redshift model. The results shown here are marginalized over the hyperparameters of the spin distribution.

A TRUNCATED power law fails to fit the high-mass BBH events. The TRUNCATED MODEL applied in Abbott et al. (2019a) measured the sharp high-mass cutoff to be $m_{\text{max}} = 40.8_{-4.4}^{+11.8} M_{\odot}$. When we fit this model to GWTC-2 data, we obtain $m_{\text{max}} = 78.5_{-9.4}^{+14.1} M_{\odot}$, in significant tension ($>99\%$ credibility) with the GWTC-1 result; see Figure 2. The TRUNCATED MODEL struggles to accommodate the high-mass systems of GWTC-2. At 99% credibility, three events of GWTC-2 have $m_1 > 45 M_{\odot}$ (regardless of whether we use a population-informed prior; Fishbach et al. 2020b). This tension remains (at the $>93\%$ credibility level) even when we exclude the highest-mass event, GW190521 (Abbott et al. 2020e, 2020f). The poor fit of the TRUNCATED MODEL is further seen in the posterior predictive check of Figure 19 in Appendix C, which shows that the TRUNCATED MODEL fails to capture the relative excess of observations with $m_1 \sim 30 M_{\odot}$ compared to the number of events with $m_1 \gtrsim 45 M_{\odot}$. Our fit to the TRUNCATED MODEL overpredicts the number of observations with $m_1 > 45 M_{\odot}$ relative to the number of observations with $30 M_{\odot} < m_1 < 45 M_{\odot}$ (98% credibility).

The POWER LAW + PEAK, BROKEN POWER-LAW, and MULTIPLE PEAK models provide better fits to the shape of the mass distribution, particularly at high masses. Although our updated fit to the mass distribution extends to higher masses than the GWTC-1 fit, we find that $97.1_{-3.5}^{+1.7}\%$ of BBH systems have primary masses below $45 M_{\odot}$ (POWER LAW + PEAK model), consistent with the GWTC-1 estimate that 99% of primary masses lie below $\sim 45 M_{\odot}$ (Abbott et al. 2019a; Kimball et al. 2020a). In Table 2, we provide log Bayes factors ($\log_{10} \mathcal{B}$) comparing the mass models. Each Bayes factor is measured relative to the model with the highest Bayesian evidence: POWER LAW + PEAK. In each case, we use the DEFAULT spin model. For context, $\log_{10} \mathcal{B} > 1.5$ is often interpreted as a strong preference for one model over another and $\log_{10} \mathcal{B} > 2$ as decisive evidence (Jeffreys 1961).

While Bayes factors depend on the choice of hyperparameter priors, it is nonetheless possible to see that the TRUNCATED MODEL is disfavored compared to the more complicated models. This inference is driven in part by the fact that, 94% of the time in our posterior predictive checks, the TRUNCATED MODEL overpredicts the number of detections with $m_1 > 50 M_{\odot}$. See

²¹⁸ In this study, we employ models in which the mass and redshift distributions factorize. This is a reasonable assumption for the $z \lesssim 1$ binaries in GWTC-2, and preliminary tests suggest that our data are well fit with this assumption. However, as more binaries are detected from ever-greater distances, it will be interesting to test models that allow for the mass distribution to evolve with redshift.

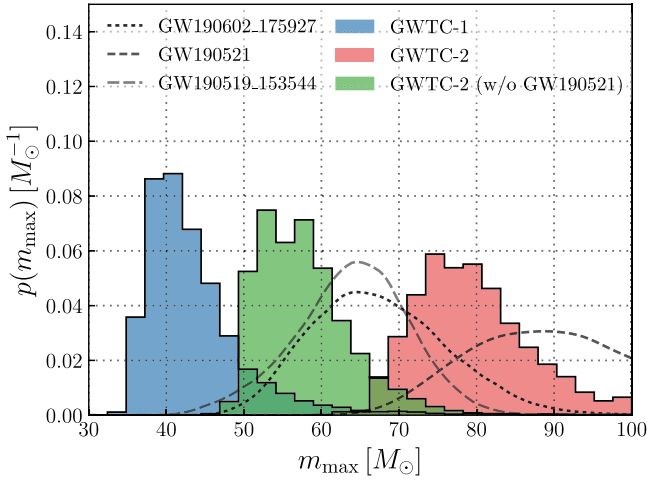


Figure 2. Posterior for the maximum mass using GWTC-1 and fit to the TRUNCATED MODEL (blue), compared to the posterior obtained by adding events from O3a data (red). The two distributions are inconsistent, suggesting that the TRUNCATED MODEL is inadequate. The tension between GWTC-1 and GWTC-2 is somewhat alleviated by the exclusion of the high-mass event GW190521 (green). However, there remain several other high-mass events in O3a. The black dashed lines show primary mass posteriors for the three events in which $m_1 > 45 M_\odot$ at 99% credibility (we employ a prior that is uniform in redshifted masses). These events cause a significant shift in the m_{\max} posterior if we assume a simple power-law fit to the data.

Appendix C for information about the posterior predictive checks. Meanwhile, there is no strong preference for POWER LAW + PEAK over BROKEN POWER LAW or MULTYPEAK. We currently lack the resolving power to determine whether the deviations from the TRUNCATED MODEL are best modeled as a break, a Gaussian peak, or two Gaussian peaks. As a further check, we carried out a follow-up analysis using a hybrid BROKEN POWER LAW + PEAK model, which indicated only modest support for a peak on top of the BROKEN POWER-LAW distribution ($\log_{10} \mathcal{B} = 0.79$).

There are features in the BH mass spectrum beyond a power law. Figure 3 shows the astrophysical merger rate density as a function of primary BH mass for the TRUNCATED, POWER LAW + PEAK, MULTYPEAK and BROKEN POWER-LAW models. Figure 4, meanwhile, shows the posterior predictive distribution for primary masses, including selection effects. Corner plots showing the constraints for the parameters in each model are available in Appendix B; see Figures 16–18. In Appendix C, we show posterior predictive checks for each model (Figures 19 and 23), comparing mock observations predicted by the model to the empirical distribution inferred from GWTC-2.

We turn first to the BROKEN POWER-LAW model (second panel in Figure 3), which is characterized by two spectral indices, α_1 and α_2 , with $p(m_1) \propto m_1^{-\alpha_1}$ for $m_1 < m_{\text{break}}$ and $p(m_1) \propto m_1^{-\alpha_2}$ above the break. We find that the data prefer a break at $m_{\text{break}} = 39.7_{-9.1}^{+20.3} M_\odot$; 90% credible bounds on the location of this break are denoted by the gray vertical band in the second panel of Figure 3. For masses above the break, the BROKEN POWER-LAW model prefers a significantly steeper power-law slope, from $\alpha_1 = 1.58_{-0.86}^{+0.82}$ before to $\alpha_2 = 5.6_{-2.5}^{+4.1}$ after. Figure 5 shows the joint posterior on α_1 and α_2 . We infer that $\alpha_2 > \alpha_1$ at a credibility of 98%. The break aligns with the cutoff m_{\max} inferred with GWTC-1 data (Abbott et al. 2019a), and we speculate that the steep drop-off in the merger rate that

Table 2

Bayes Factors for Each Mass Model Relative to the Favored POWER LAW + PEAK Model, Which Gives the Highest Bayesian Evidence for GWTC-2

Mass Model	\mathcal{B}	$\log_{10} \mathcal{B}$
POWER LAW + PEAK	1.0	0.0
MULTYPEAK	0.5	-0.3
BROKEN POWER LAW	0.12	-0.92
TRUNCATED	0.01	-1.91
POWER LAW + PEAK ($\delta_m = 0$)	0.87	-0.06
BROKEN POWER LAW + PEAK	0.74	-0.13
BROKEN POWER LAW ($\delta_m = 0$)	0.35	-0.46
POWER LAW + PEAK ($\lambda_{\text{peak}} = 0$)	0.05	-1.34

Note. For models that have a smooth turn-on at low masses parameterized by δ_m , we also compare the corresponding submodel with a sharp minimum mass cutoff ($\delta_m = 0$). For the POWER LAW + PEAK model, which includes a fraction λ_{peak} of systems in the Gaussian component, we compare the submodel with $\lambda_{\text{peak}} = 0$. We exclude GW190814 from this analysis.

occurs after m_{break} may be an imprint of PPSN, which are expected to be important for BH masses around $35 M_\odot$ (Heger & Woosley 2002; Heger et al. 2003; Woosley & Heger 2015).

The POWER LAW + PEAK model (third panel of Figure 3) produces a qualitatively similar fit to the one obtained from the BROKEN POWER-LAW model. However, a key feature of the POWER LAW + PEAK model is the Gaussian peak at $33.1_{-5.6}^{+4.0} M_\odot$, denoted by the gray vertical band in the third panel of Figure 3. Evidence for a peak can be seen in Figure 6, which shows the posterior for λ_{peak} , the fraction of systems that belong to the Gaussian component. We see that $\lambda_{\text{peak}} = 0$ (pure power law) is disfavored. It was envisioned (Talbot & Thrane 2018) that the power-law component of the POWER LAW + PEAK model would terminate in the vicinity of this peak to create a high-mass gap. However, in order to accommodate the most massive binaries in GWTC-2, the power law extends to values of $m_{\max} = 86_{-13}^{+12} M_\odot$.

While the mass spectrum must extend to these high masses, we find that 99% of primary BH masses lie below $m_{99\%} \sim 60 M_\odot$; see Table 3. The astrophysical rate density at $\sim 80 M_\odot$ (the primary mass of GW190521) is 2 orders of magnitude lower than the rate density at $\sim 40 M_\odot$. However, because of selection effects, the posterior predictive distribution skews to much higher masses, as seen in Figure 4, so that the probability of detecting at least one event with $m_1 \geq 80 M_\odot$ after observing 44 BBH events drawn from the POWER LAW + PEAK posterior predictive distribution of Figure 4 is high: 32%.

We cannot determine whether the high-mass events of GWTC-2 belong to a distinct subpopulation rather than a high-mass tail of the normal BBH population. An additional subpopulation may be expected if high-mass BHs have a different origin from low-mass ones; for example, if they are the products of hierarchical mergers (Fishbach et al. 2017; Gerosa & Berti 2017; Chatziioannou et al. 2019; Doctor et al. 2020; Kimball et al. 2020a). Using the MULTYPEAK model (fourth panel in Figure 3), which allows for a second high-mass Gaussian component at $m_1 > 50 M_\odot$ in addition to the Gaussian component at $m_1 \lesssim 40 M_\odot$, we find that the addition of a second Gaussian peak is not preferred by the data. The MULTYPEAK model is mildly disfavored compared to POWER LAW + PEAK, with a $\log_{10} \mathcal{B} = -0.3$ (or Bayes factor $\mathcal{B} = 0.5$)

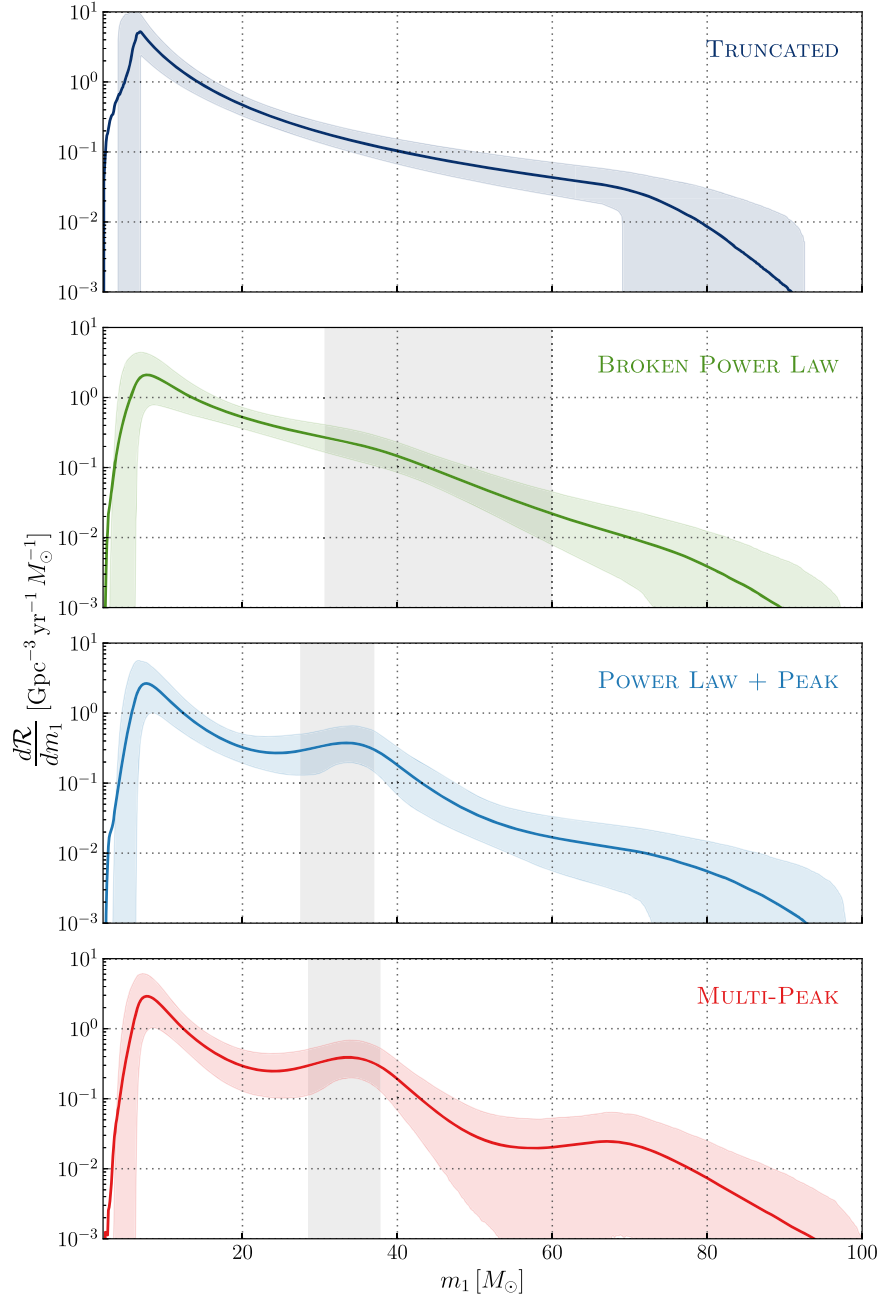


Figure 3. Astrophysical primary BH mass distribution for the TRUNCATED, BROKEN POWER-LAW, POWER LAW + PEAK, and MULTYPEAK models. The solid curve is the posterior population distribution (averaging over model uncertainty), while the shaded region shows the 90% credible interval. While the median rate is always inside the credible region, the solid curve represents the mean, which can be outside the credible region. The first panel (navy) is the TRUNCATED MODEL, the second panel (green) is the BROKEN POWER-LAW model, the third panel (blue) is the POWER LAW + PEAK model, and the fourth panel (red) is the MULTYPEAK model. The TRUNCATED MODEL is disfavored compared to the three latter models that predict a feature at $\sim 40 M_{\odot}$: a break in the mass spectrum in the BROKEN POWER-LAW model or additional Gaussian peaks in the POWER LAW + PEAK and MULTYPEAK models. The vertical gray bands show 90% credible bounds on the locations of these additional features.

for MULTYPEAK relative to POWER LAW + PEAK. Motivated by the hypothesis of hierarchical mergers, we consider a variation of the MULTYPEAK model in which the location of the second peak is required to be at twice the value of the first peak, that is, $\mu_{m,2} = 2\mu_{m,1}$ (see Appendix B.4). Studying the $(\mu_{m,1}, \mu_{m,2})$ panel of the corner plot in Figure 18, we see that the data mildly prefer the second peak at $\approx 70 M_{\odot}$, consistent with twice the value of the first peak at $\approx 35 M_{\odot}$. This “MODIFIED MULTYPEAK” is mildly preferred over the original version by a Bayes factor of ~ 2 . A similar conclusion is found using the

MULTISPIN model; as discussed in Section 5.2, we find hints but no significant evidence for subpopulations with distinct spin distributions. Additional evidence for hierarchical mergers is presented in Kimball et al. (2020b).

Within the framework of the BROKEN POWER-LAW, POWER LAW + PEAK, and MULTYPEAK models, the most massive event, GW190521, appears to be a normal member of the BBH population in the context of the other GWTC-2 events (see Appendix C.2). The event GW190521 is an outlier if we consider it in the context of GWTC-1 with the TRUNCATED

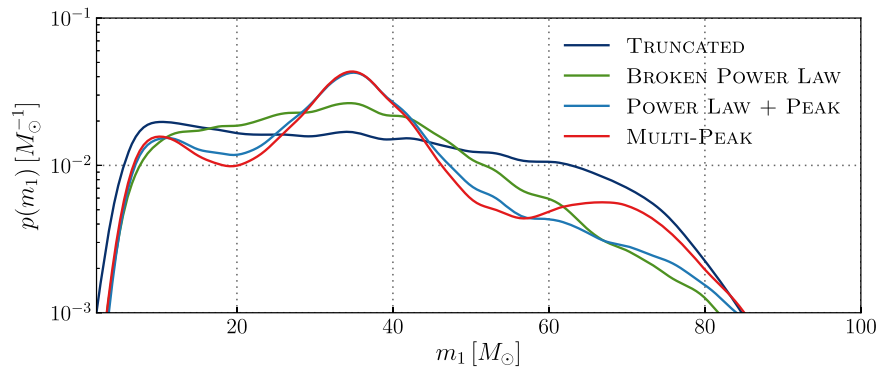


Figure 4. Observed primary BH mass distributions predicted by each mass model. For each model, we average over the uncertainty in the hyperparameter posterior. The observed distribution describes the events successfully detected by LIGO–Virgo, preferentially favoring more massive systems relative to the astrophysical distribution due to selection effects.

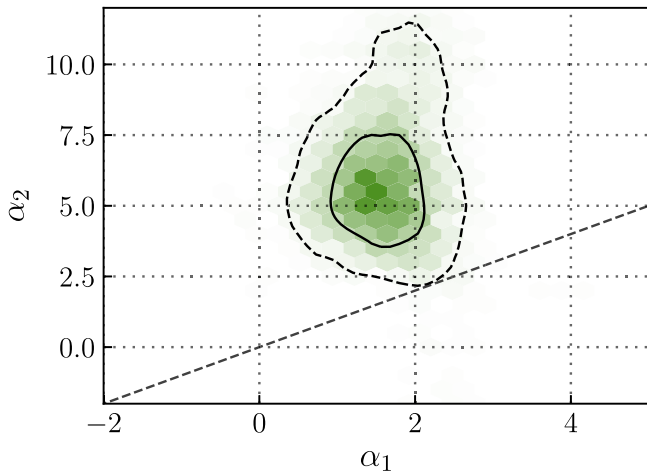


Figure 5. Constraints on the power-law indices governing the primary mass distribution within the BROKEN POWER-LAW model. The parameter α_1 is the power-law index below the break, which is found to be $m_{\text{break}} = 39.7_{-9.1}^{+20.3}$, while α_2 is the index above the break. The dashed and solid contours mark the central 50% and 90% posterior credible regions, respectively, under a flat prior on α_1, α_2 in the range $(-4, 12)$. We rule out with high confidence the hypothesis that $\alpha_1 = \alpha_2$, indicated by the dashed diagonal line, finding $\alpha_2 > \alpha_1$ with 98% credibility.

MODEL, but we interpret this as a limitation of the TRUNCATED MODEL (see Figure 2; Abbott et al. 2020f).

The GWTC-1 detections showed that BHs more massive than $\sim 45 M_\odot$ merge relatively rarely based on simple extrapolations from below $45 M_\odot$. With GWTC-2, we are beginning to resolve the shape of the primary BH mass spectrum above $45 M_\odot$. The implications are not yet clear, but there are intriguing possibilities. One hypothesis is that the events with $m_1 > 45 M_\odot$ are simply the high-mass tail of the ordinary BBH population and do not form through a distinct channel. For example, if the lower edge of the PPSN gap can be modeled as a smooth tapering rather than a sharp cutoff, the feature at $m_{\text{break}} = 39.7_{-9.1}^{+20.3}$ may represent the onset of pair instability. This explanation may pose challenges to our understanding of stellar evolution, since the pair-instability cutoff of BH masses at $\sim 40 M_\odot$ is thought to be relatively abrupt (Woosley et al. 2002; Woosley 2017; Farmer et al. 2019), even though its precise location is uncertain (Giacobbo et al. 2017; Spera & Mapelli 2017; Croon et al. 2020; Farmer et al. 2020; Mapelli et al. 2020; Marchant & Moriya 2020; van Son et al. 2020). If the PPSN cutoff is indeed sharp and all

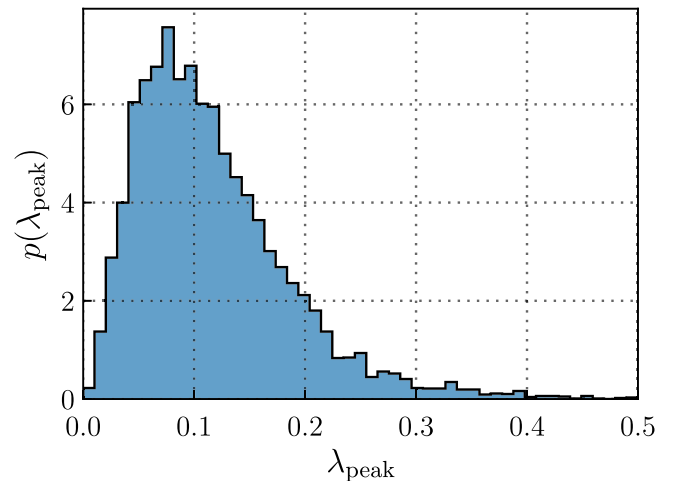


Figure 6. Posterior distribution on the fraction of binaries (λ_{peak}) in the Gaussian component of the POWER LAW + PEAK model under a flat prior on λ_{peak} ; see Appendix B.2. We find that $\lambda_{\text{peak}} = 0$ (which corresponds to no Gaussian peak) is disfavored, supporting the hypothesis that there is a feature in the BH primary mass spectrum.

observed BBH systems lie below the PPSN gap, the cutoff must occur at relatively high masses; in the TRUNCATED MODEL, $m_{\text{max}} = 78.5_{-9.4}^{+14.1} M_\odot$ (or, excluding the most massive event, GW190521, $m_{\text{max}} = 57.0_{-6.6}^{+11.9} M_\odot$). This may have significant implications for nuclear (Farmer et al. 2020) and particle (Croon et al. 2020; Ziegler & Freese 2020) physics.

Another hypothesis is that the events with $m_1 > 45 M_\odot$ constitute a distinct population created, for example, from hierarchical mergers of lower-mass binaries in globular clusters or galactic nuclei (Miller & Hamilton 2002a; Antonini & Rasio 2016; Kimpson et al. 2016; Rodriguez et al. 2018; Yang et al. 2019; Arca Sedda 2020a). Alternatively, the high-mass gap might be populated from low-metallicity stellar mergers in young star clusters, the remnants of which can merge dynamically (Di Carlo et al. 2019, 2020); BH growth through accretion (Roupas & Kazanas 2019; Natarajan 2021; Rice & Zhang 2021; Safarzadeh & Haiman 2020); or Population III stellar remnants with large hydrogen envelopes (Farrell et al. 2021; Liu & Bromm 2020; Tanikawa et al. 2021).

The BBH primary mass distribution exhibits a global maximum between ~ 4 and $\sim 10 M_\odot$. Figure 7 shows the joint posterior for the m_{min} and δ_m parameters inferred using the POWER LAW + PEAK and BROKEN POWER-LAW mass models,

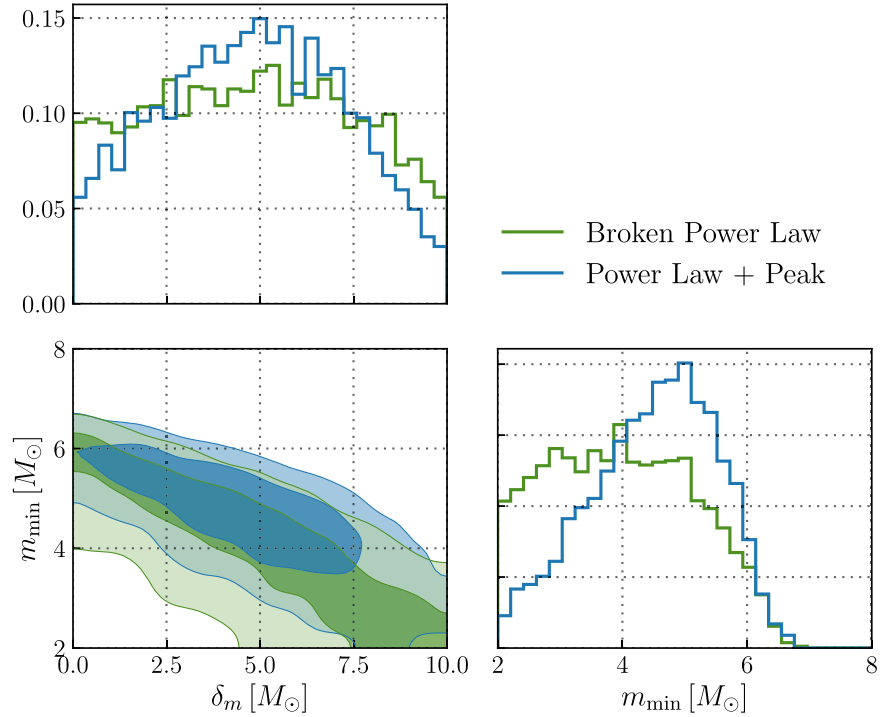


Figure 7. Posterior distribution for population parameters m_{\min} , the minimum BH mass, and δ_m , which controls the sharpness of the low-mass cutoff. A sharp cutoff corresponds to $\delta_m = 0$. Analyzing the 44 BBH events (with the exclusion of GW190814), both models exclude $(m_{\min} = 3 M_{\odot}, \delta_m = 0)$ with $>99\%$ credibility, indicating that the rate drops off at low masses. To varying degrees, both models allow for $m_{\min} \leq 3 M_{\odot}, \delta_m > 0$, suggesting that the low-mass gap may not be empty. See Appendices B.3 and B.2 for additional details about the δ_m, m_{\min} parameters.

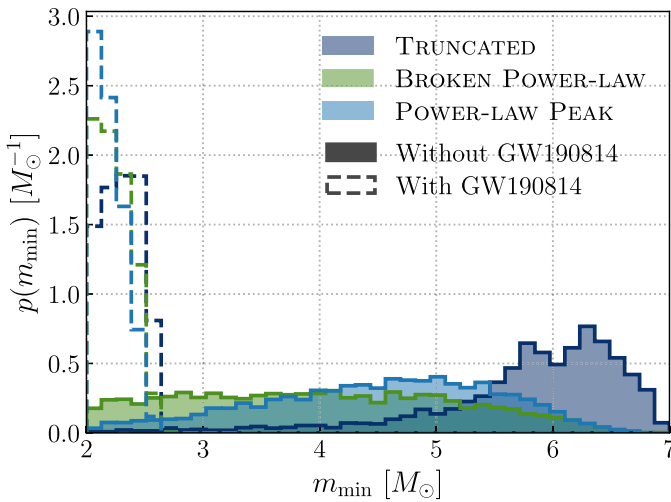
Table 3
The $m_{1\%}$ and $m_{99\%}$ Credible Intervals (90%) for Various Mass Models and Combinations of Events

Events	Mass Model	$m_{1\%} (M_{\odot})$	$m_{99\%} (M_{\odot})$
All confident BBH events, excluding GW190814	TRUNCATED	$6.0^{+0.8}_{-2.1}$	$65.5^{+10.4}_{-9.6}$
	BROKEN POWER LAW	$5.6^{+1.3}_{-1.6}$	$57.8^{+12.5}_{-8.7}$
	POWER LAW + PEAK	$6.0^{+1.0}_{-1.6}$	$59.7^{+13.9}_{-12.8}$
	MULTIPEAK	$6.0^{+1.0}_{-1.6}$	$66.0^{+12.1}_{-16.4}$
All confident BBH events, including GW190814	TRUNCATED	$2.4^{+0.2}_{-0.3}$	$60.3^{+10.1}_{-13.2}$
	BROKEN POWER LAW	$2.6^{+0.5}_{-0.3}$	$56.1^{+12.5}_{-9.0}$
	POWER LAW + PEAK	$2.5^{+0.3}_{-0.3}$	$57.8^{+15.3}_{-14.5}$
	MULTIPEAK	$2.6^{+0.4}_{-0.3}$	$63.8^{+11.2}_{-19.1}$
All confident BBH events, excluding GW190521 and GW190814	TRUNCATED	$5.8^{+0.9}_{-2.8}$	$52.3^{+8.9}_{-5.2}$
	BROKEN POWER LAW	$5.6^{+1.3}_{-1.8}$	$52.3^{+9.5}_{-5.9}$
	POWER LAW + PEAK	$5.9^{+1.0}_{-1.5}$	$52.4^{+13.2}_{-7.0}$
	MULTIPEAK	$6.2^{+0.8}_{-1.5}$	$58.9^{+11.0}_{-11.7}$

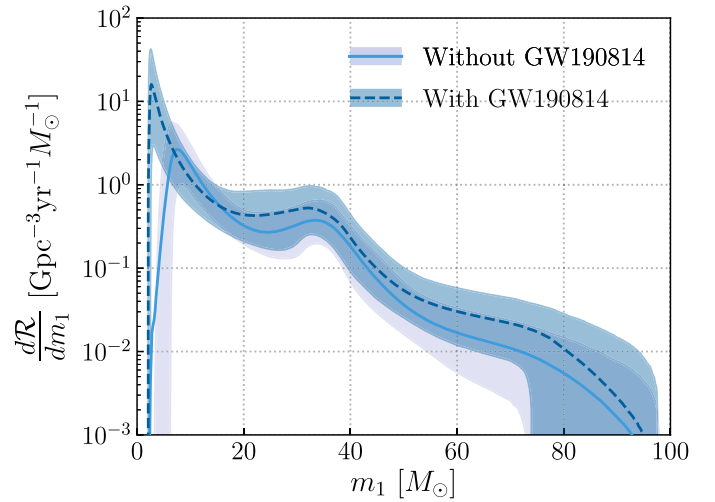
Note. These variables are defined such that, among the astrophysical BBH population, 1% of systems have primary masses $m_1 \leq m_{1\%}$, while 99% have primary masses $m_1 \leq m_{99\%}$. The POWER LAW + PEAK, MULTIPEAK, and BROKEN POWER-LAW models are preferred over the TRUNCATED MODEL.

including only BBH events with $m_2 > 3 M_{\odot}$. Recall that, while the TRUNCATED MODEL has a sharp cutoff at m_{\min} , the remaining models implement a smooth turn-on of width δ_m above m_{\min} , causing the mass spectrum to peak and turn over between m_{\min} and $\delta_m + m_{\min}$ (Talbot & Thrane 2018). Using both the BROKEN POWER-LAW and POWER LAW + PEAK models, we find that the primary mass spectrum does not decrease monotonically from $3 M_{\odot}$. Rather, it turns over at $7.8^{+1.8}_{-2.0} M_{\odot}$ (POWER LAW + PEAK model) or $6.02^{+0.78}_{-1.96} M_{\odot}$ (BROKEN POWER-LAW model). In other words, the mass distribution must turn over at $m_1 > 3 M_{\odot}$ with 99.9%

(assuming the POWER LAW + PEAK model) or 98.5% (BROKEN POWER-LAW model) credibility. As seen in Figure 7, if the BH low-mass cutoff is sharp ($\delta_m = 0$), then $m_{\min} \gtrsim 4 M_{\odot}$. Conversely, if the BH mass spectrum extends below $m_{\min} \lesssim 4 M_{\odot}$, an extended turn-on, $\delta_m \gtrsim 3 M_{\odot}$, is required. These results support the existence of a low-mass gap (or dip) between $\sim 2.6 M_{\odot}$ (the secondary mass of GW190814; the most massive component mass observed below $3 M_{\odot}$) and $\sim 6 M_{\odot}$, strengthening the results from Fishbach et al. (2020a), although we cannot determine whether the low-mass gap is empty.



(a) Minimum primary mass distributions.



(b) POWER LAW + PEAK mass distribution fit.

Figure 8. (a) Posterior distribution for the minimum mass parameter in the TRUNCATED (navy), BROKEN POWER-LAW (green), and POWER LAW + PEAK (blue) models. The solid lines show the posterior for m_{\min} when fitting the models to the confident BBH events excluding GW190814, while the dashed lines show the fits to the confident BBH events including GW190814. The TRUNCATED MODEL is disfavored. (b) Distribution of primary masses inferred using the POWER LAW + PEAK model when including (navy dashed line) and excluding (light blue solid line) GW190814. Only the secondary mass of GW190814 is below $3 M_{\odot}$. However, the primary and secondary mass distributions share a common m_{\min} parameter in all models we consider. The effect of GW190814 on the mass spectrum at low masses inferred using the BROKEN POWER-LAW model is similar.

Since our models do not permit additional features beyond a smooth turn-on to a power law at low masses, they struggle to accommodate GW190814 (with secondary mass at $m_2 = 2.59^{+0.08}_{-0.09}$). We can see this by comparing the mass distribution inferred from the events with $m_1 \geq m_2 > 3 M_{\odot}$, discussed above, to the distribution inferred with GW190814. If GW190814 is a BBH system, the minimum BH mass must extend to $m_{\min} = 2.18^{+0.27}_{-0.16} M_{\odot}$ (see the dashed histograms in Figure 8(a)). In Figure 8(b), we show how the inclusion/exclusion of GW190814 affects the shape of the primary mass distribution below $\lesssim 5 M_{\odot}$. We see that the two distributions are inconsistent at the low-mass end, suggesting that there is a feature in the mass distribution between ~ 2.6 and $\sim 6 M_{\odot}$ that our models cannot capture. This effect can also be seen in the $m_1\%$ values inferred with/without GW190814, shown in Table 3. Assuming the TRUNCATED and POWER LAW + PEAK models, the m_{\min} posteriors inferred with GW190814 lie at the $0.25^{+0.44}_{-0.20}$ and $0.78^{+2.22}_{-0.69}$ percentiles, respectively, of the m_{\min} posteriors obtained without GW190814. Even using the BROKEN POWER-LAW model, which admits greater overlap in the 1D m_{\min} posteriors inferred with/without GW190814, the addition of GW190814 significantly shifts the 2D (δ_m, m_{\min}) posterior and the inferred mass spectrum. Assuming the BROKEN POWER-LAW model with GW190814, the mass at which the mass spectrum turns over is shifted down to $2.59^{+0.78}_{-0.39} M_{\odot}$, which is inconsistent with the turnover mass (the low-mass local maximum) inferred without GW190814, $6.02^{+0.78}_{-1.96} M_{\odot}$. This indicates a failure of our models to fit GW190814 together with the BBH systems of GWTC-2. This finding is supported by additional studies described in Appendix C.3. Because GW190814 is a population outlier with respect to the BBH events of GWTC-2 and our choice of models, we exclude it from the analyses here unless otherwise indicated.

The distribution of mass ratios is broad. The GWTC-1 events are all individually consistent with $q = 1$. Describing the conditional mass ratio distribution as a power law

$p(q|m_1) \propto q^{\beta_q}$, a population analysis of GWTC-1 allowed $\beta_q = 12$ (our maximum prior bound), consistent with a mass ratio distribution sharply peaked at equal-mass pairings (Abbott et al. 2019a; Roulet & Zaldarriaga 2019; Fishbach & Holz 2020b). The first detections of confidently asymmetric systems were seen in GWTC-2: GW190412 (Abbott et al. 2020a) and GW190814 (Abbott et al. 2020b). Excluding GW190814, our reconstruction of the mass ratio distribution is consistent with the results published in Abbott et al. (2020a): $\beta_q = 1.3^{+2.4}_{-1.5}$ for the POWER LAW + PEAK model and $\beta_q = 1.4^{+2.5}_{-1.5}$ for the BROKEN POWER-LAW model. We rule out distributions that are sharply peaked around $q = 1$, with $\beta_q < 2.9$ (POWER LAW + PEAK) and $\beta_q < 3.1$ (BROKEN POWER LAW) at 90% credibility. However, we also disfavor distributions that prefer unequal-mass pairings, with $\beta_q > 0$ at 92% (POWER LAW + PEAK) and 94% (BROKEN POWER LAW) credibility. We find that 90% of systems in the underlying population have mass ratios $q > 0.26^{+0.14}_{-0.08}$.

5.2. Spin Distribution

In this subsection, we highlight the results from the GAUSSIAN, DEFAULT, and MULTISPIN models. We fix the redshift distribution to a NONEVOLVING merger rate. The GAUSSIAN and MULTISPIN models assume the mass distributions described in Appendices D.2 and D.3, respectively. For the DEFAULT spin model, we employ the POWER LAW + PEAK mass model, simultaneously fitting the mass and spin distribution as in the previous subsection.

We observe spin-induced general relativistic precession of the orbital plane. As two BHs merge, the morphology of the resulting gravitational waveform depends on their spins. The spin dependence of a gravitational waveform is determined in part by two phenomenological parameters. First, the effective inspiral spin parameter χ_{eff} quantifies the spin components

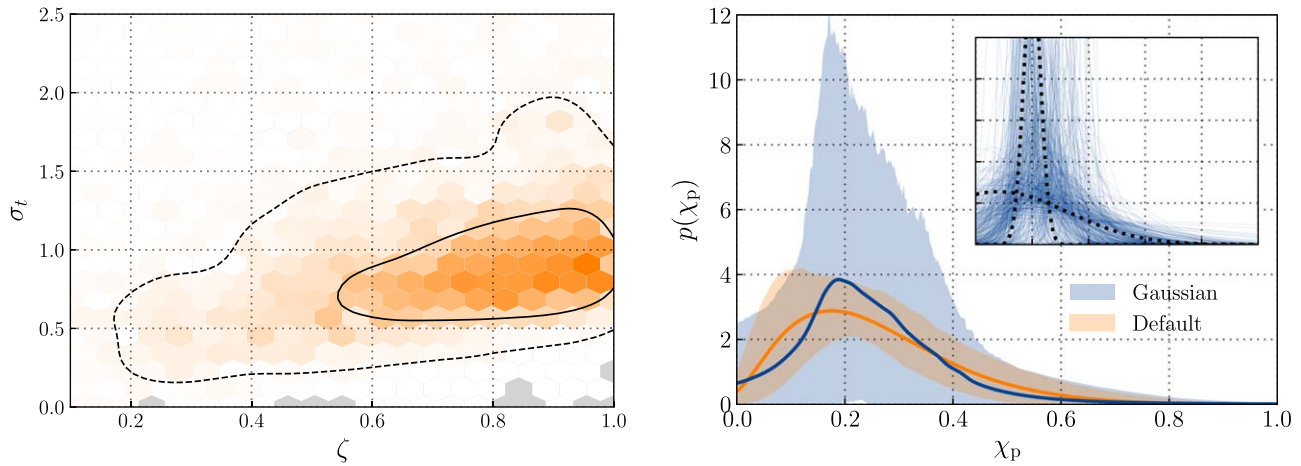


Figure 9. Left: joint posterior on the fraction ζ of BBHs with preferentially aligned spins (vs. isotropic spins) and the spread σ_t of misalignment angles among this population obtained using the DEFAULT spin model (see Appendix D.1 for additional details). We rule out a population with perfectly aligned spins corresponding to $\zeta = 1$ and $\sigma_t = 0$. The gray shaded region represents the region of parameter space inaccessible to our analysis. This region is artificially excluded due to sampling uncertainties, even when analyzing uninformative samples drawn from the spin tilt prior. The dashed and solid contours mark the central 50% and 90% posterior credible regions, respectively, assuming a flat prior on ζ and σ_t . Right: population predictive distributions for the effective precession spin parameter χ_p of BBH systems obtained using the GAUSSIAN (blue) and DEFAULT (orange) spin models. Shaded regions show the central 90% credible bounds on $p(\chi_p)$ at a given spin value, while the solid lines show the median posterior prediction. The inset shows draws of the GAUSSIAN χ_p distributions implied by the posterior on μ_p and σ_p . Broadly, we see support for two possible morphologies, indicated schematically by the dashed black curves. The GWTC-2 is compatible with a χ_p distribution that is either broad and peaked at $\mu_p = 0$ or narrow and centered at $\mu_p \sim 0.2$.

aligned with the orbital angular momentum (Damour 2001):

$$\chi_{\text{eff}} = \frac{\chi_1 \cos \theta_1 + q \chi_2 \cos \theta_2}{1 + q}. \quad (5)$$

Here χ_1 and χ_2 are the dimensionless component spins, defined by $\chi_i = |cS_i/(Gm_i^2)|$, where S_i is the spin angular momentum of component i , and θ_1 and θ_2 are the misalignment angles between the component spins and the orbital angular momentum. Second, spins with components perpendicular to the orbital angular momentum drive relativistic precession of the orbital plane (Apostolatos et al. 1994). The effect is quantified by the effective precession spin parameter (Schmidt et al. 2012; Hannam et al. 2014; Schmidt et al. 2015):

$$\chi_p = \max \left[\chi_1 \sin \theta_1, \left(\frac{4q + 3}{4 + 3q} \right) q \chi_2 \sin \theta_2 \right]. \quad (6)$$

A nonzero value of χ_p indicates the presence of relativistic spin-induced precession of the orbital plane. Although the component spin tilts θ_1 and θ_2 appearing in Equations (5) and (6) generically evolve over the course of a binary inspiral, χ_{eff} and χ_p are themselves approximately conserved quantities (Kidder 1995; Schmidt et al. 2015).

The first unambiguous measurements of BH spin in gravitational-wave astronomy came from analyses of the BBH event GW151226. This system had $\chi_{\text{eff}} > 0$ at 99% credibility, with at least one of its components having a spin magnitude $\chi > 0.2$ and spin misalignment angles consistent with $\theta_1 = \theta_2 = 0$ (Abbott et al. 2016b). While analyses of GWTC-1 found no clear evidence for spin in the other events in GWTC-1 (Miller et al. 2020; but also see Zackay et al. 2019 and Huang et al. 2020), GWTC-1 is collectively inconsistent with a population of nonspinning BHs, if one allows for both spinning and nonspinning subpopulations (Kimball et al. 2020a). Moreover, population analyses of GWTC-1 mildly disfavor the scenario in which all spins are perfectly aligned ($\theta_1 = \theta_2 = 0$), although the degree of misalignment is

degenerate with the spin magnitude distribution (Farr et al. 2017, 2018; Tiwari et al. 2018; Abbott et al. 2019a; Wysocki et al. 2019b).

In GWTC-2, additional BBH events are observed with confidently positive effective inspiral spin parameters. No individual event is observed with confidently negative χ_{eff} (Abbott et al. 2020c). Several events, including GW190521 (Abbott et al. 2020e, 2020f) and GW190412 (Abbott et al. 2020a), show moderate evidence for nonzero χ_p , but no single event unambiguously exhibits spin-induced precession (Abbott et al. 2020c).

Using the DEFAULT model described in Section 3 (see also Appendix D.1), we obtain evidence for nonvanishing spin-orbit misalignment among the population of BBH events in GWTC-2. The DEFAULT model describes the distribution of spin-orbit misalignments as a mixture of two components: a component with isotropically oriented spins and a preferentially aligned component with $z = \cos \theta$ values centered at $z = 0$ (perfect alignment) with a Gaussian spread of width σ_t . In the left panel of Figure 9, we show the joint posterior on σ_t and the fraction ζ of events in the preferentially aligned subpopulation. Perfect alignment corresponds to $\zeta = 1$ and $\sigma_t = 0$. We see that this case is ruled out at $>99\%$ credibility. Thus, either a nonzero fraction of BBH events exhibit isotropically oriented spins or BBH spins are preferentially aligned to their orbits but with a nonvanishing spread. Either case constitutes an observation of in-plane spin components among the BBH population. The gray shaded regions in the left panel of Figure 9 show the values of ζ and σ_t that are artificially excluded by the prior and/or finite sampling effects; the true measurement using GWTC-2 lies well away from this artificial exclusion region.²¹⁹

²¹⁹ In order to determine the artificial exclusion region, we generate prior samples for tilt angles $\theta_{1,2}$ conditioned on the measured values of mass ratio q and spin magnitudes $\chi_{1,2}$. There are no prior samples in the gray shaded regions, which indicates that these regions are artificially excluded due to finite sampling effects.

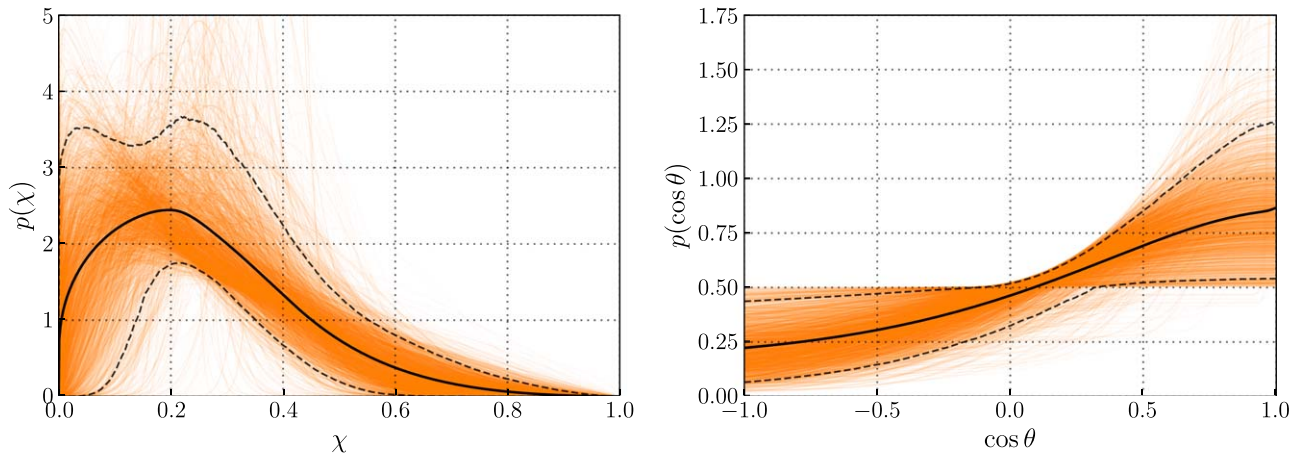


Figure 10. Reconstructions of the BH spin magnitude and tilt distributions. Left: distribution of dimensionless spin magnitude χ as inferred using the DEFAULT spin model (see Appendix D.1). Light orange curves show individual draws from the DEFAULT posterior, while the solid black curve shows the posterior population distribution for χ . Dashed lines mark the central 90% quantiles. Right: reconstructed distribution of tilt angle $\cos \theta_{1,2}$ of BH component spins relative to the orbital angular momenta. An isotropic spin orientation, which corresponds to a uniform distribution in $\cos \theta_{1,2}$, is disfavored but not ruled out. The data do, however, rule out a highly peaked distribution at $\cos \theta_{1,2} = 1$. Rather, the data are consistent with a gently peaked distribution, with a modest preference for aligned spin ($\cos \theta_{1,2} > 0$).

In Figure 10, discussed further below, we plot the range of component spin magnitude and tilt angle distributions recovered using the DEFAULT model. Although the data are consistent with tilt angle distributions that favor alignment, distributions that are highly peaked at $\cos \theta_{1,2} = 1$ are ruled out.

A similar conclusion regarding the presence of in-plane spin components may be drawn using the GAUSSIAN spin model, which imposes an entirely different parameterization for the BH spin distribution and makes different assumptions regarding their masses. In particular, when measuring the mean μ_p and standard deviation σ_p of the χ_p distribution, the case $\mu_p = \sigma_p = 0$ is ruled out at $>99\%$ credibility; fewer than 1% of posterior samples occur at $\mu_p \leq 0.05$ and $\sigma_p \leq 0.05$. Since any nonzero μ_p or σ_p implies the existence of spin-induced precession, this result supports the observation of spin misalignment seen in the DEFAULT model. In the right panel of Figure 9, the blue curve and blue shaded region mark the median and 90% credible bound, respectively, on $p(\chi_p)$ as inferred by the GAUSSIAN model. While the blue shaded region in this figure suggests a χ_p distribution that peaks at ~ 0.2 , there are in fact two morphologies preferred by the data according to the GAUSSIAN model: the recovered χ_p distribution is either broad or narrowly peaked at $\chi_p \approx 0.2$. This is illustrated by the inset, in which we plot an ensemble of distributions corresponding to individual draws from the (μ_p, σ_p) posterior; the dashed black curves highlight traces representative of the two permitted morphologies.

For comparison, the orange curve in the right panel of Figure 9 shows the χ_p distribution implied by the DEFAULT results discussed above. There are several potentially meaningful differences between the results from the GAUSSIAN and DEFAULT models. In particular, the DEFAULT model predicts χ_p distributions that are generally broader and peaked at lower values. This is due to additional physical constraints imposed by the DEFAULT spin model; component spins are presumed to preferentially cluster about $\theta = 0$, an assumption that preferentially favors smaller χ_p values. Nevertheless, the two models agree well within the statistical uncertainties,²²⁰ indicating that

the identification of spin-induced precession is robust to the systematic modeling choices and prior uncertainties.

As mentioned above, GW190521 and GW190412 individually show mild evidence of precession, with the χ_p posteriors shifted away from their respective priors (Abbott et al. 2020a, 2020e, 2020f). To verify that our population-level conclusions are not driven primarily by these two events, we have repeated the GAUSSIAN analysis excluding GW190521 and GW190412. Our results again exclude $\mu_p = \sigma_p = 0$ at a similar level of confidence ($>99\%$ credibility). This implies that the signature of precession observed here is due to the combined influence of many systems with only weakly measured χ_p , consistent with expectations from simulation studies (Fairhurst et al. 2020; Wysocki et al. 2019b).

The injection sets used to quantify search selection effects (see Appendix A) contain only events whose component spins are perfectly aligned with their orbital angular momenta. The results in Figure 9 therefore do not account for systematics possibly affecting our ability to detect events with misaligned spins. The matched filter template banks adopted by the GstLAL and PyCBC search pipelines, for instance, are composed of purely aligned spin waveforms and so may have reduced sensitivity to events with high χ_p (Harry et al. 2016; Calderón Bustillo et al. 2017). Selection effects can, however, only decrease the efficiency with which events with large in-plane spins are detected; incorporating such effects would further shift the posterior in Figure 9 away from $\zeta = 1$ and $\sigma_t = 0$ and/or more strongly rule out a delta function at $\chi_p = 0$. Thus, the presence of in-plane spin components is robust to selection effects. The specific preference for $\mu_p \approx 0.2$, though, may not be. In the future, accurately characterizing the effects of in-plane spins on detection efficiency will be crucial in order to robustly determine the shape of the $\cos \theta$ and χ_p distributions.

We observe antialigned spin, which may suggest the presence of more than one binary formation channel. Using the GAUSSIAN model described in Section 3, we infer the presence of systems with negative effective inspiral spin parameters: $\chi_{\text{eff}} < 0$. Thus, there exist BBH systems with at least one component spin tilted by $\theta > 90^\circ$ relative to the orbital angular momenta. Figure 11 shows posteriors for the

²²⁰ For technical reasons, we do not have a Bayes factor to compare the DEFAULT and GAUSSIAN spin models, though this comparison is possible in principle.

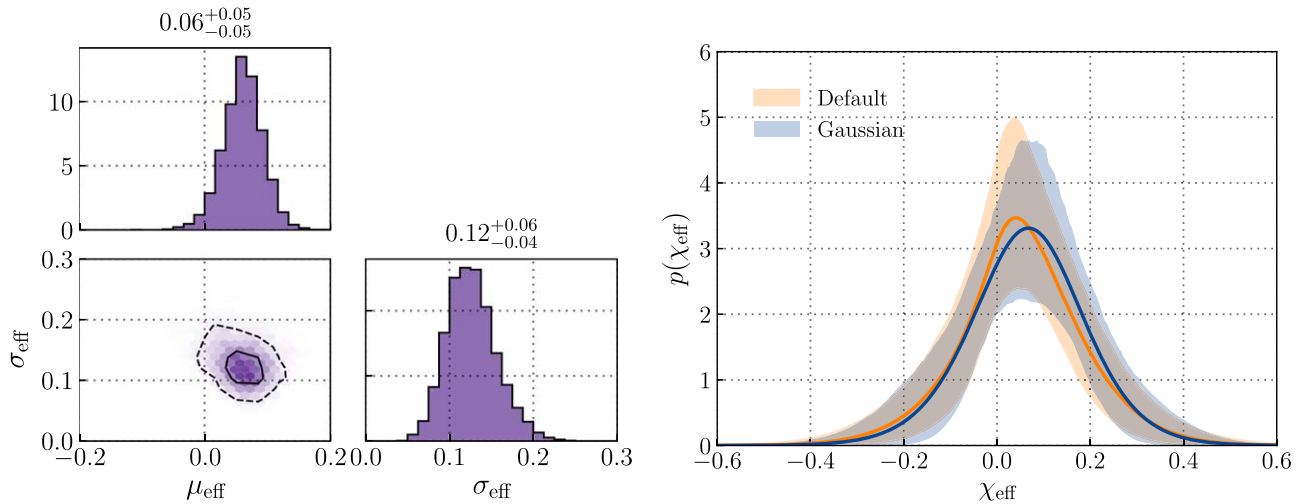


Figure 11. Left: posterior for the mean μ_{eff} and standard deviation σ_{eff} of the BBH χ_{eff} distribution, obtained using the GAUSSIAN model described in Appendix D.2. We marginalize over the parameters governing the distribution of the effective inspiral spin parameter and the effective precession spin parameter. While we infer a χ_{eff} distribution that is peaked at positive values, its measured width implies that a nonzero fraction of BBH systems have negative χ_{eff} , implying component spins misaligned by $t_{1,2} > 90^\circ$ relative to the orbital angular momentum. Right: population predictive distributions for the effective inspiral spin parameter χ_{eff} obtained with both the GAUSSIAN and DEFAULT spin models. Shaded regions show the central 90% credible bounds on $p(\chi_{\text{eff}})$, and the solid lines show the median posterior prediction for the χ_{eff} distribution.

mean μ_{eff} and standard deviation σ_{eff} of the χ_{eff} distribution marginalized over μ_p , σ_p , and the covariance between the effective inspiral spin parameter and the effective precession spin parameter. With a peak at $\mu_{\text{eff}} = 0.06^{+0.05}_{-0.05}$, we find that most systems have a small but positive χ_{eff} , in agreement with the inference from GWTC-1 (Miller et al. 2020; Roulet & Zaldarriaga 2019). With GWTC-2, we can now also constrain the width of the χ_{eff} distribution. The result, $\sigma_{\text{eff}} = 0.12^{+0.06}_{-0.04}$, requires that a nonzero fraction of BBH systems have $\chi_{\text{eff}} < 0$. Unlike the constraints on the χ_p distribution presented above, the results for the presence of negative effective inspiral spin parameters do incorporate selection effects via the prescription described in Section 4.

Analysis with the DEFAULT spin model is also suggestive of an anisotropic distribution of spin orientations. In Figure 10, we plot the population distribution of $\cos\theta_{1,2}$ reconstructed using the DEFAULT model. While the $\cos\theta_{1,2}$ distribution shows a preference for primarily aligned spins, with $\cos\theta_{1,2} > 0$, it also exhibits nonvanishing posterior support for $\cos\theta_{1,2} < 0$, indicating the presence of component spins misaligned by more than 90° . The χ_{eff} distribution inferred with the DEFAULT model closely matches the distribution inferred using the GAUSSIAN model; compare the orange and blue bands in the right panel of Figure 11. The two models therefore agree on the fraction of systems with antialigned component spins.

To further verify that the apparent presence of events with negative χ_{eff} is physical and not an artifact of our choice of models, we repeat our inference of the GAUSSIAN χ_{eff} distribution, this time permitting the minimum allowed effective inspiral spin parameter $\chi_{\text{eff}}^{\text{min}}$ (until now fixed to $\chi_{\text{eff}}^{\text{min}} = -1$) to vary as an additional hyperparameter to be inferred from the data. When fitting for $\chi_{\text{eff}}^{\text{min}}$ alongside μ_{eff} and σ_{eff} , we find that $\chi_{\text{eff}}^{\text{min}}$ is less than zero at 99% credibility (see Figure 27 in Appendix D), confirming that the evidence for antialigned spin is not an artifact of our parameterization. Allowing $\chi_{\text{eff}}^{\text{min}}$ to vary yields similar results for the implied χ_{eff}

distribution and, in particular, the fraction of systems with negative χ_{eff} .

The presence of BBH systems with negative effective inspiral spin parameters carries implications for the formation channels that give rise to stellar-mass BBH mergers. The BBHs born in the field from isolated stellar progenitors are predicted to contain components whose spins are nearly aligned with their orbital angular momenta, although sufficiently strong supernova kicks might produce modest misalignment (O’Shaughnessy et al. 2017; Stevenson et al. 2017; Gerosa et al. 2018; Rodriguez et al. 2016; Bavera et al. 2019). In contrast, binaries assembled dynamically in dense stellar environments are expected to have randomly oriented component spins, yielding positive or negative χ_{eff} with equal probabilities (Kalogera 2000; Mandel & O’Shaughnessy 2010; Rodriguez et al. 2016; Zevin et al. 2017; Rodriguez et al. 2018; Doctor et al. 2020).

Using the posteriors for μ_{eff} and σ_{eff} from Figure 11, in Figure 12, we show posteriors for the implied fractions of BBH systems with negative ($\chi_{\text{eff}} < -0.01$) and positive ($\chi_{\text{eff}} > 0.01$) effective inspiral spin parameters. Motivated by recent work suggesting that BHs are born with natal spins as small as $\chi \approx 10^{-2}$ (Qin et al. 2018; Bavera et al. 2019; Fuller et al. 2019; Fuller & Ma 2019), as well as the tendency of vanishingly small spins to confound efforts to distinguish between positive and negative χ_{eff} (Farr et al. 2018; Abbott et al. 2019a), we include a third bin containing vanishingly small spins in the range $-0.01 \leq \chi_{\text{eff}} \leq 0.01$. At 90% credibility, we find that fractions $f_p = 0.67^{+0.16}_{-0.16}$, $f_n = 0.27^{+0.17}_{-0.15}$, and $f_v = 0.05^{+0.02}_{-0.01}$ of BBH systems have positive, negative, and vanishing χ_{eff} , respectively (see Figure 28 in Appendix D). All three posterior distributions are peaked away from zero. In particular, $f_n > 7\%$ at 99% credibility. This result is in contrast to results obtained using GWTC-1 alone, which did not exhibit a confidently nonzero fraction of events with negative χ_{eff} (Abbott et al. 2019a; Miller et al. 2020). Additionally, the relatively small fraction f_v of binaries with vanishing spins may provide clues about how BHs gain angular momentum, given recent studies suggesting that

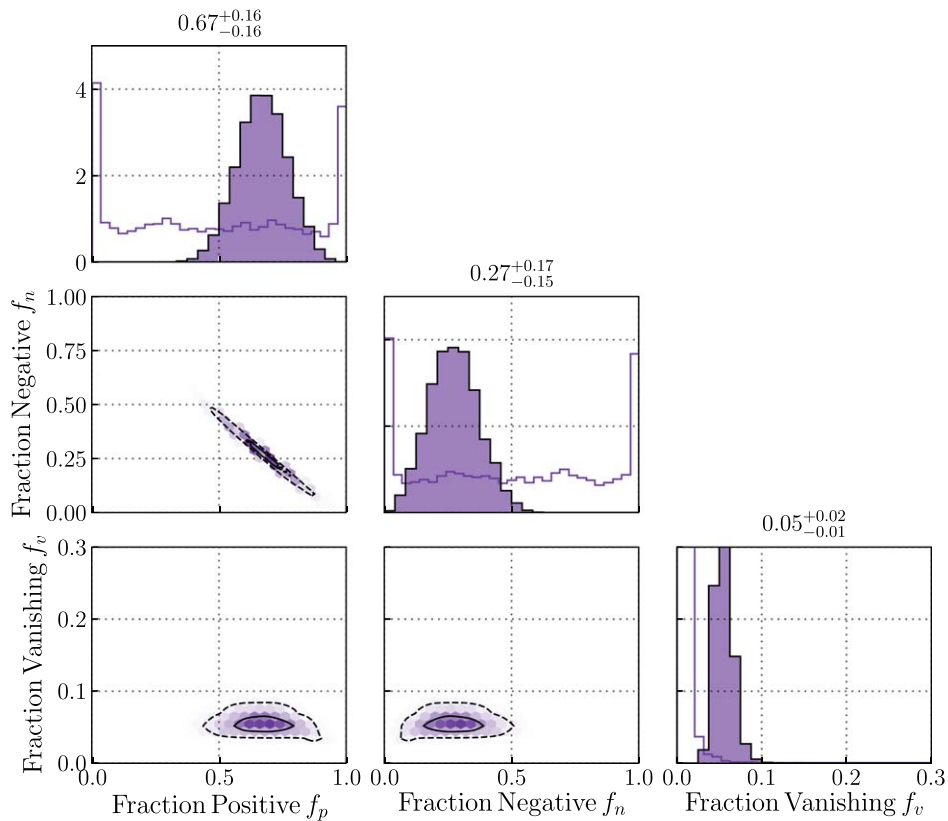


Figure 12. Posterior distribution for the fraction of BBH events with positive or negative χ_{eff} (corresponding to alignment or antialignment of the BH spin with the orbital angular momentum; see Equation (5)). We also include the fraction of events that are consistent with vanishingly small spins $|\chi_{\text{eff}}| < 0.01$. We confidently infer that a nonzero fraction of events have a positive χ_{eff} , which requires at least one component to have a spin tilt less than 90° . A smaller fraction of events have a negative χ_{eff} , which requires at least one component with a spin tilt $>90^\circ$. A nonzero fraction of events have vanishingly small spins. The prior distributions on the parameters are marked with open histograms.

most BHs are born slowly rotating (Fuller & Ma 2019). While we define the vanishing bin to be $-0.01 \leq \chi_{\text{eff}} \leq 0.01$, the exact choice of width for the vanishing bin does not strongly affect the values of f_p and f_n relative to one another. We obtain nearly identical results, albeit with a slightly weaker lower bound on f_n , when we additionally allow the minimum effective inspiral spin $\chi_{\text{eff}}^{\text{min}}$ to vary as described above; in this case, $f_p = 0.65^{+0.17}_{-0.16}$ and $f_n = 0.26^{+0.17}_{-0.21}$.

As mentioned above, dynamical formation in dense clusters is not the only astrophysical explanation of negative effective inspiral spin parameters. If stellar progenitors experience both strong natal kicks in supernovae and inefficient spin realignment, $\lesssim 10\%$ of BBH systems formed through isolated binary evolution may have $\chi_{\text{eff}} < 0$ (Rodríguez et al. 2016; O’Shaughnessy et al. 2017; Stevenson et al. 2017; Wysocki et al. 2018), although these results depend on the poorly understood physics of natal kicks and binary interaction via torques and mass transfer. Moreover, we have so far neglected the possibility of other formation channels that may operate in both the field and dynamical regimes. Isolated hierarchical triples, for example, may produce binary mergers with preferentially in-plane component spins (Antonini et al. 2018; Rodríguez & Antonini 2018; Liu et al. 2019; Fragione & Kocsis 2020). Mergers in the disks of active galactic nuclei, meanwhile, yield component spins that are preferentially parallel or antiparallel to a binary’s orbital angular momentum (McKernan et al. 2018; Yang et al. 2019; McKernan et al. 2020).

With these qualifications in mind, if we interpret negative χ_{eff} as indicative of dynamical formation in stellar clusters, then our constraints on f_n can be used to infer the fraction of dynamically assembled binaries. We assume that dynamical assembly in dense stellar environments yields a χ_{eff} distribution that is symmetric about zero, while isolated binary evolution produces only positive χ_{eff} . Among the binaries with nonnegligible spin (excluding those in the “vanishing” category above), the fractions f_d and f_i of binaries arising from dynamical and isolated channels are

$$f_d = \frac{2f_n}{f_p + f_n}, \quad (7)$$

$$f_i = \frac{f_p - f_n}{f_p + f_n}. \quad (8)$$

We find $0.25 \leq f_d \leq 0.93$ at 90% credibility, suggesting that both the field and the dynamical cluster scenarios contribute to the BBH mergers observed in GWTC-2. Because the relative values of f_n and f_p are not sensitive to the width of the vanishing χ_{eff} bin, this conclusion does not depend strongly on the definition of vanishing spin.

At present, we are unable to include a systematic investigation of waveform error in our analysis of antialigned spin and orbital precession. However, preliminary studies suggest that waveform error is unlikely to significantly affect this and other results in this paper. As described in Abbott et al. (2020c), there is good agreement regarding the parameters of

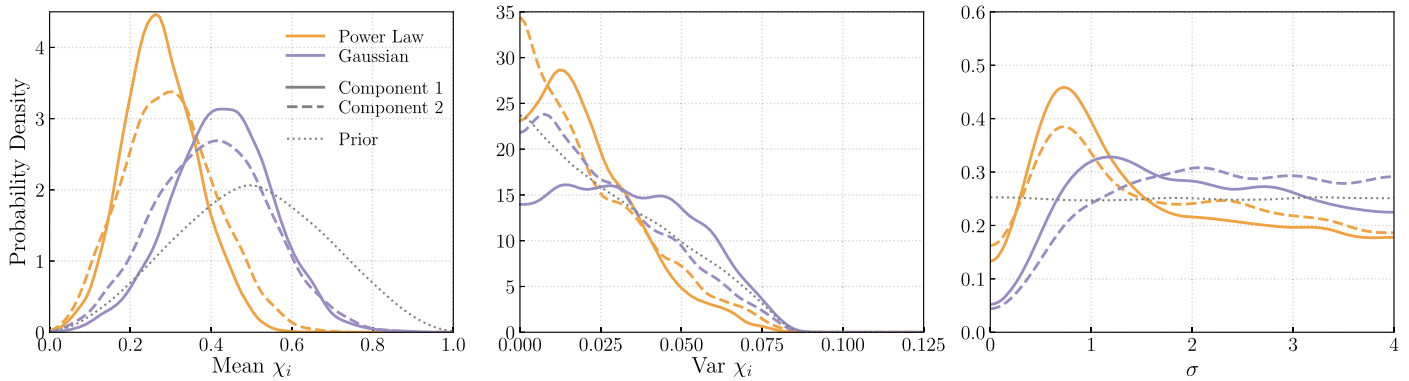


Figure 13. Posterior distribution for the MULTISPIN spin hyperparameters. Each panel corresponds to a different parameter controlling the shape of the spin distribution (see Appendix D.3 for details). Each color corresponds to a different subpopulation (power-law or Gaussian) or component (primary or secondary mass) of the binary. The power-law subpopulation is slightly better measured than the Gaussian component, as a large number of detections are assigned to it. The results hint at a potential correlation between mass and spin, but the large measurement errors mean the spin distributions are consistent between the two subpopulations.

the GWTC-2 events when inferred with different waveforms. There is a caveat: our studies do not include eccentric waveforms. Romero-Shaw et al. (2020a) and Gayathri et al. (2020) suggested that GW190521 may have been eccentric, and Calderón Bustillo et al. (2020) pointed out that eccentricity can be confused with precession for high-mass events. Currently, the only event likely to be affected is GW190521 (Calderón Bustillo et al. 2020). It is not clear how our results would change if we accounted for eccentricity, but we note that eccentricity can be a signature of dynamical assembly (Samsing et al. 2014; Samsing & Ramirez-Ruiz 2017; Lower et al. 2018; Samsing 2018; Fragione & Kocsis 2019; Romero-Shaw et al. 2019; Zevin et al. 2019). We also note that Fishbach & Holz (2020a) and Nitz & Capano (2020) found that GW190521 may be an intermediate mass ratio inspiral, which could potentially alter our conclusions if true. For future work, it would be worthwhile to estimate the systematic error using different waveform approximants.

No strong evidence for variation of the spin distribution with mass. The BHs born in hierarchical mergers inherit the orbital angular momenta of their progenitor systems, leading to significant spin magnitudes $\chi \approx 0.7$ for nearly equal-mass systems (Pretorius 2005; Berti & Volonteri 2008; Fishbach et al. 2017; Rodriguez et al. 2018; Gerosa et al. 2018; Rodriguez et al. 2019; Doctor et al. 2020; Kimball et al. 2020a). If hierarchical mergers are present in GWTC-2, then one may expect correlations between the spins and masses of BBH systems, with more massive hierarchical mergers also possessing larger spins. We use the MULTISPIN model to explore possible trends in the BBH spin distribution with mass, allowing for a distinct low- and high-mass subpopulation (with primary mass distributions parameterized by a power law and Gaussian, respectively; see Section D.3), each with a distinct spin distribution. The low-mass power law has a weak preference for smaller spins, as compared to the high-mass Gaussian. Both subpopulations disfavor perfectly aligned systems, though the low-mass subpopulation has more support for small misalignments. In spite of these differences, the uncertainties on both of these subpopulations are broad enough that the two are fully consistent with each other, and we cannot confidently claim to detect a mass dependence on the spin distribution at this stage. This is demonstrated in Figure 13, which shows the posteriors for the spin distribution hyperparameters associated with each mass subpopulation. These

findings support the results of previous studies on GWTC-1, which could neither exclude nor confidently detect a variation of the spin distribution with mass (Safarzadeh et al. 2020; Tiwari 2020).

5.3. Merger Rate and Redshift Evolution

In this subsection, we use the POWER LAW + PEAK and BROKEN POWER-LAW mass models with the DEFAULT spin model and infer the merger rate using the NONEVOLVING and POWER-LAW evolution redshift models.

We better constrain the BBH merger rate. Assuming a log-uniform prior, we find a BBH merger rate of $R_{\text{BBH}} = 23.9^{+14.3}_{-8.6} \text{ Gpc}^{-3} \text{ yr}^{-1}$ using the POWER LAW + PEAK mass distribution and the assumption of a NONEVOLVING merger rate density. We find that estimates of the BBH merger rate are robust to our choice of mass model, with excellent agreement between the POWER LAW + PEAK, BROKEN POWER-LAW, and MULTIPLEAK models. The TRUNCATED MODEL yields a higher merger rate than the other models, but the results agree within the statistical uncertainties: $R_{\text{BBH}} = 33^{+22}_{-12} \text{ Gpc}^{-3} \text{ yr}^{-1}$. Our BBH merger rate estimate is consistent with the hypothesis that a significant fraction of the merger rate is due to dynamically assembled binaries in globular clusters (Portegies Zwart & McMillan 2000; O’Leary et al. 2006; Moody & Sigurdsson 2009; Downing et al. 2011; Rodriguez et al. 2015; Park et al. 2017; Fragione & Kocsis 2018; Antonini & Gieles 2020), young/open star clusters (Banerjee et al. 2010; Ziosi et al. 2014), nuclear star clusters (O’Leary et al. 2009; Miller & Lauburg 2009; Antonini & Rasio 2016), or active galactic nuclei disks (McKernan et al. 2018; Gröbner et al. 2020; Tagawa et al. 2020).

In Table 4, we show the merger rate in different primary mass bins as inferred with the BROKEN POWER-LAW, POWER LAW + PEAK, and MULTIPLEAK models. Taking the range between the lowest 5% and highest 95% estimate across these three models in each mass bin, we find the merger rate to be $\sim 4\text{--}14 \text{ Gpc}^{-3} \text{ yr}^{-1}$ in the range of $10\text{--}20 M_{\odot}$, $\sim 1.3\text{--}5.3 \text{ Gpc}^{-3} \text{ yr}^{-1}$ in the range of $20\text{--}30 M_{\odot}$, and $\sim 1.3\text{--}5.2 \text{ Gpc}^{-3} \text{ yr}^{-1}$ in the range of $30\text{--}40 M_{\odot}$. In Figure 7, we showed that the primary mass spectrum turns over between 4 and $10 M_{\odot}$. We estimate the merger rate in this range to be $\sim 3\text{--}21 \text{ Gpc}^{-3} \text{ yr}^{-1}$.

Our estimate of the BBH merger rate includes only systems with $m_1 \geq m_2 > 3 M_{\odot}$, which notably excludes GW190814. If we calculate the merger rate for all systems down to

Table 4
Merger Rate Estimate in Different Primary Mass Bins

Mass Model	\mathcal{R} (Gpc ⁻³ yr ⁻¹)			
	$4 M_{\odot} \leq m_1 < 10 M_{\odot}$	$10 M_{\odot} < m_1 < 20 M_{\odot}$	$20 M_{\odot} \leq m_1 < 30 M_{\odot}$	$30 M_{\odot} \leq m_1 < 40 M_{\odot}$
BROKEN POWER LAW	$7.86^{+11.17}_{-4.81}$	$8.89^{+5.29}_{-3.57}$	$3.71^{+1.58}_{-1.1}$	$2.04^{+1.16}_{-0.78}$
POWER LAW + PEAK	$8.91^{+11.28}_{-5.25}$	$7.07^{+4.58}_{-2.98}$	$2.75^{+1.94}_{-1.14}$	$3.05^{+1.86}_{-1.13}$
MULTIPEAK	$9.54^{+11.48}_{-5.78}$	$7.02^{+4.54}_{-3.06}$	$2.6^{+1.88}_{-1.3}$	$3.19^{+2.02}_{-1.22}$

Note. These results assume a NONEVOLVING merger rate density and exclude GW190814 from the analysis.

$m_2 \geq 2 M_{\odot}$ using our models, thereby including GW190814, we infer a higher merger rate: $R_{\text{BBH}} = 52^{+52}_{-26}$ Gpc⁻³ yr⁻¹ for the POWER LAW + PEAK model. The reason for this change is that including GW190814 increases the low-mass rate (see Figure 8(b)). However, because our mass distribution models do not extrapolate well to $m_2 < 3 M_{\odot}$ (see Section 5.1), the fit with GW190814 likely overestimates the rate of systems with masses between ~ 2.6 and $\sim 6 M_{\odot}$. Because of the uncertainty regarding the nature of GW190814 and the low significance of GW190426_152155 (the other NSBH candidate in GWTC-2), we do not attempt to model the NSBH mass distribution and do not calculate an NSBH merger rate. An estimate of the merger rate for GW190814-like systems can be found in Abbott et al. (2020b).

We update the BNS merger rate. We give an update to the BNS rate based on the two confident BNS detections in GWTC-2, GW170817 and GW190425. We estimate a rate of $\mathcal{R}_{\text{BNS}} = 320^{+490}_{-240}$ Gpc⁻³ yr⁻¹ for a population of nonspinning BNSs with component masses uniformly distributed between 1 and $2.5 M_{\odot}$.²²¹ To compute the sensitive spacetime volume of the detector network, we perform a Monte Carlo simulation, drawing BNSs uniformly in comoving volume and source-frame time, and evaluate their detectability with a threshold on the signal-to-noise ratio. The detectability of each simulated system was approximated by requiring a network signal-to-noise ratio above 10 with signal-to-noise ratios above 5 in at least two detectors. We assume a Jeffreys prior on the BNS merger rate, $p(\mathcal{R}) \propto \mathcal{R}^{-1/2}$. Because of the longer observing time and lack of additional detections, we find a slightly smaller value for the BNS rate than previously reported. Assuming that there are 0.01 Milky Way equivalent galaxies (MWEG) in 1 Mpc³ (Kopparapu et al. 2008), this implies a rate of \mathcal{R} MWEG⁻¹ Myr⁻¹.

The BBH merger rate probably increases with redshift but slower than the SFR. Figure 14 shows the merger rate as a function of redshift using the POWER-LAW evolution model (see Appendix E for additional details and Figure 30 for a posterior predictive check). When we allow the merger rate to evolve with redshift according to $(1+z)^{\kappa}$, we find that the $z=0$ merger rate is $\mathcal{R}(z=0) = 19.3^{+15.1}_{-9.0}$ Gpc⁻³ yr⁻¹. The posterior for the rate evolution parameter κ is shown in Figure 15. Since GWTC-2 includes events with greater redshifts than the events in GWTC-1, we obtain a much tighter constraint on the evolution of the merger rate; compare our updated constraints of $\kappa = 1.3^{+2.1}_{-2.1}$ (POWER LAW + PEAK model) and $\kappa = 1.8^{+2.1}_{-2.2}$ (BROKEN POWER-LAW model) to the GWTC-1 result of $\kappa = 8.4^{+9.6}_{-9.5}$. We find that the merger rate is consistent with a nonevolving distribution ($\kappa = 0$) but is more

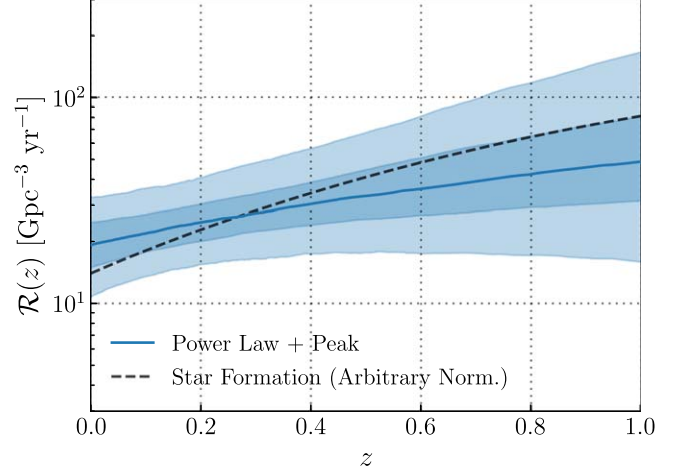


Figure 14. Merger rate density as a function of redshift, fit to the POWER-LAW EVOLUTION model. The solid curve shows the median rate density, while the dark (light) shaded region shows 50% (90%) credible intervals. The dashed curve shows the shape of the SFR. The data exhibit a mild preference for the merger rate to increase with redshift but are consistent with a flat distribution, as well as one that tracks the SFR.

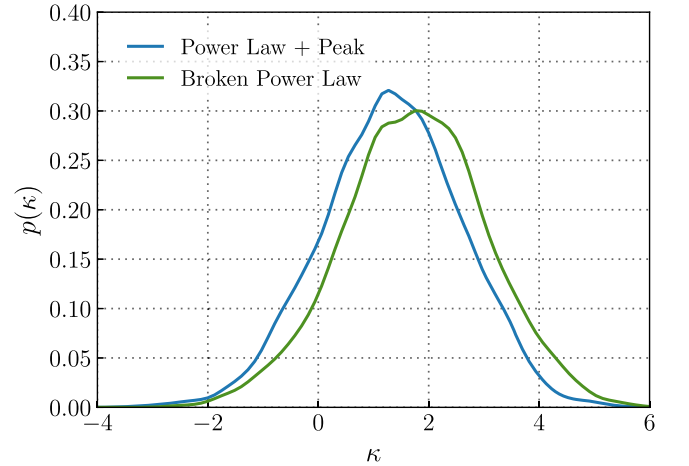


Figure 15. Posterior for the redshift evolution parameter κ from the POWER-LAW EVOLUTION model, which assumes that rate density scales like $(1+z)^{\kappa}$. We assume the POWER LAW + PEAK and BROKEN POWER-LAW mass models and take a flat prior on κ .

likely to increase with increasing redshift, with $\kappa > 0$ at 85% credibility (POWER LAW + PEAK model) or 91% (BROKEN POWER-LAW model).

Locally ($z \approx 0$), the Madau–Dickinson SFR (Madau & Dickinson 2014) corresponds to $\kappa = 2.7$ in our POWER-LAW REDSHIFT parameterization. We infer $\kappa < 2.7$ at 86% credibility with the POWER LAW + PEAK mass model (77% with the BROKEN POWER LAW). Another way of comparing our inferred

²²¹ See Farrow et al. (2019) and Galadage et al. (2021) for fits to the mass distribution of Galactic BNSs.

merger rate to the SFR is by looking at the ratio between the rates at $z = 1$ and 0, $\mathcal{R}_{\text{BBH}}(z = 1)/\mathcal{R}_{\text{BBH}}(z = 0)$. For the SFR, $\mathcal{R}_{\text{SFR}}(z = 1)/\mathcal{R}_{\text{SFR}}(z = 0) \approx 6$, while for BBH systems, we infer $\mathcal{R}_{\text{BBH}}(z = 1)/\mathcal{R}_{\text{BBH}}(z = 0) = 2.5^{+8.0}_{-1.9}$ (POWER LAW + PEAK model). These results are consistent with most astrophysical formation channels, which predict a factor of ~ 2 increase between the merger rates at $z = 0$ and 1 (Santoliquido et al. 2020; Dominik et al. 2013; Mapelli et al. 2017; Rodríguez & Loeb 2018; Baibhav et al. 2019; Eldridge et al. 2019; Neijssel et al. 2019).

6. Conclusions

The publication of the GWTC-2 has increased the population of BBH events by a factor of more than 4. The new catalog has highlighted the limitations of some early population models while yielding remarkable new signatures.

1. We find that the BBH primary mass spectrum is not well described as a simple power law with an abrupt cutoff; there is a strong statistical preference for other models with nontrivial features, such as a peak or tapering. These features occur at $\approx 37 M_{\odot}$, where one might expect pair-instability supernovae (and pulsational pair-instability supernovae) to shape the mass distribution of BHs.
2. At the opposite end of the spectrum, we observe a dearth of systems between the NS and BH masses, suggesting that the BH mass spectrum likely turns over at $\sim 7.8^{+1.8}_{-2.0} M_{\odot}$. We constrain the minimum mass of BHs in BBH systems to be $m_{\text{min}} \lesssim 5.7 M_{\odot}$ at 90% credibility. This is greater than the mass of BH candidates in Galactic binaries, e.g., Thompson et al. (2019). These results hold only when we restrict our analysis to events with both component masses above $3 M_{\odot}$.
3. Meanwhile, we find that our models fail to fit GW190814 together with the BBH systems with both components above $3 M_{\odot}$. This may indicate that GW190814 belongs to a distinct population or that there are additional features at the low-mass end of the BBH mass spectrum that are missing in our models. This is perhaps unsurprising, as the combination of mass ratio, merger rate, and secondary mass inferred from this system pose a challenge to our current understanding of compact binary formation (Abbott et al. 2020b; Arca Sedda 2020b; Zevin et al. 2020; Safarzadeh 2020).
4. We detect clear evidence of spin-induced, general relativistic precession of the orbital plane. We determine that this signature is due not to a single precessing merger but rather the overall preference of the data for precessing waveforms.
5. We observe that some fraction of the BHs in GWTC-2 are spinning with an orientation that is antialigned with respect to the orbital angular momentum of the binary. If we plausibly assume that all binaries with antialigned spins are assembled dynamically, this may imply that LIGO–Virgo events merge both dynamically and in the field. Based on the inferred mass and spin distributions, we find no clear evidence for or against hierarchical mergers in GWTC-2.
6. We compute the rate of compact binary mergers, finding $\mathcal{R}_{\text{BNS}} = 320^{+490}_{-240}$ and $\mathcal{R}_{\text{BBH}} = 23.9^{+14.3}_{-8.6} \text{ Gpc}^{-3} \text{ yr}^{-1}$. The data are consistent with both a merger rate that is constant in time and one that tracks the SFR in the local universe,

though the data prefer a merger rate that is somewhere in between. We find that the merger rate at $z = 1$ differs from the merger rate at $z = 0$ by a factor of $\mathcal{R}_{\text{BBH}}(z = 1)/\mathcal{R}_{\text{BBH}}(z = 0) = 2.5^{+8.0}_{-1.9}$, to be compared with the SFR, $\mathcal{R}_{\text{SFR}}(z = 1)/\mathcal{R}_{\text{SFR}}(z = 0) \sim 6$.

While a clearer picture is emerging of the population properties of compact binaries, key questions remain. How do we best characterize the deviations from the power law in the primary BH mass spectrum, and what is the physical origin of these new features? What is the origin of BBH mergers in the high-mass gap: hierarchical mergers, stars producing remnants heavier than expected from pair-instability supernovae theory, or something else? What is the shape of the mass spectrum between NS and BH masses, and does the current dearth of systems between ~ 3 and $\sim 6 M_{\odot}$ represent an empty low-mass gap? If so, do systems like the secondary mass of GW190814 belong to the NS or BH side of the gap? Is the observation of antialigned spins indicative of dynamically assembled binaries? As the sensitivity of LIGO, Virgo, and KAGRA improves, and as more gravitational-wave transients are detected, we expect to begin to answer these questions. As future observations subject our models to increasing scrutiny, it is inevitable that refinements will be required to fit newly resolved features. This cycle of refining models to account for new data will reveal new questions while providing an evolving understanding of the conclusions presented here.

The authors gratefully acknowledge the support of the United States National Science Foundation (NSF) for the construction and operation of the LIGO Laboratory and Advanced LIGO, as well as the Science and Technology Facilities Council (STFC) of the United Kingdom, the Max-Planck-Society (MPS), and the State of Niedersachsen/Germany for support of the construction of Advanced LIGO and construction and operation of the GEO600 detector. Additional support for Advanced LIGO was provided by the Australian Research Council. The authors gratefully acknowledge the Italian Istituto Nazionale di Fisica Nucleare (INFN), the French Centre National de la Recherche Scientifique (CNRS), and the Netherlands Organization for Scientific Research for the construction and operation of the Virgo detector and the creation and support of the EGO consortium. The authors also gratefully acknowledge research support from these agencies, as well as by the Council of Scientific and Industrial Research of India; the Department of Science and Technology, India; the Science & Engineering Research Board (SERB), India; the Ministry of Human Resource Development, India; the Spanish Agencia Estatal de Investigación; the Vicepresidència i Conselleria d’Innovació Recerca i Turisme and the Conselleria d’Educació i Universitat del Govern de les Illes Balears; the Conselleria d’Innovació Universitats; Ciència i Societat Digital de la Generalitat Valenciana and the CERCA Programme Generalitat de Catalunya, Spain; the National Science Centre of Poland; the Swiss National Science Foundation (SNSF); the Russian Foundation for Basic Research; the Russian Science Foundation; the European Commission; the European Regional Development Funds (ERDF); the Royal Society; the Scottish Funding Council; the Scottish Universities Physics Alliance; the Hungarian Scientific Research Fund (OTKA); the French Lyon Institute of Origins (LIO); the Belgian Fonds de la Recherche Scientifique (FRS-FNRS); Actions de Recherche Concertées (ARC) and

Fonds Wetenschappelijk Onderzoek—Vlaanderen (FWO), Belgium; the Paris Île-de-France Region; the National Research, Development and Innovation Office Hungary (NKFIH); the National Research Foundation of Korea; Industry Canada and the Province of Ontario through the Ministry of Economic Development and Innovation; the Natural Science and Engineering Research Council Canada; the Canadian Institute for Advanced Research; the Brazilian Ministry of Science, Technology, Innovations, and Communications; the International Center for Theoretical Physics South American Institute for Fundamental Research (ICTP-SAIFR); the Research Grants Council of Hong Kong; the National Natural Science Foundation of China (NSFC); the Leverhulme Trust; the Research Corporation; the Ministry of Science and Technology (MOST), Taiwan; and the Kavli Foundation. The authors gratefully acknowledge the support of the NSF, STFC, INFN, and CNRS for the provision of computational resources.

We would like to thank all of the essential workers who put their health at risk during the COVID-19 pandemic, without whom we would not have been able to complete this work.

This is LIGO document number LIGO-P2000077.

Appendix A Estimating the Detection Fraction

A key ingredient in Equations (1) and (2) is the detection fraction $\xi(\Lambda)$, the fraction of systems within some prior volume (redshift $z < 2.3$) that we expect to successfully detect. The detection fraction quantifies selection biases, so it is critical to accurately characterize. For a population described by hyperparameters Λ , the detection fraction is

$$\xi(\Lambda) = \int P_{\text{det}}(\theta) \pi(\theta|\Lambda) d\theta. \quad (\text{A1})$$

Here $P_{\text{det}}(\theta)$ is the detection probability: the probability that an event with parameters θ is detectable. The detection probability depends primarily on the masses and redshift of a system and, to a lesser degree, the spins.

We calculate $\xi(\Lambda)$ using injections. We simulate compact binary signals from a reference population and record which ones are successfully detected by the PyCBC and GstLAL search pipelines; see Abbott et al. (2020c). Following Tiwari (2018), Farr (2019), Vitale (2020), and Loredó (2004), the point estimate for Equation (A1) is calculated using a Monte Carlo integral over found injections,

$$\hat{\xi}(\Lambda) = \frac{1}{N_{\text{inj}}} \sum_{j=1}^{N_{\text{found}}} \frac{\pi(\theta_j|\Lambda)}{p_{\text{draw}}(\theta_j)}, \quad (\text{A2})$$

where N_{inj} is the total number of injections, N_{found} is the injections that are successfully detected, and p_{draw} is the probability distribution from which the injections are drawn; see LIGO-Virgo (2020) for additional details. When sampling the population likelihood, we marginalize over the uncertainty in $\hat{\xi}(\Lambda)$ following Farr (2019) and ensure that the effective number of found injections remaining after population reweighting is sufficiently high ($N_{\text{eff}} > 4N_{\text{det}}$).

For the O3a observing period, we use the injection campaign described in Abbott et al. (2020c) and characterize the found injections as those recovered with an FAR below our threshold of 1 yr^{-1} in either PyCBC or GstLAL. For the O1 and O2 observing period, we supplement the O3a pipeline injections with mock injections drawn from the same distribution p_{draw} above. For the

mock injections, we calculate $P_{\text{det}}(m_1, m_2, z, \chi_{1,z}, \chi_{2,z})$ according to the semianalytic approximation described in Abbott et al. (2019a), based on a single-detector signal-to-noise ratio threshold $\rho = 8$ and the ADVANCED LIGO EARLY HIGH NOISE power spectral density curve (Abbott et al. 2013). We combine O1, O2, and O3 injection sets ensuring a constant rate of injections across the total observing time, yielding $N_{\text{inj}} \approx 7.7 \times 10^7$ injections for O3a and $N_{\text{inj}} \approx 7.1 \times 10^7$ for O1 and O2. To control computational costs, not all of the injections are performed in real data. Before injecting, the expected network signal-to-noise ratio of the injections is computed, and the hopeless injections with signal-to-noise ratios < 6 are removed.

Due to the finite number of injections, we approximate Equation (A1) with a fixed spin distribution instead of the distribution implied by Λ . When combining the TRUNCATED, POWER LAW + PEAK, BROKEN POWER-LAW, and MULTIPLE PEAK mass models with the DEFAULT spin distribution, we assume that the aligned spin components $\chi_{1,z}, \chi_{2,z}$ are independently drawn from a uniform distribution $U(-0.5, 0.5)$. By making this approximation, we are in effect ignoring selection effects due to spin. Nevertheless, we expect this approximation to have a negligible impact on the inferred spin distribution compared to the statistical uncertainties. For aligned spin components in the range $(-0.5, 0.5)$, the detection probability varies by no more than a factor of 2 (Ng et al. 2018a). Furthermore, our main conclusions regarding the spin distribution inferred from the DEFAULT model are supported by the GAUSSIAN model, which requires no approximations for spin selection effects. The MULTISPIN model calculates Equation (A1) by calibrating a semianalytic approximation to the list of found injections (Wysocki 2020).

The transfer function between the observed strain and the astrophysical strain is subject to a systematic calibration uncertainty. We neglect this calibration uncertainty in our estimates of the search sensitivity above. For the O3a observing run, the amplitude uncertainty was $\lesssim 3\%$ (Sun et al. 2020), which leads to a $\lesssim 10\%$ systematic uncertainty in the sensitive spacetime volume and the inferred merger rate. This systematic uncertainty is subdominant to our uncertainties from Poisson counting errors.

Appendix B Details of Mass Population Models

In this section, we provide details about the population models described above in Section 3; see also Figure 1. Each subsection includes a table with a summary of the parameters for that model and the prior distribution used for each parameter. The prior distributions are indicated using abbreviations; for example, $U(0, 1)$ translates to uniform on the interval $(0, 1)$, and $\text{LU}(10^{-6}, 10^5)$ translates to log-uniform on the interval $10^{-6}, 10^5$.

B.1. TRUNCATED Mass Model

This model is equivalent to “Model B” in Abbott et al. (2019a). The primary mass distribution for this model follows a power law with spectral index α and a sharp cutoff at the lower end m_{min} and the upper end of the distribution m_{max} :

$$\pi(m_1 | \alpha, m_{\text{min}}, m_{\text{max}}) \propto \begin{cases} m_1^{-\alpha} & m_{\text{min}} < m_1 < m_{\text{max}} \\ 0 & \text{otherwise} \end{cases}. \quad (\text{B1})$$

Table 5
Summary of TRUNCATED Parameters

Parameter	Description	Prior
α	Spectral index for the power law of the primary mass distribution	U(-4, 12)
β_q	Spectral index for the power law of the mass ratio distribution	U(-4, 12)
m_{\min}	Minimum mass of the power-law component of the primary mass distribution	U($2 M_{\odot}$, $10 M_{\odot}$)
m_{\max}	Maximum mass of the power-law component of the primary mass distribution	U($30 M_{\odot}$, $100 M_{\odot}$)

Table 6
The Parameters that Describe the BBH Mass Distribution for Model POWER LAW + PEAK

Parameter	Description	Prior
α	Spectral index for the power law of the primary mass distribution	U(-4, 12)
β_q	Spectral index for the power law of the mass ratio distribution	U(-4, 12)
m_{\min}	Minimum mass of the power-law component of the primary mass distribution	U($2 M_{\odot}$, $10 M_{\odot}$)
m_{\max}	Maximum mass of the power-law component of the primary mass distribution	U($30 M_{\odot}$, $100 M_{\odot}$)
λ_{peak}	Fraction of BBH systems in the Gaussian component	U(0, 1)
μ_m	Mean of the Gaussian component in the primary mass distribution	U($20 M_{\odot}$, $50 M_{\odot}$)
σ_m	Width of the Gaussian component in the primary mass distribution	U($1 M_{\odot}$, $10 M_{\odot}$)
δ_m	Range of mass tapering at the lower end of the mass distribution	U($0 M_{\odot}$, $10 M_{\odot}$)

Meanwhile, the mass ratio $q \equiv m_2/m_1$ follows a power-law distribution with spectral index β_q :

$$\pi(q|\beta_q, m_{\min}, m_1) \propto \begin{cases} q^{\beta_q} & m_{\min} < m_2 < m_1 \\ 0 & \text{otherwise.} \end{cases} \quad (\text{B2})$$

The hyperparameters for this model are summarized in Table 5.

B.2. POWER LAW + PEAK Mass Model

This is equivalent to ‘‘Model C’’ from Abbott et al. (2019a). It is motivated by the idea that the mass loss undergone by pulsational pair-instability supernovae could lead to a pileup of BBH events before the pair-instability gap (Talbot & Thrane 2018). The primary mass distribution is an extension of the TRUNCATED MODEL with the addition of tapering at the lower-mass end of the distribution and a Gaussian component:

$$\pi(m_1|\lambda_{\text{peak}}, \alpha, m_{\min}, \delta_m, m_{\max}, \mu_m, \sigma_m) = [(1 - \lambda_{\text{peak}})\mathfrak{P}(m_1 | -\alpha, m_{\max}) + \lambda_{\text{peak}}G(m_1|\mu_m, \sigma_m)]S(m_1|m_{\min}, \delta_m). \quad (\text{B3})$$

Here $\mathfrak{P}(m_1 | -\alpha, m_{\max})$ is a normalized power-law distribution with spectral index $-\alpha$ and high-mass cutoff m_{\max} . Meanwhile, $G(m_1|\mu_m, \sigma_m)$ is a normalized Gaussian distribution with mean μ_m and width σ_m . The parameter λ_{peak} is a mixing fraction determining the relative prevalence of mergers in \mathfrak{P} and G . Finally, $S(m_1, m_{\min}, \delta_m)$ is a smoothing function that rises from zero to 1 over the interval $(m_{\min}, m_{\min} + \delta_m)$,

$$S(m|m_{\min}, \delta_m) = \begin{cases} 0 & (m < m_{\min}) \\ [f(m - m_{\min}, \delta_m) + 1]^{-1} & (m_{\min} \leq m < m_{\min} + \delta_m), \\ 1 & (m \geq m_{\min} + \delta_m) \end{cases} \quad (\text{B4})$$

with

$$f(m', \delta_m) = \exp\left(\frac{\delta_m}{m'} + \frac{\delta_m}{m' - \delta_m}\right). \quad (\text{B5})$$

The conditional mass ratio distribution in this model also includes the smoothing term:

$$\pi(q|\beta, m_1, m_{\min}, \delta_m) \propto q^{\beta_q} S(qm_1|m_{\min}, \delta_m). \quad (\text{B6})$$

The hyperparameters for this model are summarized in Table 6.

In Figure 16, we provide a corner plot representation of the posterior distribution for the POWER LAW + PEAK hyperparameters. The $(\mu_m, \lambda_{\text{peak}})$ panel describes the Gaussian component: μ_m is the center of the Gaussian, while λ_{peak} is the fraction of mergers taking place in the Gaussian (as opposed to the power-law distribution). Judging from this panel, it appears at first that λ_{peak} peaks close to zero (corresponding to no Gaussian peak). However, if we zoom in as in Figure 6, we see that the posterior for λ_{peak} is peaked clearly away from zero at ~ 0.02 . This is consistent with the large Bayes factor indicating a preference for POWER LAW + PEAK over TRUNCATED.

B.3. BROKEN POWER-LAW Mass Model

This model is an extension of the TRUNCATED MODEL. The primary mass distribution consists of a broken power law. This is motivated by the potential tapering of the primary mass distribution at high masses. Also, the model employs a smoothing function to prevent a sharp cutoff at low masses:

$$\pi(m_1|\alpha_1, \alpha_2, m_{\min}, m_{\max}) \propto \begin{cases} m_1^{-\alpha_1} S(m_1|m_{\min}, \delta_m) & m_{\min} < m_1 < m_{\text{break}} \\ m_1^{-\alpha_2} S(m_1|m_{\min}, \delta_m) & m_{\text{break}} < m_1 < m_{\max} \\ 0 & \text{otherwise.} \end{cases} \quad (\text{B7})$$

Here

$$m_{\text{break}} = m_{\min} + b(m_{\max} - m_{\min}) \quad (\text{B8})$$

is the mass where there is a break in the spectral index and b is the fraction of the way between m_{\min} and m_{\max} at which the primary mass distribution undergoes a break. Meanwhile, $S(m_1, m_{\min}, \delta_m)$ is a smoothing function as in Equation (B4). The conditional mass

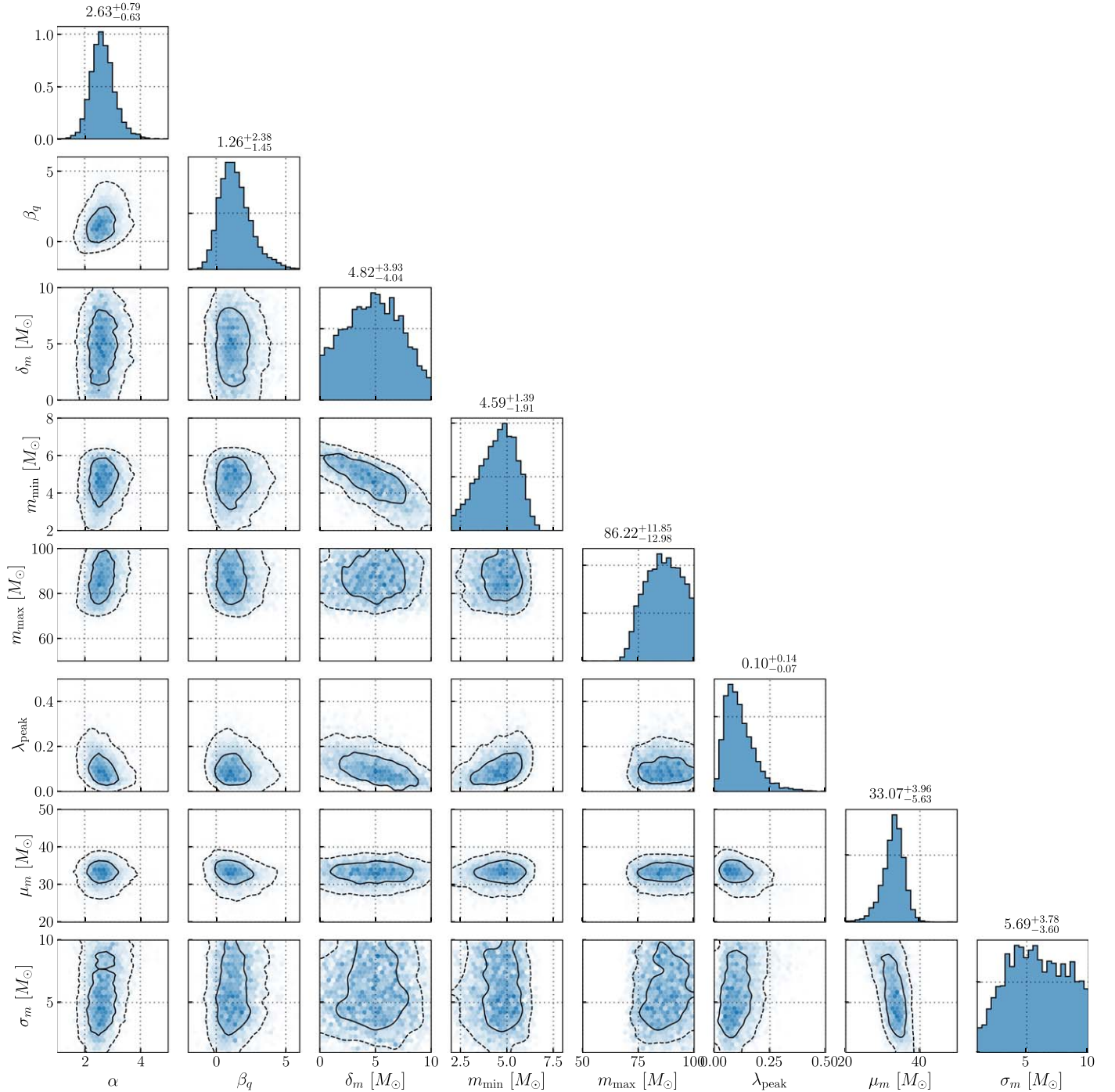


Figure 16. Posterior distribution for the mass hyperparameters for POWER LAW + PEAK. The fit excludes GW190814. The contours represent 50% and 90% credible bounds.

ratio distribution is the same as in the POWER LAW + PEAK model; see Equation (B6). The hyperparameters for this model are summarized in Table 7. In Figure 17, we provide a corner plot for the BROKEN POWER LAW. In the limit of no low-mass smoothing ($\delta_m = 0$), as well as in the limit of a second power law with a steep slope that mimics a sharp cutoff ($m_{\text{break}} = m_{\text{max}}$), this model reduces to the TRUNCATED MODEL. Above, we noted that the BROKEN POWER-LAW model prefers a break in the primary mass spectrum near $40 M_{\odot}$. On the other hand, if we

believe that the feature represented by m_{break} should be closer to a sharp cutoff, then the cutoff must occur at higher masses, approaching the maximum mass of the TRUNCATED MODEL at $m_{\text{max}} = 74.6^{+15.4}_{-8.6} M_{\odot}$. This can be seen by the correlation between b and α_2 in Figure 17.

B.4. MULTIPLEPEAK Mass Model

This model is an extension of POWER LAW + PEAK, where there is an additional Gaussian component at the upper end of

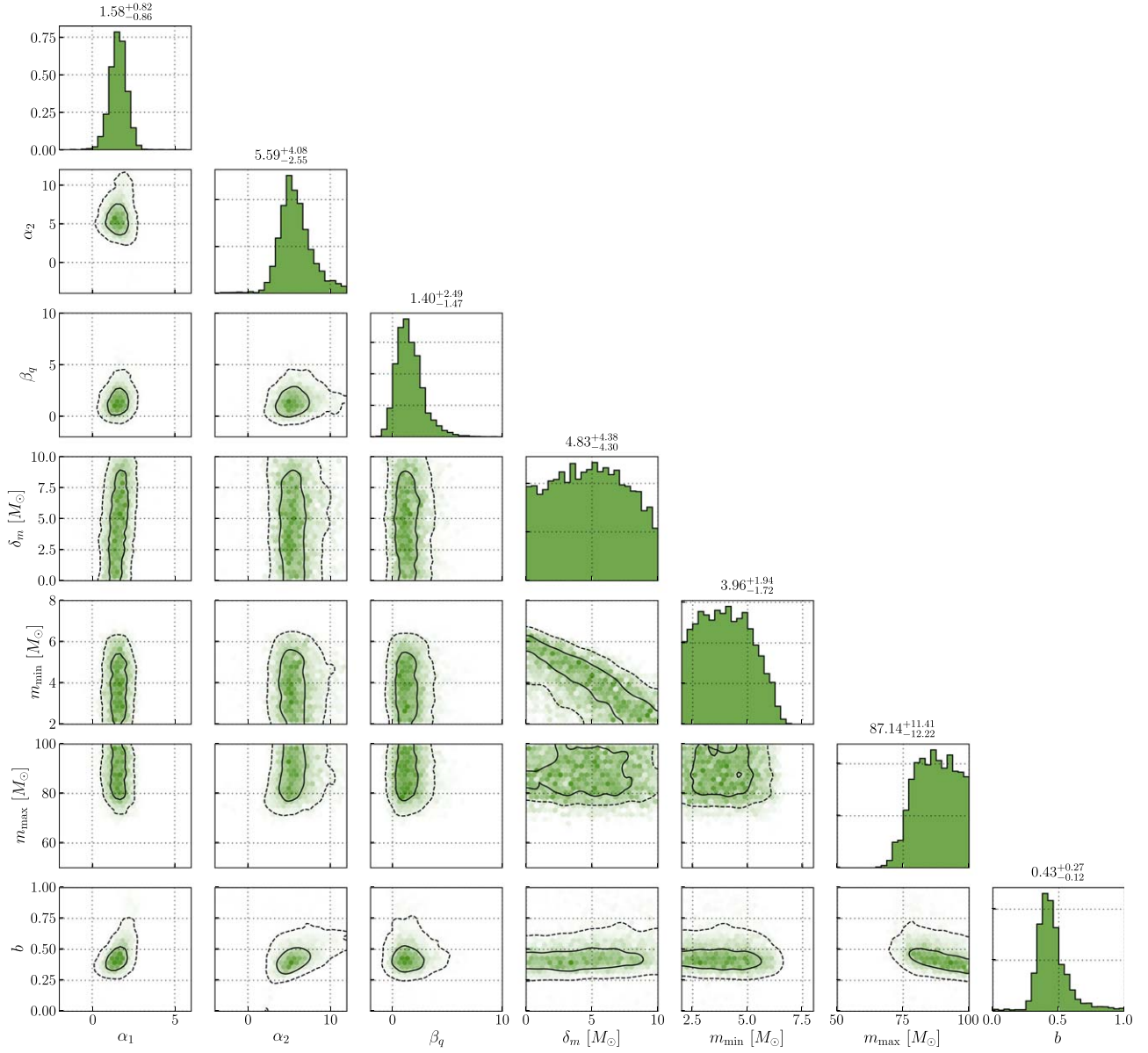


Figure 17. Posterior distribution for mass hyperparameters for a BROKEN POWER LAW. The fit excludes GW190814. The contours represent 50% and 90% credible bounds.

Table 7
Summary of BROKEN POWER-LAW Parameters

Parameter	Description	Prior
α_1	Power-law slope of the primary mass distribution for masses below m_{break}	$U(-4, 12)$
α_2	Power-law slope for the primary mass distribution for masses above m_{break}	$U(-4, 12)$
β_q	Spectral index for the power law of the mass ratio distribution	$U(-4, 12)$
m_{min}	Minimum mass of the power-law component of the primary mass distribution	$U(2 M_{\odot}, 10 M_{\odot})$
m_{max}	Maximum mass of the primary mass distribution	$U(30 M_{\odot}, 100 M_{\odot})$
b	The fraction of the way between m_{min} and m_{max} at which the primary mass distribution breaks (e.g., a break fraction of 0.4 between $m_{\text{min}} = 5$ and $m_{\text{max}} = 85$ means that the break occurs at $m_1 = 32$)	$U(0, 1)$
δ_m	Range of mass tapering on the lower end of the mass distribution	$U(0 M_{\odot}, 10 M_{\odot})$

Table 8
Parameters for the BBH Mass Distribution for Model MULTYPEAK

Parameter	Description	Prior
α	Spectral index for the power law of the primary mass distribution	U(-4, 12)
β_q	Spectral index for the power law of the mass ratio distribution	U(-4, 12)
m_{\min}	Minimum mass of the power-law component of the primary mass distribution	U($2 M_{\odot}$, $10 M_{\odot}$)
m_{\max}	Maximum mass of the power-law component of the primary mass distribution	U($30 M_{\odot}$, $100 M_{\odot}$)
λ	Fraction of BBH systems in the Gaussian components	U(0, 1)
λ_1	Fraction of BBH systems in the Gaussian components belonging to the lower-mass component	U(0, 1)
$\mu_{m,1}$	Mean of the lower-mass Gaussian component in the primary mass distribution	U($20 M_{\odot}$, $50 M_{\odot}$)
$\sigma_{m,1}$	Width of the lower-mass Gaussian component in the primary mass distribution	U($1 M_{\odot}$, $10 M_{\odot}$)
$\mu_{m,2}$	Mean of the upper-mass Gaussian component in the primary mass distribution	U($50 M_{\odot}$, $100 M_{\odot}$)
$\sigma_{m,2}$	Width of the upper-mass Gaussian component in the primary mass distribution	U($1 M_{\odot}$, $10 M_{\odot}$)
δ_m	Range of mass tapering on the lower end of the mass distribution	U($0 M_{\odot}$, $10 M_{\odot}$)

the mass distribution motivated by a possible subpopulation of objects in the upper-mass gap:

$$\begin{aligned} \pi(m_1|\lambda, \alpha, m_{\min}, \delta_m, m_{\max}, \mu_m, \sigma_m) \\ = [(1 - \lambda)\mathfrak{P}(m_1 | -\alpha, m_{\max}) + \lambda\lambda_1 G(m_1|\mu_{m,1}, \sigma_{m,1}) + \lambda(1 - \lambda_1)G(m_1|\mu_{m,2}, \sigma_{m,2})]S(m_1|m_{\min}, \delta_m). \end{aligned} \quad (\text{B9})$$

Here the parameters λ and λ_1 correspond to the fraction of binaries in any Gaussian component and in the lower-mass Gaussian of the Gaussian components, respectively. The distribution $G(m_1|\mu_{m,1}, \sigma_{m,1})$ is a normalized Gaussian distribution for the lower-mass peak with mean $\mu_{m,1}$ and width $\sigma_{m,1}$, and $G(m_1|\mu_{m,2}, \sigma_{m,1})$ is a normalized Gaussian distribution for the upper-mass peak with mean $\mu_{m,2}$ and width $\sigma_{m,2}$. The

hyperparameters for this model are summarized in Table 8. In Figure 18, we provide a corner plot for MULTYPEAK for parameters

corresponding to the two Gaussian peaks. The mean of the upper-mass peak $\mu_{m,2} = 68_{-14}^{+18} M_{\odot}$ is located at approximately twice the mean of the lower-mass peak $\mu_{m,1} = 33.4_{-4.4}^{+4.4} M_{\odot}$. The remaining parameters are $\alpha = 2.9_{-1.4}^{+1.9}$, $\beta_q = 0.9_{-1.3}^{+1.9}$, $m_{\min} = 4.6_{-1.8}^{+1.3} M_{\odot}$, and $m_{\max} = 65_{-30}^{+31} M_{\odot}$. In Figure 19, we provide a posterior predictive check for all of the mass models used in this analysis.

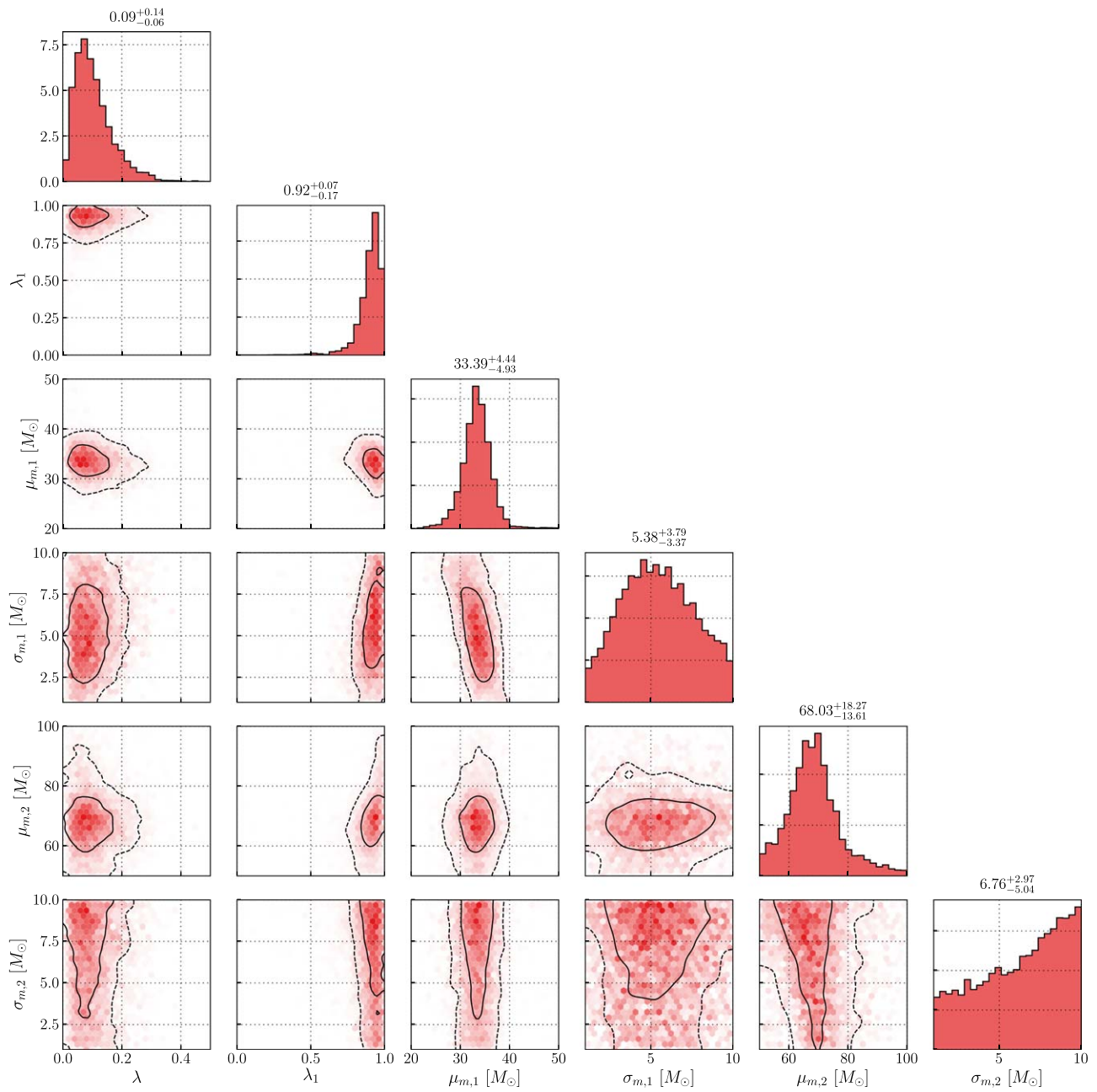


Figure 18. Posterior distribution for mass hyperparameters for MULTIPLEAK. The fit excludes GW190814. The contours represent 50% and 90% credible bounds.

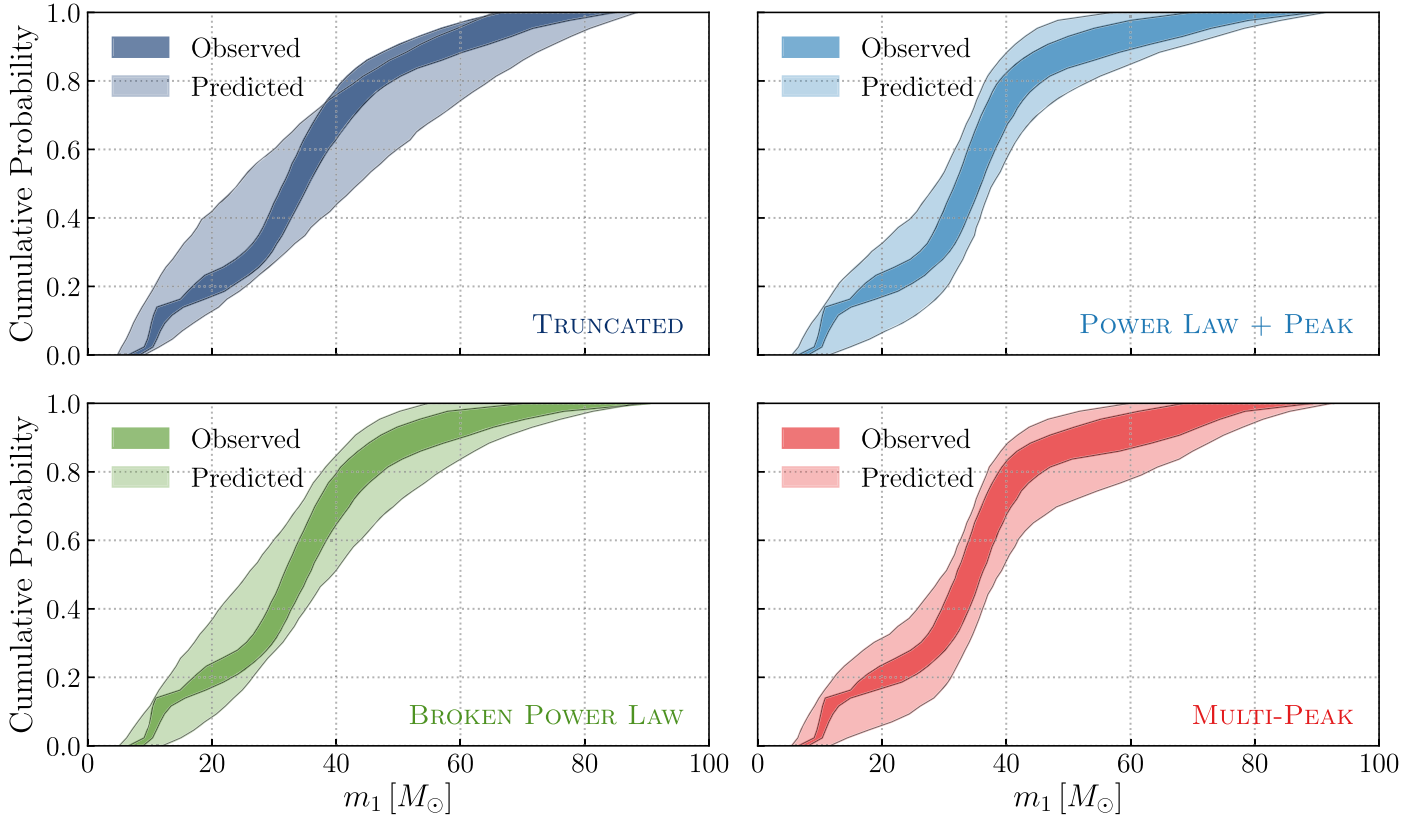


Figure 19. Posterior predictive check: the cumulative density function of the observed primary mass distribution for the TRUNCATED, POWER LAW + PEAK, BROKEN POWER-LAW, and MULTYPEAK models. The observed event distribution is shown with darker colors. The thickness of the bands indicates the 90% credibility range. The POWER LAW + PEAK, BROKEN POWER-LAW, and MULTYPEAK models are a better fit than the TRUNCATED MODEL; the dark band overlaps entirely with the light band. This is due to the POWER LAW + PEAK, BROKEN POWER-LAW, and MULTYPEAK models having more flexibility to fit the relative excess of binaries in the 30–40 M_\odot region compared to the $\gtrsim 40 M_\odot$ region. This analysis excludes GW190814.

Appendix C Mass Model Checking

Section 5.1 describes the inferred mass distribution obtained with the TRUNCATED, BROKEN POWER-LAW, POWER LAW + PEAK, and MULTYPEAK models and compares the different models by calculating their Bayes factors. Here we assess the goodness of fit of the models using posterior predictive checks, comparing predicted and empirical catalogs of observed m_1 distributions in Figure 19. The lighter bands show the cumulative distribution of m_1 as predicted by the model, while the darker bands show the empirical distribution based on the actual events observed in GWTC-2. The bands represent a family of curves, where each curve corresponds to a different draw from the population hyperposterior. Each draw from the hyperposterior updates both the predicted distribution (in the lighter color) and the empirical distribution (in the darker color), as the individual event posteriors are updated according to the inferred population distribution (Galadage et al. 2020; Fishbach et al. 2020b; Miller et al. 2020). If the model is a good fit to the data, the darker bands should overlap with the lighter bands. Figure 19 shows the relatively poor fit for the TRUNCATED MODEL, which cannot capture the excess of events at $\sim 30\text{--}40 M_\odot$ compared to $\gtrsim 40 M_\odot$. The remaining panels show the improved fits with the POWER LAW + PEAK, BROKEN POWER-LAW, and MULTYPEAK models. These results are consistent with the Bayes factors in Table 2, which conclude that the TRUNCATED MODEL is disfavored by a Bayes factor of 10–80 relative to the other models.

C.1. On GW190412

Other than GW190814, we find that GW190412 (Abbott et al. 2020a), when analyzed with a population-informed prior, remains the only system for which we can confidently bound the mass ratio away from unity, yielding $q < 0.53$ at 99% credibility (using the POWER LAW + PEAK mass model). All other events, when analyzed with a population-informed prior, are consistent with $q = 1$ at 99% credibility. Repeating the analysis in Abbott et al. (2020a), we perform a leave-one-out analysis without GW190412 and find $\beta_q = 4.0^{+6.4}_{-3.2}$ ($\beta_q = 4.5^{+5.9}_{-3.5}$) for the POWER LAW + PEAK (BROKEN POWER-LAW) model. The β_q posterior inferred with the inclusion of GW190412 ($\beta_q = 1.3^{+2.4}_{-1.5}$ for the POWER LAW + PEAK model; $\beta_q = 1.4^{+2.5}_{-1.5}$ for the BROKEN POWER-LAW model) has a moderate ($\sim 50\%$) overlap with the leave-one-out β_q posterior, indicating that, consistent with the conclusion in Abbott et al. (2020a), GW190412 likely belongs to the low mass ratio tail of the distribution rather than a distinct subpopulation of asymmetric systems.

C.2. On GW190521

As discussed in Section 5.1, the most massive event, GW190521 (Abbott et al. 2020e), is an outlier with respect to the TRUNCATED MODEL (see Figure 2) but fits well within the mass distributions inferred from the other models. In Figure 20, we show the effect of GW190521 on the primary mass distribution. This event shifts the best-fit mass distribution, but this shift is within the statistical uncertainties. Thus, we find no evidence that GW190521 is an outlier within the framework of the POWER LAW

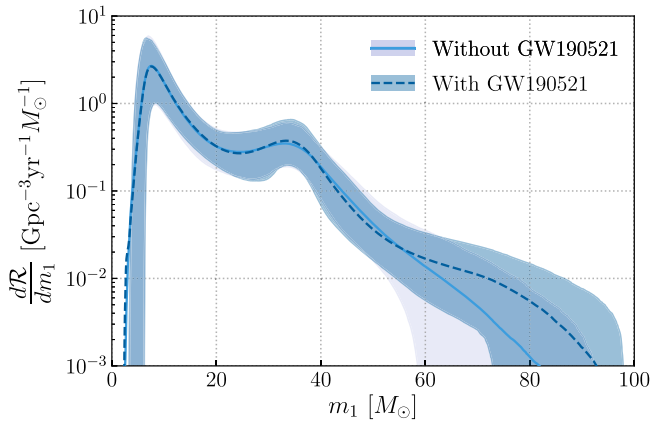


Figure 20. Comparison of the primary BH mass distribution for the population with and without GW190521. The data are fit using the POWER LAW + PEAK model; the BROKEN POWER-LAW model produces similar results. The solid curves are the posterior predictive distributions, while the shaded regions show the 90% credible interval. The inclusion/exclusion of GW190521 does not have a significant effect on the fit. This analysis excludes GW190814.

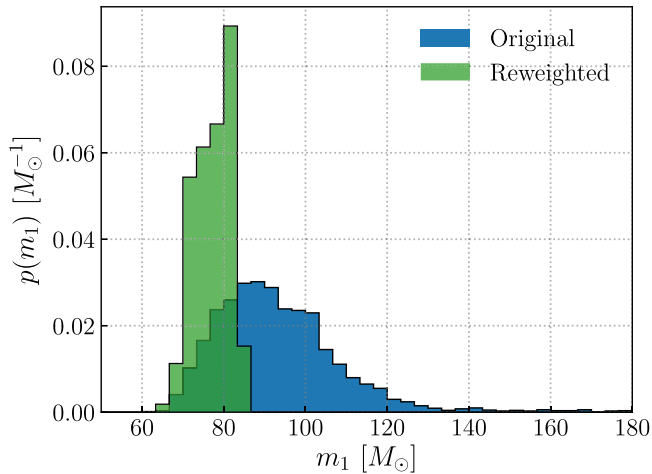


Figure 21. Posterior probability density for the primary mass of GW190521 using the original default prior (blue; flat in redshifted masses) and a reweighted version (green) obtained by using the POWER LAW + PEAK mass model. Results using the BROKEN POWER-LAW mass model are similar. The reweighted version shifts the posterior support to lower masses, with $m_1 < 83 M_\odot$ (99% credibility).

+ PEAK and BROKEN POWER-LAW mass models. This finding is supported by the posterior predictive check in Section C.4. In Figure 21, we show how the primary mass posterior distribution for GW190521 changes when we use the POWER LAW + PEAK model to inform our prior. While the population-informed posterior on the primary mass prefers smaller masses (Fishbach et al. 2020b), the conclusion that the primary mass of GW190521 is above $67 M_\odot$ (99% credibility) is robust to the choice of prior, consistent with the claims in Abbott et al. (2020e).

C.3. On GW190814

On the other hand, we see a clear indication that GW190814 is an outlier with respect to the BBH population within the framework of the POWER LAW + PEAK and BROKEN POWER-LAW mass models, as discussed in Section 5.1. As an additional posterior predictive check, following the analysis described in Fishbach et al. (2020b) and Abbott et al. (2020a), we use the posterior predictive distribution, inferred without

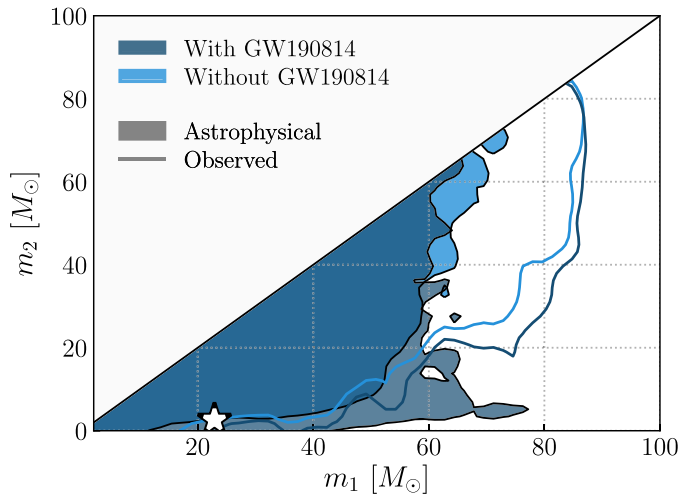
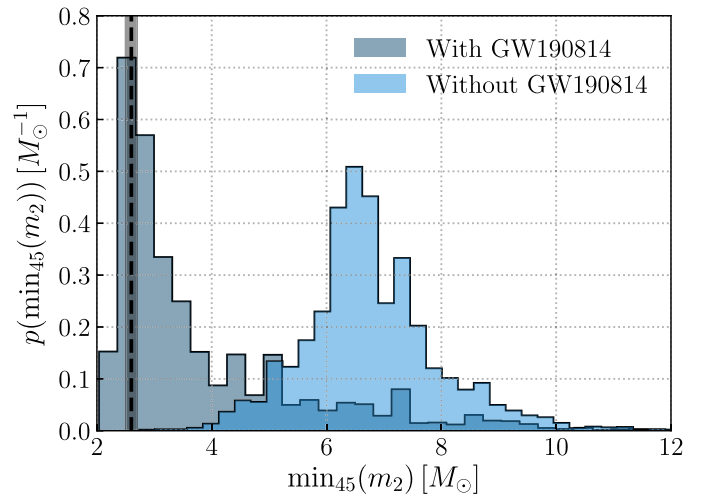
GW190814, to construct a distribution for the minimum m_2 detected in a sample of 45 events. When using both the POWER LAW + PEAK and BROKEN POWER-LAW models, we find that the observation of a system with a secondary mass equal to or smaller than the that of GW190814 ($2.59^{+0.08}_{-0.09} M_\odot$) is highly improbable, with a probability of $<0.02\%$ for both the POWER LAW + PEAK and BROKEN POWER-LAW models; see Figure 22(b) for the distribution of the minimum observed secondary mass in a sample of 45 events predicted by the POWER LAW + PEAK model. The distribution for the BROKEN POWER LAW is qualitatively similar. The mass ratio of GW190814 is also somewhat unusual according to this posterior predictive check; see Figure 22(a). Observing an event with the mass ratio of GW190814 or smaller based on the fit to the other 44 BBH events has a probability of $<0.02\%$ in both the POWER LAW + PEAK and BROKEN POWER-LAW models. These posterior predictive checks suggest that GW190814 is not a typical BBH and support the conclusion that there may be a dearth of systems between ~ 2.6 and $\sim 6 M_\odot$. Future observations will reveal the precise shape of the mass distribution at low masses and extreme mass ratios and better determine the nature of GW190814.

C.4. Mass and Distance Checks with a Burst Analysis

The earlier posterior predictive checks in this section compared simulated sets of BBH masses to the observed set of catalog events. As a complimentary posterior predictive check, we can simulate the gravitational-wave signals from these predicted events, run them through our search pipelines, and compare the synthetic data, as detected by the pipeline, to the observed data. As a proof of principle, we carry out this posterior predictive check with the COHERENT WAVEBURST (CWB) pipeline (Klimenko & Mitselmakher 2004; Klimenko et al. 2016), which is designed to detect unmodeled gravitational-wave transients.

The CWB analysis resulted in the detection of 22 BBH events in GWTC-2. We investigate whether the set of CWB observations is consistent with the model predictions. We focus on assessing possible outliers at high masses and redshifts, where CWB is especially sensitive to BBH signals. In particular, we examine whether GW190521, which was recovered with higher significance by the CWB search than the template searches, is an outlier in the context of our mass and redshift models. Following Klimenko et al. (2016), we calculate the expected distribution of the central frequency f (which depends on the redshifted mass of the BBH) and coherent signal-to-noise ratio ρ (which, for a given redshifted mass, depends on the distance of the BBH) for two different population models, POWER LAW + PEAK and BROKEN POWER LAW, using the NONEVOLVING redshift model. We then compare the empirical distribution of (f, ρ) as recovered by the CWB pipeline to the distribution predicted by the population model. We quantify the comparison by calculating a p -value for each event i , which measures how unusual its observed (f_i, ρ_i) is, given the distribution of predicted (f, ρ) . The central frequency is a proxy for the redshifted mass, while the signal-to-noise ratio is a proxy for the distance.

To compute the predicted distribution of (f, ρ) , we inject simulated waveforms drawn from the POWER LAW + PEAK and BROKEN POWER-LAW distributions into the O1, O2, and O3a data and compile injections recovered by CWB with an $\text{FAR} < 1 \text{ yr}^{-1}$. The central frequencies and coherent signal-to-noise ratios of the recovered injections generated according to POWER LAW + PEAK are plotted in Figure 23. The results for


 (a) The model-averaged astrophysical mass distribution $p(m_1, m_2)$.


(b) Observed minimum secondary mass distribution.

Figure 22. Left: posterior population distribution for primary and secondary mass with and without GW190814. Shown here are the 99% credible intervals. Dark blue is with GW190814, and light blue is without. The shaded regions show the astrophysical distribution, while the colored contours show the observed distribution (as it appears in the catalog due to selection effects). The median value of the posterior of GW190814 is marked with a star. Right: distribution of the minimum secondary mass detected out of 45 detections, predicted from the fit to the POWER LAW + PEAK model to the BBH population excluding GW190814 (light blue) and including GW190814 (dark blue). The dashed line and shaded region (gray) denote the median and 90% symmetric credible interval on the secondary mass of GW190814. This distribution is qualitatively similar to the distribution predicted from the fit to the BROKEN POWER-LAW model.

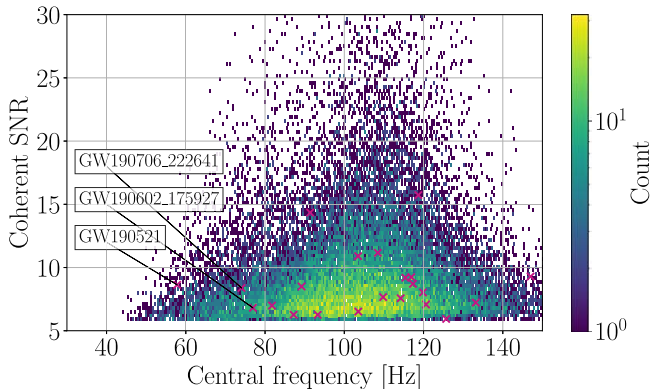


Figure 23. Coherent signal-to-noise ratio and central frequency for 22 BBH events detected by one of our detection pipelines, CWB, in O1, O2, and O3a (violet dots) compared to simulated BBH events from the POWER LAW + PEAK model detected by CWB. The consistency between the distributions of simulated and observed triggers shows that the POWER LAW + PEAK mass model coupled with the NONEVOLVING redshift distribution is a good fit to the data. Results for the BROKEN POWER-LAW model are similar.

a BROKEN POWER LAW are similar. The locations of the 22 detections on this plane are visually consistent with the model predictions, indicating that the model is a reasonably good fit to the data. The event with the lowest p -value (least consistent with predictions) is GW190521, with p -values of 0.053 and 0.077 for the BROKEN POWER-LAW and POWER LAW + PEAK models, respectively. These p -values indicate that GW190521 is a moderately unusual detection, but it is consistent with the population models.

Appendix D Details of Spin Population Models

D.1. DEFAULT Spin Model

This model was introduced in Abbott et al. (2019a). Following Wysocki et al. (2019a), the dimensionless spin

Table 9

Summary of DEFAULT Spin Parameters

Parameter	Description	Prior
μ_χ	Mean of the beta distribution of spin magnitudes	U(0,1)
σ_χ^2	Variance of the beta distribution of spin magnitudes	U(0,0.25)
ζ	Mixing fraction of mergers from TRUNCATED Gaussian distribution	U(0,1)
σ_τ	Width of TRUNCATED Gaussian, determining typical spin misalignment	U(0.01,4)

magnitude distribution is taken to be a beta distribution,

$$\pi(\chi_{1,2} | \alpha_\chi, \beta_\chi) = \text{beta}(\alpha_\chi, \beta_\chi), \quad (\text{D1})$$

where α_χ and β_χ are the standard shape parameters that determine the distribution's mean and variance. The beta distribution is convenient because it is bounded on (0,1). The distributions for χ_1 and χ_2 are assumed to be the same. Following Talbot & Thrane (2017), we define $z = \cos \theta_{1,2}$ as the cosine of the tilt angle between the component spin and a binary's orbital angular momentum and assume that z is distributed as a mixture of two populations:

$$\pi(z | \zeta, \sigma_\tau) = \zeta G_\tau(z | \sigma_\tau) + (1 - \zeta) \mathcal{I}(z). \quad (\text{D2})$$

Here $\mathcal{I}(z)$ is an isotropic distribution, while $G_\tau(z | \sigma_\tau)$ is a TRUNCATED Gaussian peaking at $z = 0$ (perfect alignment) with width σ_τ . The mixing parameter ζ controls the relative fraction of mergers drawn from the isotropic distribution and Gaussian subpopulations. The isotropic subpopulation is intended to accommodate dynamically assembled binaries, while G_τ is a model for field mergers. The hyperparameters for this model and their priors are summarized in Table 9.

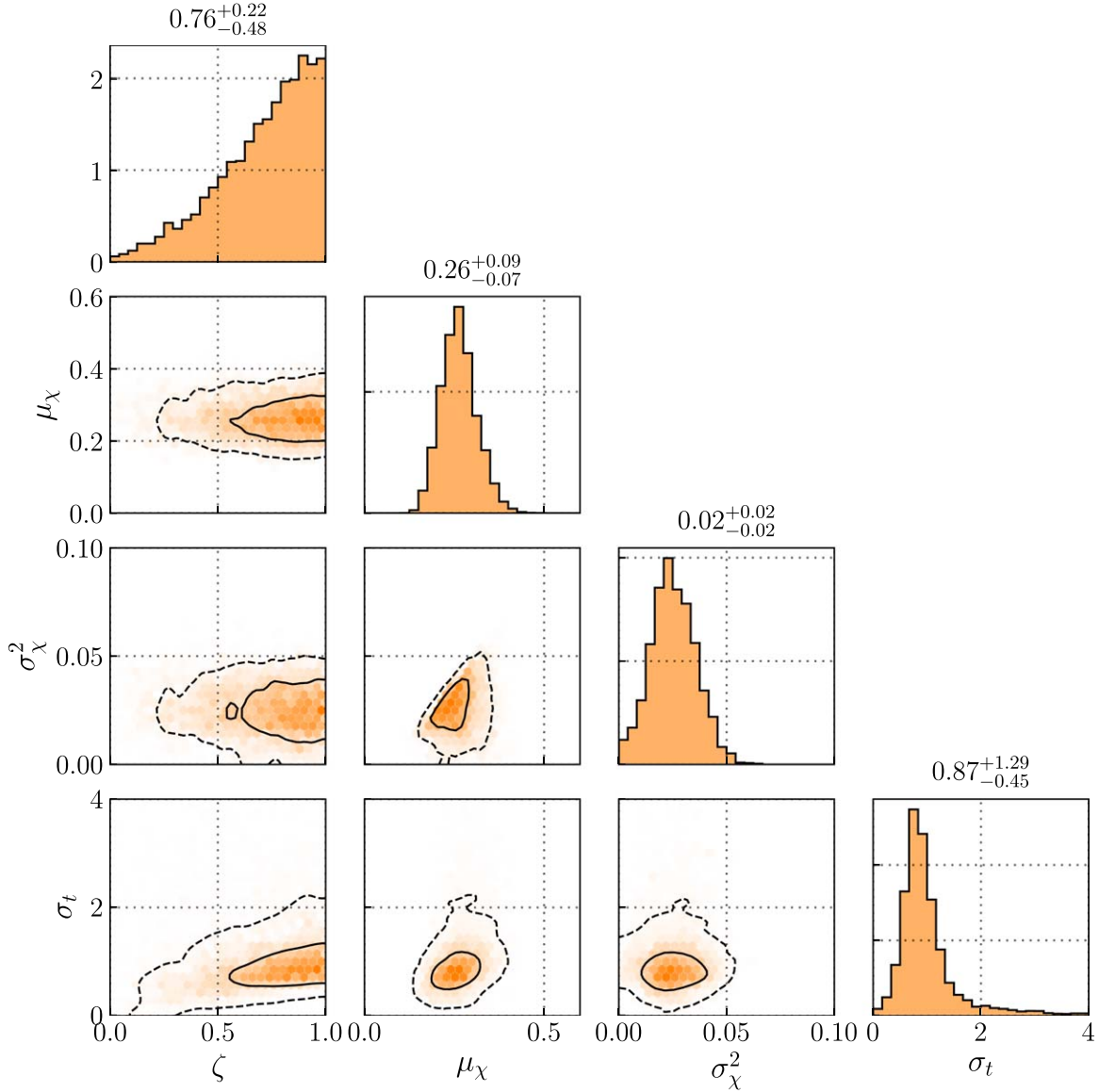


Figure 24. Posterior distribution for spin hyperparameters for DEFAULT, assuming the POWER LAW + PEAK mass model and NONEVOLVING redshift distribution. The fit excludes GW190814. The contours represent 50% and 90% credible bounds. A perfectly aligned spin distribution ($\sigma_t = 0, \zeta = 1$) is ruled out at >99% credibility, consistent with the results of the GAUSSIAN model, but the data disfavor a purely isotropic distribution ($\zeta = 0$ or $\sigma_t \gtrsim 2$).

Additional constraints to the priors on μ_χ and σ_χ^2 are applied by setting $\alpha_\chi, \beta_\chi > 1$.

In Figure 24, we provide a corner plot for the DEFAULT spin model. This model prefers modest spin magnitudes. It favors the hypothesis that binaries are preferentially aligned ($\zeta \rightarrow 1$ and $\sigma_t \lesssim 2$), albeit with potentially large misalignment angles ($\sigma_t > 0$). The case of perfect alignment, which would correspond to $\zeta = 1$ and $\sigma = 0$, is disfavored, lying outside the 99% credible bound on ζ and σ_t . Within the main text, Figure 10 shows the implied distributions of component spin magnitudes and tilt angles. The implied distributions of the effective precession spin parameter (χ_p) and inspiral spin parameter (χ_{eff}) are shown in Figures 9 and 11, respectively; these distributions are in good agreement with the results obtained using the GAUSSIAN model described below. In particular, both models predict the existence of systems with antialigned spins (negative χ_{eff}) and in-plane spin components (nonzero χ_p).

D.2. GAUSSIAN Spin Model

The GAUSSIAN spin model offers an alternative description of BBH spins. It is convenient to measure the distribution of the effective inspiral spin parameter (χ_{eff}) and precession spin parameter (χ_p), which are better constrained than individual component spin magnitudes or tilts. We parameterize the distributions of χ_{eff} and χ_p using a bivariate Gaussian:

$$\pi(\chi_{\text{eff}}, \chi_p | \mu_{\text{eff}}, \sigma_{\text{eff}}, \mu_p, \sigma_p, \rho) \propto G(\chi_{\text{eff}}, \chi_p | \boldsymbol{\mu}, \boldsymbol{\Sigma}). \quad (\text{D3})$$

The distribution has a mean $\boldsymbol{\mu} = (\mu_{\text{eff}}, \mu_p)$ and a covariance matrix

$$\boldsymbol{\Sigma} = \begin{pmatrix} \sigma_{\text{eff}}^2 & \rho \sigma_{\text{eff}} \sigma_p \\ \rho \sigma_{\text{eff}} \sigma_p & \sigma_p^2 \end{pmatrix}. \quad (\text{D4})$$

The population parameters appearing in Equations (D3) and (D4) and their associated priors are summarized in Table 10. We

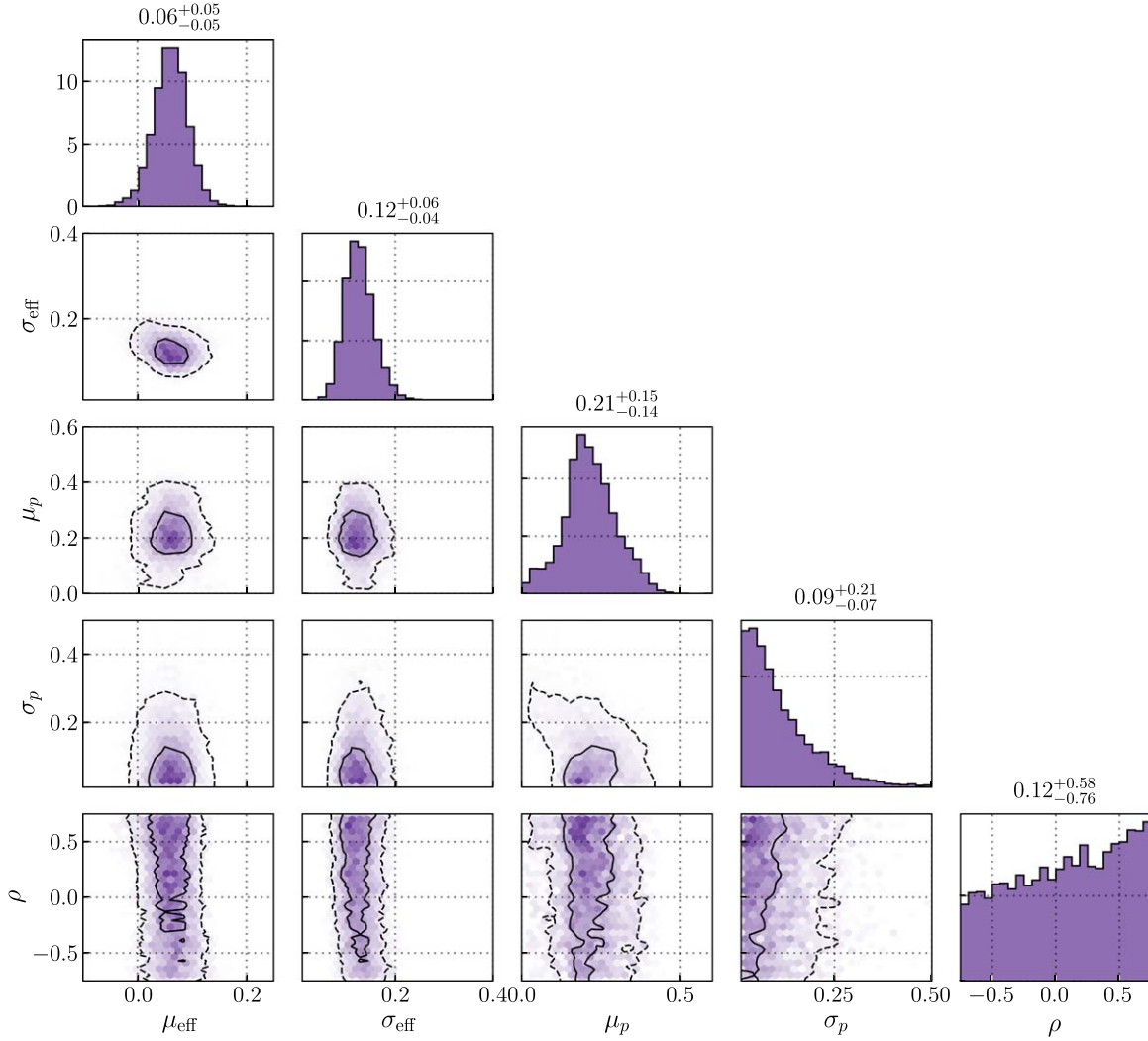


Figure 25. Posterior distribution for spin hyperparameters under the GAUSSIAN model. The fit again excludes GW190814, and contours represent 50% and 90% credible bounds. Consistent with the results of the DEFAULT model, which results in a perfectly aligned spin distribution at 99% credibility, here we find that a vanishing χ_p distribution ($\mu_p = \sigma_p = 0$) is disfavored.

Table 10
Summary of GAUSSIAN Spin Parameters

Parameter	Description	Prior
μ_{eff}	Mean of the χ_{eff} distribution	$U(-1, 1)$
σ_{eff}	Standard deviation of the χ_{eff} distribution	$U(0.01, 1)$
μ_p	Mean of the χ_p distribution	$U(0.01, 1)$
σ_p	Standard deviation of the χ_p distribution	$U(0.01, 1)$
ρ	Degree of correlation between χ_{eff} and χ_p	$U(-0.75, 0.75)$

truncate and normalize Equation (D3) based on the allowed regions of the effective inspiral spin parameter: $\chi_{\text{eff}} \in (-1, 1)$ and $\chi_p \in (0, 1)$. The results from the GAUSSIAN model are obtained assuming a TRUNCATED mass model with $\alpha = -2.2$, $\beta_q = 1.3$, $m_{\text{min}} = 5 M_{\odot}$, and $m_{\text{max}} = 75 M_{\odot}$, consistent with the median values obtained when fitting the TRUNCATED MODEL to GWTC-2. We additionally assume a comoving merger rate density that grows as $(1 + z)^{2.7}$. Although the TRUNCATED MODEL is

disfavored relative to the more complex mass models discussed above, it is sufficient for purposes of constructing an informed mass ratio distribution, the primary confounding factor in efforts to measure χ_{eff} and χ_p (Ng et al. 2018a).

The full posterior on the parameters of the GAUSSIAN model is shown in Figure 25. We find no correlation between the parameters of the χ_{eff} and χ_p distributions, nor do we obtain any information regarding the degree of correlation ρ between the effective inspiral spin parameter and the effective precession spin parameter. As discussed in Section 5.2, analysis with the GAUSSIAN spin model is consistent with the identification of spin-orbit misalignment using the DEFAULT spin model with $\mu_p = \sigma_p = 0$ disfavored. For the DEFAULT spin model, we verified that the signature of spin-orbit misalignment was not a spurious prior artifact, finding that our posterior lies safely outside the artificial exclusion region in Figure 9. A similar exclusion region also exists for the GAUSSIAN model around $\mu_p = \sigma_p = 0$, but our estimate of its exact size is subject to sampling uncertainties driven by the relatively small number of prior samples close to $\chi_p = 0$ for each event.

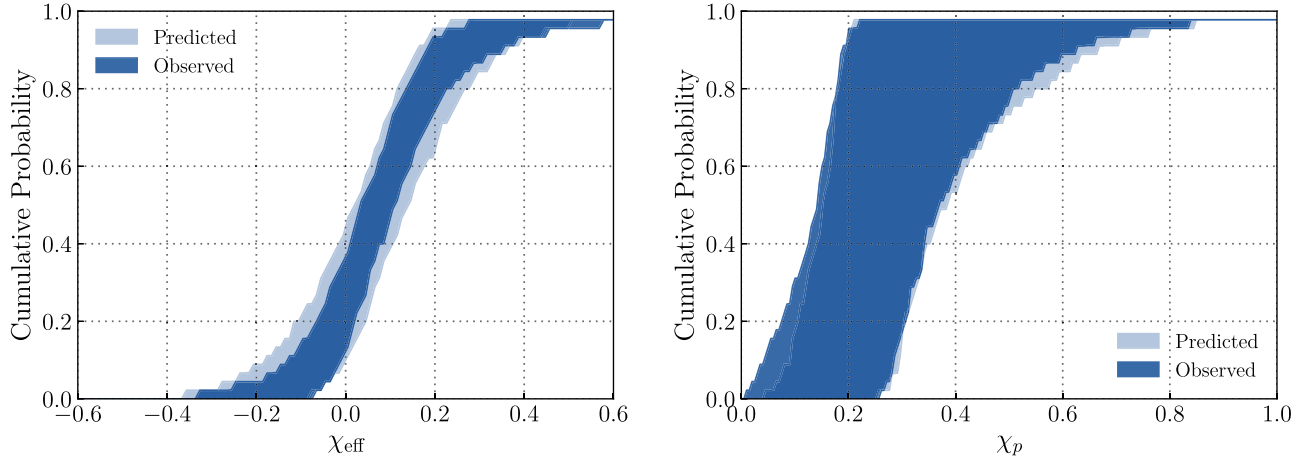


Figure 26. Population predictive checks for the effective inspiral spin parameter χ_{eff} (left) and the effective precession spin parameter χ_p (right) of BBH mergers using the GAUSSIAN spin model. The light blue regions show the central 90% credible bounds on the posterior predictive distributions. According to the model, we expect the observed distributions on χ_{eff} and χ_p to lie within the light blue regions 90% of the time. The dark blue regions show the 90% credible bounds on the observed distributions in GWTC-2, found using the population-informed posteriors of the confident BBH events in GWTC-2. The overlap between the dark and light blue regions shows that the model passes the posterior predictive check. The results for the DEFAULT model are similar, indicating that both models are a good fit to the data.

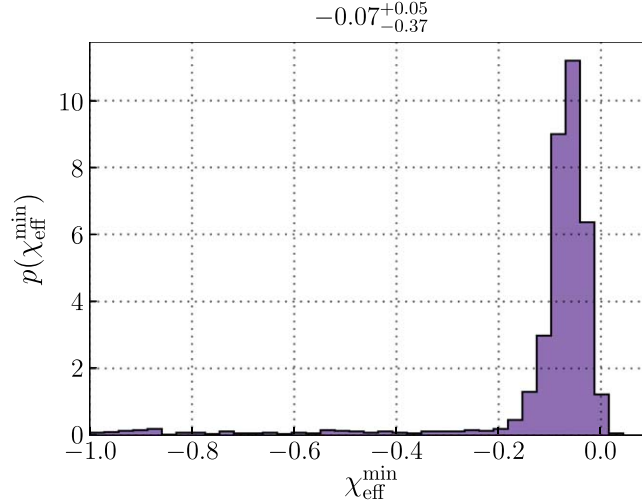


Figure 27. Posterior distribution for $\chi_{\text{eff}}^{\text{min}}$, below which we truncate the GAUSSIAN χ_{eff} distribution. While the results shown in the main text presume $\chi_{\text{eff}}^{\text{min}} = -1$, in Section D.2, we elevate $\chi_{\text{eff}}^{\text{min}}$ to a free hyperparameter to be determined by the data; the resulting marginalized posterior distribution is shown here. In this case, we exclude $\chi_{\text{eff}}^{\text{min}} \geq 0$ at 99% credibility. This finding affirms that the signatures of antialigned BH spins are present in our BBH catalog and not a bias due to our choice of parameterized spin model.

With the GAUSSIAN model, we also find evidence that at least some BHs have antialigned spins, with $\theta > 90^\circ$, such that $\chi_{\text{eff}} < 0$. To further evaluate the robustness of our GAUSSIAN model fits, in Figure 26, we show posterior predictive comparisons between predicted and empirical catalogs of χ_{eff} and χ_p measurements. The light blue regions mark 90% credible bounds on the predicted cumulative distribution of observed effective inspiral spin parameter values, given our posterior on the GAUSSIAN model parameters. The dark blue regions, meanwhile, show 90% credible bounds on the true distribution observed within GWTC-2, achieved by reweighting single-event χ_{eff} and χ_p by repeated random draws from the GAUSSIAN hyperposterior. A similar predictive comparison between the observation and an alternative strictly positive model, in which the effective inspiral spin distribution is TRUNCATED on the interval $0 \leq \chi_{\text{eff}} \leq 1$, reveals possible

tension; when asserting that all effective inspiral spins are positive, the resulting population model underpredicts the number of observations with $\chi_{\text{eff}} < 0.1$ approximately 75% of the time.

As an additional check, we repeat the GAUSSIAN spin analysis on our data, truncating the χ_{eff} distribution not on $(-1, 1)$ but rather on $(\chi_{\text{eff}}^{\text{min}}, 1)$, where $\chi_{\text{eff}}^{\text{min}}$ is inferred from the data. Figure 27 shows the marginal posterior for $\chi_{\text{eff}}^{\text{min}}$. We find that $\chi_{\text{eff}}^{\text{min}}$ is constrained to be negative at 99% credibility, confirming that support for a negative effective inspiral spin parameter is a feature of the data and not simply an artifact of the GAUSSIAN model. In contrast, when we repeat the measurement of $\chi_{\text{eff}}^{\text{min}}$ using simulated catalogs drawn from (i) a Gaussian population TRUNCATED to strictly positive values and (ii) a pair of delta functions at $\chi_{\text{eff}} = 0$ and 0.1, we correctly observe consistency with $\chi_{\text{eff}}^{\text{min}} = 0$. Examining $\chi_{\text{eff}}^{\text{min}}$

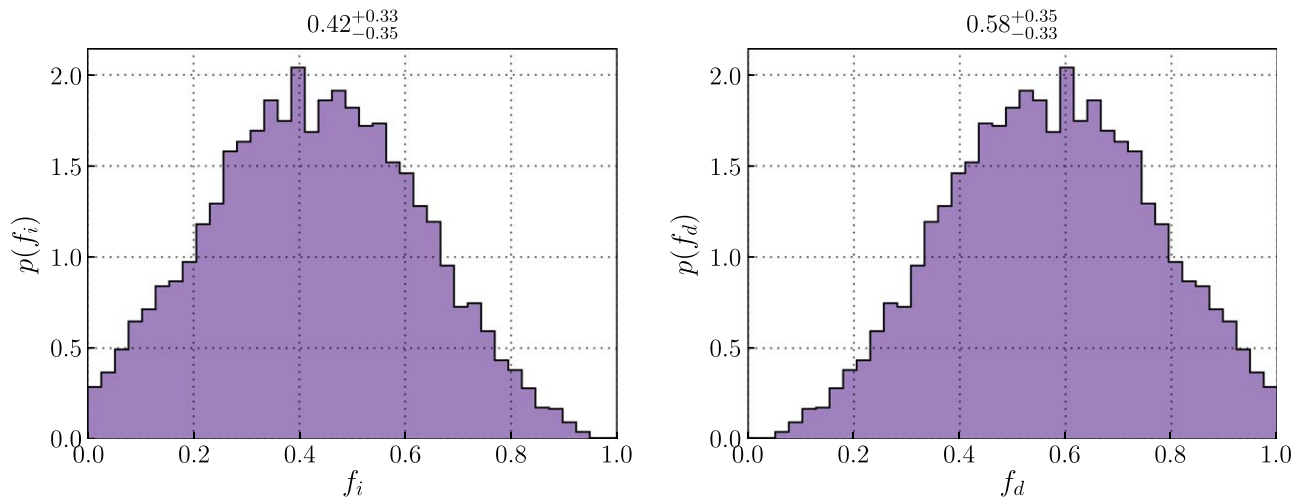


Figure 28. Posterior distributions for f_i (left) and f_d (right) of BBH mergers as defined in Equation (7). Assuming that all binaries with $\chi_{\text{eff}} < 0$ are dynamically formed, f_d corresponds to the fraction of dynamically assembled BBH systems, and f_i corresponds to the fraction of BBH systems formed through the isolated channel.

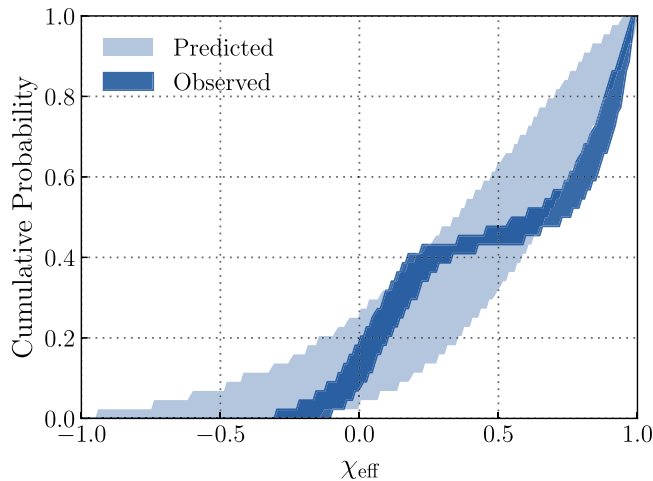


Figure 29. Example of a failed posterior predictive check for the effective inspiral spin parameter χ_{eff} distribution. We fit the GAUSSIAN spin model to a mock catalog drawn from the strongly bimodal χ_{eff} distributions predicted in the presence of tidal torques (Kushnir et al. 2016; Zaldarriaga et al. 2018; Bavera et al. 2019; Belczynski et al. 2020). The dark shaded region shows the central 90% credible bounds on the mock observed cumulative χ_{eff} distribution, while the light region corresponds to that predicted by the model. In this case, our GAUSSIAN model is an extremely poor representation of the underlying χ_{eff} distribution, so significant tension is seen between the observed and predicted distributions, with the model overpredicting the fraction of observations with $\chi_{\text{eff}} < 0$, as well as the fraction of observations with $0.3 \lesssim \chi_{\text{eff}} \lesssim 0.8$.

is therefore a useful safeguard even when the true population is poorly fit by a Gaussian. As described in the main text, we can leverage the assumption that BBHs with negative values of χ_{eff} are formed dynamically to infer the fraction of binaries formed via dynamical (f_d) and isolated (f_i) channels; see Equation (7). In Figure 28, we show the corresponding posterior distributions for f_i and f_d .

There are several sources of possible bias that might influence our GAUSSIAN model conclusions. One possible source of bias is the mass model presumed for the GAUSSIAN spin analysis. As noted above, measurements of a binary’s χ_{eff} and mass ratio q are generally anticorrelated (Ng et al. 2018a). Therefore, our particular choice of $\beta_q = 1.3$ could conceivably affect conclusions regarding the χ_{eff} distribution. We have directly verified that the results in Figure 27 remain robust under different fiducial choices of β_q between -1.5 and 2 .

Another source of bias may be the Gaussian functional form we impose on the χ_{eff} and χ_p distributions, enforcing a unimodal distribution with smooth tails. As discussed in Section 5.2, though, the DEFAULT spin model yields near-identical χ_{eff} and χ_p

distributions, despite its different parameterization and physical assumptions. However, if the χ_{eff} distribution deviates too strongly from a Gaussian functional form, then it may remain possible to spuriously conclude that $\chi_{\text{eff}}^{\text{min}} < 0$. In the case of significant tidal torques, for example, it is predicted that the χ_{eff} distribution is strongly bimodal, with effective inspiral spins clustered near $\chi_{\text{eff}} = 0$ or 1 , with no support at $\chi_{\text{eff}} < 0$ (Kushnir et al. 2016; Zaldarriaga et al. 2018; Bavera et al. 2019; Belczynski et al. 2020). To illustrate how the results can be biased from model misspecification, we analyze mock observations drawn from a similar bimodal distribution. Using this intentionally misspecified model, we incorrectly conclude that $\chi_{\text{eff}}^{\text{min}} < 0$. However, in cases of such extreme model mismatch, we expect that our data would fail the predictive check of Figure 26. Indeed, Figure 29 shows the result of such a predictive check in the case of the bimodal, tidally torqued χ_{eff} distribution. When fitting this population with a Gaussian model, we find that the model overpredicts the fraction of mock observations with negative χ_{eff} , as well as the range $0.3 \lesssim \chi_{\text{eff}} \lesssim 0.8$, showing a clear deviation in the predicted and observed cumulative χ_{eff} distributions.

Table 11
Summary of MULTISPIN Parameters

Parameter	Description	Prior
\mathcal{R}_{pl}	Local merger rate for the low-mass power-law subpopulation	U(0, 5000)
\mathcal{R}_{g}	Local merger rate for the high-mass Gaussian subpopulation	U(0, 5000)
α_m	Power-law slope of the primary mass distribution for the low-mass subpopulation	U(-4, 12)
β_q	Power-law slope of the mass ratio distribution for the low-mass subpopulation	U(-4, 10)
m_{min}	Minimum mass of the primary mass distribution for the low-mass subpopulation	U(2, 10)
m_{max}	Maximum mass of the primary mass distribution for the low-mass subpopulation	U(30, 100)
μ_{m_1}	Centroid of the primary mass distribution for the high-mass subpopulation	U(20, 50)
σ_{m_1}	Width of the primary mass distribution for the high-mass subpopulation	U(0.4, 10)
μ_{m_2}	Centroid of the secondary mass distribution for the high-mass subpopulation	U(20, 50)
σ_{m_2}	Width of the secondary mass distribution for the high-mass subpopulation	U(0.4, 10)
Mean $\chi_{1,\text{pl}}$	Mean of the beta distribution of primary spin magnitudes for the low-mass subpopulation	U(0, 1)
Var $\chi_{1,\text{pl}}$	Variance of the beta distribution of primary spin magnitudes for the low-mass subpopulation	U(0, 0.25)
$\sigma_{1,\text{pl}}$	Width of the TRUNCATED Gaussian distribution of the cosine of the primary spin-tilt angle for the low-mass subpopulation	U(0, 4)
Mean $\chi_{2,\text{pl}}$	Mean of the beta distribution of secondary spin magnitudes for the low-mass subpopulation	U(0, 1)
Var $\chi_{2,\text{pl}}$	Variance of the beta distribution of secondary spin magnitudes for the low-mass subpopulation	U(0, 0.25)
$\sigma_{2,\text{pl}}$	Width of the TRUNCATED Gaussian distribution of cos(secondary spin-tilt angle) for the low-mass subpopulation	U(0, 4)
Mean $\chi_{1,\text{g}}$	Mean of the beta distribution of primary spin magnitudes for the high-mass subpopulation	U(0, 1)
Var $\chi_{1,\text{g}}$	Variance of the beta distribution of primary spin magnitudes for the high-mass subpopulation	U(0, 0.25)
$\sigma_{1,\text{g}}$	Width of the TRUNCATED Gaussian distribution of cos(primary spin-tilt angle) for the high-mass subpopulation	U(0, 4)
Mean $\chi_{2,\text{g}}$	Mean of the beta distribution of secondary spin magnitudes for the high-mass subpopulation	U(0, 1)
Var $\chi_{2,\text{g}}$	Variance of the beta distribution of secondary spin magnitudes for the high-mass subpopulation	U(0, 0.25)
$\sigma_{2,\text{g}}$	Width of the TRUNCATED Gaussian distribution of cos(secondary spin-tilt angle) for the high-mass subpopulation	U(0, 4)

D.3. MULTISPIN Model

This model is an extension of the TRUNCATED mass model with an additional Gaussian component. It is similar to the POWER LAW + PEAK model, but there are several differences. First, the high-mass subpopulation in the MULTISPIN model is described by a Gaussian in both m_1 and m_2 (up to the $m_1 \geq m_2$ truncation), while POWER LAW + PEAK only models m_1 as a Gaussian and assumes that all BBH systems are described by a power-law distribution in mass ratio q . Most importantly, as its name suggests, the MULTISPIN model allows each subpopulation to have its own independent spin distribution, each of which follows the DEFAULT model, with $\zeta = 1$. This allows us to probe whether the spin distribution varies with mass. The parameters for MULTISPIN are summarized in Table 11.

Appendix E

Redshift Evolution Models

The POWER-LAW redshift evolution model parameterizes the merger rate density as

$$\mathcal{R}(z) = \mathcal{R}_0(1 + z)^\kappa, \quad (\text{E1})$$

where \mathcal{R}_0 denotes the merger rate density at $z = 0$. This implies that the redshift distribution is

$$\frac{dN}{dz} = \mathcal{C} \frac{dV_c}{dz} (1 + z)^{\kappa-1}, \quad (\text{E2})$$

where dV_c/dz is the differential comoving volume, and \mathcal{C} is related to \mathcal{R}_0 by

$$\mathcal{R}_0 = \mathcal{C} \frac{dV_c}{dz} \left[\int_0^{z_{\text{max}}} \frac{dV_c}{dz} (1 + z)^{\kappa-1} \right]^{-1}. \quad (\text{E3})$$

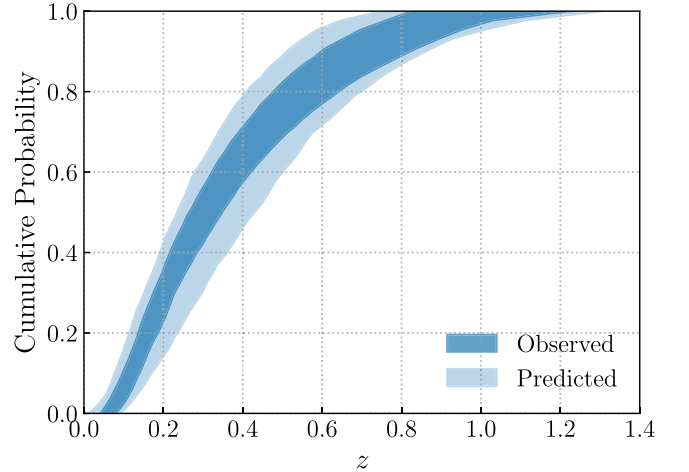


Figure 30. Posterior predictive check: the cumulative density function for the POWER-LAW EVOLUTION model. The model is a good fit to the data. This analysis excludes GW190814.

We take $z_{\text{max}} = 2.3$ in the analysis, as this is a conservative upper bound on the redshift at which we could detect BBH systems during O3a within the mass range considered here. When fitting this model, we employ a uniform prior on κ centered at $\kappa = 0$. The value $\kappa = 0$ corresponds to no evolution, i.e., a merger rate that is uniform in comoving volume and source-frame time. We take a sufficiently wide prior so that the likelihood is entirely within the prior range, $\kappa \in (-6, 6)$. We show a posterior predictive check for this redshift evolution model in Figure 30.

Appendix F

Gravitational-wave Lensing

It has been suggested that gravitational-wave lensing could bias the estimate of binary masses (Dai et al. 2017; Li et al. 2018; Ng et al. 2018b; Oguri 2018; Hannuksela et al. 2019), which could lead to a biased population inference. However, based on the predictions on the number of expected gravitational-wave sources and the distribution of galaxy lenses in the universe, Li et al. (2018) and Oguri (2018) predicted that only around one in a thousand observed events are lensed, although this estimate can vary depending on the redshift evolution of the merger rate density. The lensing rate is expected to be similarly rare for galaxy clusters (Smith et al. 2018). As the expected lensing rate is low compared to the number of events in GWTC-2, we assume that all events in our sample are unlensed.

ORCID iDs

K. Ackley  <https://orcid.org/0000-0002-8648-0767>
 K. Agatsuma  <https://orcid.org/0000-0002-3952-5985>
 S. Anand  <https://orcid.org/0000-0003-3768-7515>
 G. Ashton  <https://orcid.org/0000-0001-7288-2231>
 F. Aubin  <https://orcid.org/0000-0002-8241-4156>
 F. Badaracco  <https://orcid.org/0000-0001-8553-7904>
 S. Banagiri  <https://orcid.org/0000-0001-7852-7484>
 I. Bartos  <https://orcid.org/0000-0001-5607-3637>
 B. Bécsy  <https://orcid.org/0000-0003-0909-5563>
 M. Bejger  <https://orcid.org/0000-0002-4991-8213>
 S. Bernuzzi  <https://orcid.org/0000-0002-2334-0935>
 D. Bhattacharjee  <https://orcid.org/0000-0003-0466-750X>
 I. A. Bilenko  <https://orcid.org/0000-0002-9543-0542>
 M. Boer  <https://orcid.org/0000-0001-9157-4349>
 Y. Bouffanais  <https://orcid.org/0000-0003-3462-0366>
 F. Brighenti  <https://orcid.org/0000-0001-9807-8479>
 R. Buscicchio  <https://orcid.org/0000-0002-7387-6754>
 M. Cabero  <https://orcid.org/0000-0003-4059-4512>
 M. W. Coughlin  <https://orcid.org/0000-0002-8262-2924>
 M. Fishbach  <https://orcid.org/0000-0002-1980-5293>
 D. E. Holz  <https://orcid.org/0000-0002-0175-5064>
 V. Kalogera  <https://orcid.org/0000-0001-9236-5469>
 S. Nissanke  <https://orcid.org/0000-0001-6573-7773>
 G. Raaijmakers  <https://orcid.org/0000-0002-9397-786X>

References

Aasi, J., Abadie, J., Abbott, B. P., et al. 2015, *CQGra*, 32, 074001
 Abbott, B., Abbott, R., Abbott, T., et al. 2013, *LRR*, 21, 3
 Abbott, B., Abbott, R., Abbott, T., et al. 2016a, *PhRvD*, 94, 064035
 Abbott, B., Abbott, R., Abbott, T., et al. 2016b, *PhRvL*, 116, 241103
 Abbott, B., Abbott, R., Abbott, T., et al. 2016c, *PhRvL*, 116, 241102
 Abbott, B., Abbott, R., Abbott, T., et al. 2019a, *ApJL*, 882, L24
 Abbott, B., Abbott, R., Abbott, T., et al. 2019b, *PhRvX*, 9, 031040
 Abbott, B., Abbott, R., Abbott, T., et al. 2021, *SoftX*, 13, 100658
 Abbott, R., Abbott, T., Abraham, S., et al. 2020a, arXiv:2004.08342
 Abbott, R., Abbott, T., Abraham, S., et al. 2020b, *ApJL*, 896, L44
 Abbott, R., Abbott, T., Abraham, S., et al. 2020c, arXiv:2010.14527
 Abbott, R., Abbott, T. D., Abraham, S., et al. 2020d, LIGO Document P2000434-v2, <https://dcc.ligo.org/LIGO-P2000434/public>
 Abbott, R., Abbott, T. D., Abraham, S., et al. 2020e, *PhRvL*, 125, 101102
 Abbott, R., Abbott, T. D., Abraham, S., et al. 2020f, *ApJL*, 900, L13
 Acernese, F., Agathos, M., Agatsuma, K., et al. 2015, *CQGra*, 32, 024001
 Adams, T., Buskulic, D., Germain, V., et al. 2016, *CQGra*, 33, 175012
 Allen, B. 2005, *PhRvD*, 71, 062001
 Allen, B., Anderson, W. G., Brady, P. R., Brown, D. A., & Creighton, J. D. E. 2012, *PhRvD*, 85, 122006
 Antonini, F., & Gieles, M. 2020, arXiv:2009.01861

Antonini, F., Murray, N., & Mikkola, S. 2014, *ApJ*, 781, 45
 Antonini, F., & Rasio, F. A. 2016, *ApJ*, 831, 187
 Antonini, F., Rodríguez, C. L., Petrovich, C., & Fischer, C. L. 2018, *MNRAS Letters*, 480, L58
 Antonini, F., Toonen, S., & Hamers, A. S. 2017, *ApJ*, 841, 77
 Apostolatos, T. A., Cutler, C., Sussman, G. J., & Thorne, K. S. 1994, *PhRvD*, 49, 6274
 Arca Sedda, M. 2020a, *ApJ*, 891, 47
 Arca Sedda, M. 2020b, *CmPhy*, 3, 43
 Arca Sedda, M., Mapelli, M., Spera, M., Benacquista, M., & Giacobbo, N. 2020, *ApJ*, 894, 133
 Ashton, G., Hübner, M., Lasky, P. D., et al. 2019, *ApJS*, 241, 27
 Ashton, G., & Thrane, E. 2020, *MNRAS*, 498, 1905
 Babak, S., Taracchini, A., & Buonanno, A. 2017, *PhRvD*, 95, 024010
 Baibhav, V., Berti, E., Gerosa, D., et al. 2019, *PhRvD*, 100, 064060
 Bailyn, C., Jain, R. K., Coppi, P., & Orosz, J. A. 1998, *ApJ*, 499, 367
 Banerjee, S., Baumgardt, H., & Kroupa, P. 2010, *MNRAS*, 402, 371
 Barkat, Z., Rakavy, G., & Sack, N. 1967, *PhRvL*, 18, 379
 Bartos, I., Kocsis, B., Haiman, Z., & Márka, S. 2017, *ApJ*, 835, 165
 Bavera, S. S., Fragos, T., Qin, Y., et al. 2019, *A&A*, 635, A97
 Belczynski, K., Heger, A., Gladysz, W., et al. 2016, *A&A*, 594, A97
 Belczynski, K., Kalogera, V., & Bulik, T. 2002, *ApJ*, 572, 407
 Belczynski, K., Klencki, J., Fields, C. E., et al. 2020, *A&A*, 636, A104
 Berti, E., & Volonteri, M. 2008, *ApJ*, 684, 822
 Bethe, H. A., & Brown, G. E. 1998, *ApJ*, 506, 780
 Biscoveanu, S., Isi, M., Vitale, S., & Varma, V. 2020, arXiv:2007.09156
 Bohé, A., Hannam, M., Husa, S., et al. 2016, LIGO Document T1500602-v4, <https://dcc.ligo.org/LIGO-T1500602/public>
 Bohé, A., Shao, L., Taracchini, A., et al. 2017, *PhRvD*, 95, 044028
 Calderón Bustillo, J., Laguna, P., & Shoemaker, D. 2017, *PhRvD*, 95, 104038
 Calderón Bustillo, J., Sanchis-Gual, N., Torres-Forné, A., & Font, J. A. 2020, arXiv:2009.01066
 Canton, T. D., Nitz, A. H., Lundgren, A. P., et al. 2014, *PhRvD*, 90, 082004
 Carpenter, B., Gelman, A., Hoffman, M. D., et al. 2017, *Journal of Statistical Software*, 76, 1
 Carr, B., Kühnel, F., & Sandstad, M. 2016, *PhRvD*, 94, 083504
 Carr, B. J., & Hawking, S. W. 1974, *MNRAS*, 168, 399
 Chatziioannou, K., Cotesta, R., Ghonge, S., et al. 2019, *PhRvD*, 100, 104015
 Chu, Q. 2017, PhD thesis, Univ. Western Australia
 Croon, D., McDermott, S. D., & Sakstein, J. 2020, arXiv:2007.07889
 Dai, L., Venumadhav, T., & Sigurdson, K. 2017, *PhRvD*, D95, 044011
 Damour, T. 2001, *PhRvD*, 64, 124013
 de Mink, S. E., & Mandel, I. 2016, *MNRAS*, 460, 3545
 Di Carlo, U. D., Giacobbo, N., Mapelli, M., et al. 2019, *MNRAS*, 487, 2947
 Di Carlo, U. D., Mapelli, M., Bouffanais, Y., et al. 2020, *MNRAS*, 497, 1043
 Doctor, Z., Wysocki, D., O’Shaughnessy, R., Holz, D. E., & Farr, B. 2020, *ApJ*, 893, 35
 Dominik, M., Belczynski, K., Fryer, C., et al. 2013, *ApJ*, 779, 72
 Dominik, M., Berti, E., O’Shaughnessy, R., et al. 2015, *ApJ*, 806, 263
 Downing, J. M. B., Benacquista, M. J., Giersz, M., & Spurzem, R. 2011, *MNRAS*, 416, 133
 Eldridge, J. J., Stanway, E. R., & Tang, P. N. 2019, *MNRAS*, 482, 870
 Eldridge, J. J., Stanway, E. R., Xiao, L., et al. 2017, *PASA*, 34, e058
 Essick, R., & Landry, P. 2020, *ApJ*, 904, 80
 Fairhurst, S., Green, R., Hannam, M., & Hoy, C. 2020, *PhRvD*, 102, 041302
 Farmer, R., Renzo, M., de Mink, S., Fishbach, M., & Justham, S. 2020, *ApJL*, 902, L36
 Farmer, R., Renzo, M., de Mink, S. E., Marchant, P., & Justham, S. 2019, *ApJ*, 887, 53
 Farr, B., Holz, D. E., & Farr, W. M. 2018, *ApJL*, 854, L9
 Farr, W. M. 2019, *RNAAS*, 3, 66
 Farr, W. M., Sravan, N., Cantrell, A., et al. 2011, *ApJ*, 741, 103
 Farr, W. M., Stevenson, S., Coleman Miller, M., et al. 2017, *Natur*, 548, 426
 Farrell, E. J., Groh, J. H., Hirschi, R., et al. 2021, *MNRAS Letters*, 502, L40
 Farrow, N., Zhu, X.-J., & Thrane, E. 2019, *ApJ*, 876, 18
 Fernandez, N., & Profumo, S. 2019, *JCAP*, 2019, 022
 Fishbach, M., Essick, R., & Holz, D. E. 2020a, *ApJL*, 899, L8
 Fishbach, M., Farr, W. M., & Holz, D. E. 2020b, *ApJL*, 891, L31
 Fishbach, M., & Holz, D. E. 2017, *ApJL*, 851, L25
 Fishbach, M., & Holz, D. E. 2020a, *ApJL*, 904, L26
 Fishbach, M., & Holz, D. E. 2020b, *ApJL*, 891, L27
 Fishbach, M., Holz, D. E., & Farr, B. 2017, *ApJL*, 840, L24
 Fishbach, M., Holz, D. E., & Farr, W. M. 2018, *ApJL*, 863, L41
 Foreman-Mackey, D., Hogg, D. W., Lang, D., & Goodman, J. 2013, *PASP*, 125, 306
 Fowler, W. A., & Hoyle, F. 1964, *ApJS*, 9, 201

- Fragione, G., Grishin, E., Leigh, N. W. C., Perets, H. B., & Perna, R. 2019, *MNRAS*, **488**, 47
- Fragione, G., & Kocsis, B. 2018, *PhRvL*, **121**, 161103
- Fragione, G., & Kocsis, B. 2019, *MNRAS*, **486**, 4781
- Fragione, G., & Kocsis, B. 2020, *MNRAS*, **493**, 3920
- Fuller, J., & Ma, L. 2019, *ApJL*, **881**, L1
- Fuller, J., Piro, A. L., & Jermyn, A. S. 2019, *MNRAS*, **485**, 3661
- Galadage, S., Adamcewicz, C., Zhu, X.-J., & Thrane, E. 2021, *ApJL*, **909**, L19
- Galadage, S., Talbot, C., & Thrane, E. 2020, *PhRvD*, **102**, 083026
- Gayathri, V., Healy, J., Lange, J., et al. 2020, arXiv:2009.05461
- Gerosa, D., & Berti, E. 2017, *PhRvD*, **95**, 124046
- Gerosa, D., Berti, E., O'Shaughnessy, R., et al. 2018, *PhRvD*, **98**, 084036
- Giacobbo, N., Mapelli, M., & Spera, M. 2017, *MNRAS*, **474**, 2959
- Gröbner, M., Ishibashi, W., Tiwari, S., Haney, M., & Jetzer, P. 2020, *A&A*, **638**, A119
- Gültekin, K., Miller, M. C., & Hamilton, D. P. 2004, *ApJ*, **616**, 221
- Hanna, C., Caudill, S., Messick, C., et al. 2020, *PhRvD*, **101**, 022003
- Hannam, M., Schmidt, P., Bohé, A., et al. 2014, *PhRvL*, **113**, 151101
- Hannuksela, O. A., Haris, K., Ng, K. K. Y., et al. 2019, *ApJL*, **874**, L2
- Harry, I., Privitera, S., Bohé, A., & Buonanno, A. 2016, *PhRvD*, **94**, 024012
- Heger, A., Fryer, C. L., Woosley, S. E., Langer, N., & Hartmann, D. H. 2003, *ApJ*, **591**, 288
- Heger, A., & Woosley, S. E. 2002, *ApJ*, **567**, 532
- Huang, Y., Haster, C.-J., Vitale, S., et al. 2020, *PhRvD*, **102**, 103024
- Husa, S., Khan, S., Hannam, M., et al. 2016, *PhRvD*, **93**, 044006
- Inayoshi, K., Hirai, R., Kinugawa, T., & Hotokezaka, K. 2017, *MNRAS*, **468**, 5020
- Jeffreys, H. 1961, *Theory of Probability* (3rd ed.; Oxford: Oxford Univ. Press)
- Kalogera, V. 2000, *ApJ*, **541**, 319
- Khan, S., Ohme, F., Chatziioannou, K., & Hannam, M. 2020, *PhRvD*, **101**, 024056
- Khan, S., Husa, S., Hannam, M., et al. 2016, *PhRvD*, **93**, 044007
- Kidder, L. E. 1995, *PhRvD*, **52**, 821
- Kimball, C., Talbot, C., Berry, C. P., et al. 2020a, *ApJ*, **900**, 177
- Kimball, C., Talbot, C., Berry, C. P., et al. 2020b, arXiv:2011.05332
- Kimpson, T. O., Spera, M., Mapelli, M., & Ziosi, B. M. 2016, *MNRAS*, **463**, 2443
- Klimenko, S., & Mitselmakher, G. 2004, *CQGrA*, **21**, S1819
- Klimenko, S., Vedovato, G., Drago, M., et al. 2016, *PhRvD*, **93**, 042004
- Kopparapu, R. K., Hanna, C., Kalogera, V., et al. 2008, *ApJ*, **675**, 1459
- Kovetz, E. D., Cholis, I., Breysse, P. C., & Kamionkowski, M. 2017, *PhRvD*, **95**, 103010
- Kreidberg, L., Bailyn, C. D., Farr, W. M., & Kalogera, V. 2012, *ApJ*, **757**, 36
- Kulkarni, S. R., Hut, P., & McMillan, S. 1993, *Natur*, **364**, 421
- Kushnir, D., Zaldarriaga, M., Kollmeier, J. A., & Waldman, R. 2016, *MNRAS*, **462**, 844
- Lange, J., O'Shaughnessy, R., & Rizzo, M. 2018, arXiv:1805.10457
- Li, S.-S., Mao, S., Zhao, Y., & Lu, Y. 2018, *MNRAS*, **476**, 2220
- LIGO Scientific Collaboration 2018, *LIGO Algorithm Library—LALSuite*, Free Software (GPL), doi:10.7935/GT1W-FZ16
- LIGO-Virgo 2020, *GWTC-2 Data Release: Sensitivity of Matched Filter Searches to Binary Black Hole Merger Populations*, <https://dcc.ligo.org/LIGO-P2000217/public>
- Liu, B., & Bromm, V. 2020, arXiv:2009.11447
- Liu, B., Lai, D., & Wang, Y.-H. 2019, *ApJ*, **881**, 41
- Loredo, T. J. 2004, in *AIP Conf. Ser. 735, Bayesian Inference And Maximum Entropy Methods In Science And Engineering*, ed. V. Dose et al. (Melville, NY: AIP), 195
- Lower, M. E., Thrane, E., Lasky, P. D., & Smith, R. J. E. 2018, *PhRvD*, **98**, 083028
- Madau, P., & Dickinson, M. 2014, *ARA&A*, **52**, 415
- Madau, P., & Rees, M. J. 2001, *ApJL*, **551**, L27
- Magee, R., Fong, H., Caudill, S., et al. 2019, *ApJL*, **878**, L17
- Mandel, I., & de Mink, S. E. 2016, *MNRAS*, **458**, 2634
- Mandel, I., Farr, W. M., & Gair, J. R. 2019, *MNRAS*, **486**, 1086
- Mandel, I., Müller, B., Riley, J., et al. 2021, *MNRAS*, **500**, 1380
- Mandel, I., & O'Shaughnessy, R. 2010, *CQGrA*, **27**, 114007
- Mapelli, M. 2016, *MNRAS*, **459**, 3432
- Mapelli, M., Giacobbo, N., Ripamonti, E., & Spera, M. 2017, *MNRAS*, **472**, 2422
- Mapelli, M., Spera, M., Montanari, E., et al. 2020, *ApJ*, **888**, 76
- Marchant, P., Langer, N., Podsiadlowski, P., Tauris, T. M., & Moriya, T. J. 2016, *A&A*, **588**, A50
- Marchant, P., & Moriya, T. 2020, *A&A*, **640**, L8
- McKernan, B., Ford, K. E. S., Lyra, W., & Perets, H. B. 2012, *MNRAS*, **425**, 460
- McKernan, B., Ford, K. E. S., O'Shaughnessy, R., & Wysocki, D. 2020, *MNRAS*, **494**, 1203
- McKernan, B., Saavik Ford, K. E., Bellovary, J., et al. 2018, *ApJ*, **866**, 66
- Messick, C., Blackburn, K., Brady, P., et al. 2017, *PhRvD*, **95**, 042001
- Miller, C. M., & Hamilton, D. P. 2002a, *ApJ*, **576**, 894
- Miller, M. C., & Hamilton, D. P. 2002b, *MNRAS*, **330**, 232
- Miller, M. C., & Lauburg, V. M. 2009, *ApJ*, **692**, 917
- Miller, S., Callister, T. A., & Farr, W. 2020, *ApJ*, **895**, 128
- Moody, K., & Sigurdsson, S. 2009, *ApJ*, **690**, 1370
- Most, E. R., Papenfort, L. J., Weih, L. R., & Rezzolla, L. 2020, *MNRAS Letters*, **499**, L82
- Natarajan, P. 2021, *MNRAS*, **501**, 1413
- Neijssel, C. J., Vigna-Gómez, A., Stevenson, S., et al. 2019, *MNRAS*, **490**, 3740
- Ng, K. K., Vitale, S., Zimmerman, A., et al. 2018a, *PhRvD*, **98**, 083007
- Ng, K. K. Y., Wong, K. W. K., Broadhurst, T., & Li, T. G. F. 2018b, *PhRvD*, **97**, 023012
- Nitz, A. H., Capano, C., Nielsen, A. B., et al. 2019, *ApJ*, **872**, 195
- Nitz, A. H., & Capano, C. D. 2021, *ApJL*, **907**, L9
- Nitz, A. H., Dent, T., Canton, T. D., Fairhurst, S., & Brown, D. A. 2017, *ApJ*, **849**, 118
- Nitz, A. H., Dent, T., Davies, G. S., et al. 2020a, *ApJ*, **891**, 123
- Nitz, A., Harry, I., Brown, D., et al. 2020b, *gwastro/pycbc: Pycbc release v1.15.0*, Zenodo, doi:10.5281/zenodo.596388
- O'Leary, R. M., Kocsis, B., & Loeb, A. 2009, *MNRAS*, **395**, 2127
- O'Leary, R. M., Rasio, F. A., Fregeau, J. M., Ivanova, N., & O'Shaughnessy, R. 2006, *ApJ*, **637**, 937
- O'Shaughnessy, R., Gerosa, D., & Wysocki, D. 2017, *PhRvL*, **119**, 011101
- Oguri, M. 2018, *MNRAS*, **480**, 3842
- Olejak, A., Fishbach, M., Belczynski, K., et al. 2020, *ApJL*, **901**, L39
- Ossokine, S., Buonanno, A., Marsat, S., et al. 2020, *PhRvD*, **102**, 044055
- Özel, F., Psaltis, D., Narayan, R., & McClintock, J. E. 2011, *ApJ*, **725**, 1918
- Pan, Y., Buonanno, A., Taracchini, A., et al. 2014, *PhRvD*, **89**, 084006
- Park, D., Kim, C., Lee, H. M., Bae, Y.-B., & Belczynski, K. 2017, *MNRAS*, **469**, 4665
- Portegies Zwart, S. F., & McMillan, S. L. W. 2000, *ApJL*, **528**, L17
- Portegies Zwart, S. F., & Yungelson, L. R. 1998, *A&A*, **332**, 173
- Pratten, G., & Vecchio, A. 2020, arXiv:2008.00509
- Pretorius, F. 2005, *PhRvL*, **95**, 121101
- Qin, Y., Fragos, T., Meynet, G., et al. 2018, *A&A*, **616**, A28
- Rice, J. R., & Zhang, B. 2021, *ApJ*, **908**, 59
- Riddell, A., Hartikainen, A., Lee, D., et al. 2018, *Stan-Dev/PyStan: v2.18.0.0*, Zenodo, doi:10.5281/ZENODO.1456206
- Rodriguez, C. L., Amaro-Seoane, P., Chatterjee, S., & Rasio, F. A. 2018, *PhRvL*, **120**, 151101
- Rodriguez, C. L., & Antonini, F. 2018, *ApJ*, **863**, 7
- Rodriguez, C. L., & Loeb, A. 2018, *ApJL*, **866**, L5
- Rodriguez, C. L., Morscher, M., Pattabiraman, B., et al. 2015, *PhRvL*, **115**, 051101
- Rodriguez, C. L., Zevin, M., Amaro-Seoane, P., et al. 2019, *PhRvD*, **100**, 043027
- Rodriguez, C. L., Zevin, M., Pankow, C., Kalogera, V., & Rasio, F. A. 2016, *ApJL*, **832**, L2
- Romero-Shaw, I. M., Lasky, P. D., & Thrane, E. 2019, *MNRAS*, **490**, 5210
- Romero-Shaw, I. M., Lasky, P. D., Thrane, E., & Bustillo, J. C. 2020a, *ApJL*, **903**, L5
- Romero-Shaw, I. M., Talbot, C., Biscoveanu, S., et al. 2020b, *MNRAS*, **499**, 3295
- Roulet, J., Venumadhav, T., Zackay, B., Dai, L., & Zaldarriaga, M. 2020, *PhRvD*, **102**, 123022
- Roulet, J., & Zaldarriaga, M. 2019, *MNRAS*, **484**, 4216
- Roupas, Z., & Kazanas, D. 2019, *A&A*, **632**, L8
- Sachdev, S., Caudill, S., Fong, H., et al. 2019, arXiv:1901.08580
- Safarzadeh, M. 2020, *NatAs*, **4**, 735
- Safarzadeh, M., Farr, W. M., & Ramirez-Ruiz, E. 2020, *ApJ*, **894**, 129
- Safarzadeh, M., & Haiman, Z. 2020, *ApJL*, **903**, L21
- Samsing, J. 2018, *PhRvD*, **97**, 103014
- Samsing, J., MacLeod, M., & Ramirez-Ruiz, E. 2014, *ApJ*, **784**, 71
- Samsing, J., & Ramirez-Ruiz, E. 2017, *ApJL*, **840**, L14
- Santoliquido, F., Mapelli, M., Bouffanais, Y., et al. 2020, *ApJ*, **898**, 152
- Schmidt, P., Hannam, M., & Husa, S. 2012, *PhRvD*, **86**, 104063
- Schmidt, P., Ohme, F., & Hannam, M. 2015, *PhRvD*, **91**, 024043
- Sigurdsson, S., & Hernquist, L. 1993, *Natur*, **364**, 423
- Smith, G. P., Jauzac, M., Veitch, J., et al. 2018, *MNRAS*, **475**, 3823
- Speagle, J. S. 2020, *MNRAS*, **493**, 3132
- Spera, M., & Mapelli, M. 2017, *MNRAS*, **470**, 4739

- Stevenson, S., Berry, C. P. L., & Mandel, I. 2017, *MNRAS*, **471**, 2801
- Stone, N. C., Metzger, B. D., & Haiman, Z. 2017, *MNRAS*, **464**, 946
- Sun, L., Goetz, E., Kissel, J. S., et al. 2020, *CQGra*, **37**, 225008
- Tagawa, H., Haiman, Z., & Kocsis, B. 2020, *ApJ*, **898**, 25
- Talbot, C., Smith, R., Thrane, E., & Poole, G. B. 2019, *PhRvD*, **100**, 043030
- Talbot, C., & Thrane, E. 2017, *PhRvD*, **96**, 023012
- Talbot, C., & Thrane, E. 2018, *ApJ*, **856**, 173
- Tan, H., Noronha-Hostler, J., & Yunes, N. 2020, *PhRvL*, **125**, 261104
- Tanikawa, A., Susa, H., Yoshida, T., Trani, A. A., & Kinugawa, T. 2021, *ApJ*, **910**, 30
- Taracchini, A., Buonanno, A., Pan, Y., et al. 2014, *PhRvD*, **89**, 061502
- Tews, I., Pang, P. T., Dietrich, T., et al. 2021, *ApJL*, **908**, L1
- Thompson, T. A., Kochanek, C. S., Stanek, K. Z., et al. 2019, *Sci*, **366**, 637
- Thrane, E., & Talbot, C. 2019, *PASA*, **36**, E010
- Tiwari, V. 2018, *CQGra*, **35**, 145009
- Tiwari, V. 2020, arXiv:2006.15047
- Tiwari, V., Fairhurst, S., & Hannam, M. 2018, *ApJ*, **868**, 140
- Usman, S. A., Nitz, A. H., Harry, I. W., et al. 2016, *CQGra*, **33**, 215004
- van Son, L. A. C., de Mink, S. E., Broekgaarden, F. S., et al. 2020, *ApJ*, **897**, 100
- Varma, V., Field, S. E., Scheel, M. A., et al. 2019, *PhRvR*, **1**, 033015
- Veitch, J., Raymond, V., Farr, B., et al. 2015, *PhRvD*, **91**, 042003
- Venumadhav, T., Zackay, B., Roulet, J., Dai, L., & Zaldarriaga, M. 2019, *PhRvD*, **100**, 023011
- Venumadhav, T., Zackay, B., Roulet, J., Dai, L., & Zaldarriaga, M. 2020, *PhRvD*, **101**, 083030
- Vigna-Gómez, A., Toonen, S., Ramirez-Ruiz, E., et al. 2021, *ApJL*, **907**, L19
- Vitale, S. 2020, arXiv:2007.05579
- Vitale, S., Gerosa, D., Haster, C.-J., Chatzioannou, K., & Zimmerman, A. 2017a, *PhRvL*, **119**, 251103
- Vitale, S., Lynch, R., Sturani, R., & Graff, P. 2017b, *CQGra*, **34**, 03LT01
- Woosley, S. E. 2017, *ApJ*, **836**, 244
- Woosley, S. E., & Heger, A. 2015, in *Very Massive Stars Local Universe*, Astrophysics and Space Science Library, Vol. 412, ed. J. Vink (Cham: Springer), 199
- Woosley, S. E., Heger, A., & Weaver, T. A. 2002, *RvMP*, **74**, 1015
- Wysocki, D. 2020, LIGO Document T2000432-v1, <https://dcc.ligo.org/LIGO-T2000432/public>
- Wysocki, D., Lange, J., & O’Shaughnessy, R. 2019a, *PhRvD*, **100**, 043012
- Wysocki, D., & O’Shaughnessy, R. 2017, Bayesian Parametric Population Models, bayesian-parametric-population-models.readthedocs.io
- Wysocki, D., O’Shaughnessy, R., Lange, J., & Fang, Y.-L. L. 2019b, *PhRvD*, **99**, 084026
- Wysocki, D., Gerosa, D., O’Shaughnessy, R., et al. 2018, *PhRvD*, **97**, 043014
- Yang, Y., Bartos, I., Gayathri, V., et al. 2019, *PhRvL*, **123**, 181101
- Zackay, B., Dai, L., Venumadhav, T., Roulet, J., & Zaldarriaga, M. 2020, *PhRvD*, **101**, 083030
- Zackay, B., Venumadhav, T., Dai, L., Roulet, J., & Zaldarriaga, M. 2019, *PhRvD*, **100**, 023007
- Zaldarriaga, M., Kushnir, D., & Kollmeier, J. A. 2018, *MNRAS*, **473**, 4174
- Zevin, M., Pankow, C., Rodriguez, C. L., et al. 2017, *ApJ*, **846**, 82
- Zevin, M., Samsing, J., Rodriguez, C., Haster, C.-J., & Ramirez-Ruiz, E. 2019, *ApJ*, **871**, 91
- Zevin, M., Spera, M., Berry, C. P., & Kalogera, V. 2020, *ApJL*, **899**, L1
- Zhang, N.-B., & Li, B.-A. 2020, *ApJ*, **902**, 38
- Ziegler, J., & Freese, K. 2020, arXiv:2010.00254
- Ziosi, B. M., Mapelli, M., Branchesi, M., & Tormen, G. 2014, *MNRAS*, **441**, 3703